ICES REPORT 12-43

November 2012

Functional Entropy Variables: A New Methodology for Deriving Thermodynamically Consistent Algorithms for Complex Fluids, with Particular Reference to the Isothermal Navier-Stokes-Korteweg Equations

by

Ju Liu, Hector Gomez, John A. Evans, Thomas J.R. Hughes, and Chad M. Landis

Report Documentation Page

1. REPORT DATE **NOV 2012**	2. REPORT TYPE	3. DATES COVERED **00-00-2012 to 00-00-2012**

4. TITLE AND SUBTITLE	5a. CONTRACT NUMBER
Functional Entropy Variables: A New Methodology for Deriving Thermodynamically Consistent Algorithms for Complex Fluids, with Particular Reference to the Isothermal Navier-Stokes-Korteweg Equations	
	5b. GRANT NUMBER
	5c. PROGRAM ELEMENT NUMBER
6. AUTHOR(S)	5d. PROJECT NUMBER
	5e. TASK NUMBER
	5f. WORK UNIT NUMBER

7. PERFORMING ORGANIZATION NAME(S) AND ADDRESS(ES) **The University of Texas at Austin,The Institute for Computational Engineering and Sciences,Austin,TX,78712**	8. PERFORMING ORGANIZATION REPORT NUMBER

9. SPONSORING/MONITORING AGENCY NAME(S) AND ADDRESS(ES)	10. SPONSOR/MONITOR'S ACRONYM(S)
	11. SPONSOR/MONITOR'S REPORT NUMBER(S)

12. DISTRIBUTION/AVAILABILITY STATEMENT
Approved for public release; distribution unlimited

13. SUPPLEMENTARY NOTES

14. ABSTRACT

We propose a new methodology for the numerical solution of the isothermal Navier-Stokes- Korteweg equations. Our methodology is based on a semi-discrete Galerkin method invoking functional entropy variables, a generalization of classical entropy variables, and a new time integration scheme. We show that the resulting fully discrete scheme is unconditionally stable-in-energy, second-order time-accurate, and mass-conservative. We utilize isogeometric analysis for spatial discretization and verify the aforementioned properties by adopting the method of manufactured solutions and comparing coarse mesh solutions with overkill solutions. Various problems are simulated to show the capability of the method. Our methodology provides a means of constructing unconditionally stable numerical schemes for nonlinear non-convex hyperbolic systems of conservation laws.

15. SUBJECT TERMS

16. SECURITY CLASSIFICATION OF:			17. LIMITATION OF ABSTRACT	18. NUMBER OF PAGES	19a. NAME OF RESPONSIBLE PERSON
a. REPORT **unclassified**	b. ABSTRACT **unclassified**	c. THIS PAGE **unclassified**	**Same as Report (SAR)**	**62**	

Functional Entropy Variables: A New Methodology for Deriving Thermodynamically Consistent Algorithms for Complex Fluids, with Particular Reference to the Isothermal Navier-Stokes-Korteweg Equations

Ju Liu [a,*], Hector Gomez [b], John A. Evans [a], Thomas J.R. Hughes [a],
Chad M. Landis [c]

[a] *Institute for Computational Engineering and Sciences, The University of Texas at Austin,*
201 East 24th Street, 1 University Station C0200, Austin, TX 78712, USA
[b] *Department of Mathematical Methods, University of A Coruña,*
Campus de Elviña, s/n, 15192, A Coruña
[c] *Aerospace Engineering and Engineering Mechanics, The University of Texas at Austin,*
210 East 24th Street, 1 University Station C0600, Austin, TX 78712, USA
[*] *Corresponding author. E-mail address:* jliu@ices.utexas.edu

Abstract

We propose a new methodology for the numerical solution of the isothermal Navier-Stokes-Korteweg equations. Our methodology is based on a semi-discrete Galerkin method invoking *functional* entropy variables, a generalization of classical entropy variables, and a new time integration scheme. We show that the resulting fully discrete scheme is unconditionally stable-in-energy, second-order time-accurate, and mass-conservative. We utilize isogeometric analysis for spatial discretization and verify the aforementioned properties by adopting the method of manufactured solutions and comparing coarse mesh solutions with overkill solutions. Various problems are simulated to show the capability of the method. Our methodology provides a means of constructing unconditionally stable numerical schemes for nonlinear non-convex hyperbolic systems of conservation laws.

1

1   Introduction

We present a new fully discrete numerical formulation for the isothermal Navier-Stokes-Korteweg equations. This formulation is motivated by the concept of entropy variables and is provably unconditionally stable-in-energy and second-order accurate in time. Consequently, our new formulation exhibits enhanced robustness in comparison with classical methods, making it an attractive candidate for the numerical simulation of phase transition phenomena.

1.1   Phase transition phenomena and the Navier-Stokes-Korteweg equations

Liquid-vapor phase transition phenomena occur ubiquitously in the natural world as well as in engineering practice. For example, one study shows that sea water's liquid-vapor transition induced by shrimp claw closure is one major contribution to deep sea background noise [66]. In the shipbuilding industry, liquid-vapor phase transition is a critical factor in the design of robust, low-noise, and efficient propellers [45], and, nowadays, carbon dioxide is compressed into a supercritical fluid state and injected into underground reservoirs to mitigate the greenhouse effect [64]. Despite the common occurrences of the phase transition phenomenon, it is rather poorly understood from a theoretical standpoint. Introduced by and named after the 1910 Nobel Laureate in physics, the van der Waals fluid model is considered an ideal candidate for modeling the liquid-vapor phase transition phenomenon. In the van der Waals model, the description of the liquid and vapor phases of a single material are unified into one continuous equation of state. This equation of state is regarded as a generalization of the perfect gas law by accounting for long-range molecular interactions and is even believed applicable to solid phases [40]. Using the van der Waals fluid model, Korteweg derived a model of capillarity from thermodynamic considerations. This model can then be inserted into the compressible Navier-Stokes equations, resulting in a third-order partial differential system of balance laws known as the Navier-Stokes-Korteweg equations. This system was shown to satisfy the second law of thermodynamics in 1985 [23]. In the present work, we restrict our attention to the isothermal Navier-Stokes-Korteweg equations and develop a new numerical scheme to study the liquid-vapor two phase flow of a single substance.

The van der Waals fluid model has been a focal point of research across different disciplines over the last few decades. Mathematically, it is known that the Navier-Stokes-Korteweg system is of nonlinear hyperbolic type above a critical temperature in the sharp-interface limit of vanishing viscosity and capillarity, while below the critical temperature, it is a mixed hyperbolic-elliptic differential system. Existence, uniqueness, and well-posedness results for such systems are still lacking [46], though a number of mathematical results have been established for the Navier-Stokes-Korteweg equations in the presence of non-vanishing viscosity [28] or capillarity [9, 14, 20, 35, 44]. We anticipate that our new numerical scheme could motivate further theoretical study. The Navier-Stokes-Korteweg equations can be categorized as a phase-field model. In the continuum mechanics community, the phase-field approach is used to model various types of multiphase phenomena including microstructure evolution [16], ferroelectric ceramics [63], and cancerous tumor growth [52], to name just a

few. Despite its widespread applicability, the van der Waals fluid model is not perfect. As will be shown in Figure 2, the van der Waals fluid model mimics the behavior of fluid in liquid and vapor phases qualitatively, but it is by no means accurate. Recent efforts have been made to modify the model in an attempt to increase its accuracy for specific materials [57].

1.2   Entropy variables and provably stable-in-entropy[1] schemes

In the sharp-interface limit of vanishing viscosity and capillarity, the Navier-Stokes-Korteweg equations become a partial differential system of nonlinear hyperbolic or mixed (hyperbolic-elliptic) type. Weak solutions of these types of equations are typically non-unique and exhibit several distinct wave structures. In order to obtain physically admissible solutions, one or more additional constraints must be placed on weak solutions. In the context of the Navier-Stokes-Korteweg equations, one should enforce the second law of thermodynamics to ensure the mathematical entropy is non-increasing in time. Such a relation should also be satisfied on the discrete level. Indeed, as Sobolev norms have been adopted for analyzing stability of linear problems [36], entropy norms play an analogous role in analyzing the stability of nonlinear problems.

The study of entropy-stable schemes for gas dynamics can be traced back to early work on symmetrization of the Euler and Navier-Stokes equations [34, 38, 65]. In those works, it was shown that the weighted residual form of the symmetrized Navier-Stokes equations will produce semi-discrete solutions automatically satisfying the Clausius-Duhem inequality. The symmetrized form of the Navier-Stokes equations invokes a particular set of fluid variables which are referred to as entropy variables. In the late 1980s, it was proven that the weighted residual form of the symmetrized Navier-Stokes equations in conjunction with a space-time formulation constitutes a fully discrete scheme which is provably unconditionally stable-in-entropy [58, 59]. However, the situation becomes more complicated in the context of the van der Waals fluid model. The system of conservation laws describing a van der Waals fluid exhibit a mixed type differential system under the critical temperature since the associated entropy function is not globally convex. This fact results in two main difficulties. First and foremost, the classical way of defining entropy variables does not result in a viable variable set. Namely, the mapping between conservation variables and classical entropy variables is not invertible (see our discussion in Section 2.4). Second, the space-time method is no longer guaranteed to be unconditionally stable-in-entropy as its stability relies on one crucial fact – that the Jacobian matrix describing the mapping from conservation variables to classical entropy variables is positive definite. In the context of the van der Waals fluid model, the Jacobian matrix can be singular or even negative definite within the diffuse interface. Numerical analyses for mixed type differential systems have been carried out by precursors in the finite difference community [42, 60, 62]. However, to the best of our knowledge, there are very few semi-discrete schemes that have achieved entropy stability [15, 17]. Among the schemes that are indeed entropy stable, the common techniques employed are intricate

---

[1]In the isothermal case, the second law of thermodynamics is represented in terms of an energy dissipation inequality, where the total energy takes on the role of mathematical entropy function. Hence we call our method stable-in-energy, which is equivalent to the notion of stable-in-entropy. In the remainder of the text, the two terms "stable-in-energy" and "stable-in-entropy" are used interchangeably.

discrete flux terms to directly enforce the nonlinear stability condition. Moreover, there have been no practical provably stable-in-entropy fully discrete schemes developed as of yet.

In this work, the two difficulties mentioned above are addressed. First, we generalize the notion of entropy variables to the functional setting. In the presence of capillarity, the standard mathematical entropy function is supplemented with a differential regularization term and new entropy variables are defined as the variational derivatives of this new mathematical entropy functional with respect to conservation variables. A calculation will reveal that the entropy variable corresponding to momentum is simply the velocity field while the entropy variable corresponding to density is a complicated and nonlinear function of density, velocity, and derivatives of the density field. We introduce this non-trivial entropy variable as a new independent variable and couple it with our conservation laws by replacing pressure and capillarity terms with this new variable. In doing so, the equation associated with the entropy variable plays an analogous role to the equation of state, and we no longer need to deal with a degenerate change-of-variables from conservation variables to entropy variables. It will be shown that the weighted residual formulation of this modified strong problem will lead to an unconditionally stable-in-entropy semi-discrete formulation. Second, to develop a stable fully discrete scheme, we apply a recently proposed time integration scheme based on a perturbation of the trapezoidal rule [31]. This time integration scheme has several appealing features: (1) The nonlinear stability of the semi-discrete scheme is inherited at the fully discrete level; (2) Second-order accuracy is attained; (3) The introduced numerical dissipation can be tuned by adjusting a single parameter; (4) There is no requirement of convexity for the mathematical entropy functional. Hence, this time marching scheme is an ideal candidate for constructing a fully discrete scheme for the Navier-Stokes-Korteweg system. We prove the aforesaid properties of the fully discrete scheme with a comprehensive suite of numerical tests.

1.3   Isogeometric analysis

Isogeometric analysis was initially proposed to create a pathway for breaking down the barrier between Computer Aided Engineering (CAE) and Computer Aided Design (CAD) [37]. Invoking the isoparametric paradigm, isogeometric analysis utilizes the same basis functions that are used in CAD as the basis for engineering analysis. Such an approach retains an exact representation of geometry at every level of discretization in contrast with traditional element/grid based numerical methods. Isogeometric analysis allows one to bypass many of the costs of mesh refinement since there is no need to link to the CAD geometry once the coarse but geometrically exact mesh is generated. In contrast, the classical mesh refinement process requires communication with the CAD system at each refinement iteration, which is not only time consuming but also error prone. Moreover, isogeometric analysis possesses the unique k-refinement concept, which enables the generation of higher-order, higher-continuity basis functions without a proliferation of degrees of freedom. The enhanced continuity of isogeometric analysis basis functions has allowed for straightforward Galerkin discretization of high-order differential equations which are often encountered, for example, in thin shell theory [43] and phase-field models [12, 21, 30]. The k-refinement concept has also been shown to exhibit enhanced robustness and accuracy in comparison with classical C^0 finite elements [19, 24]. In particular, it has been shown that smooth basis functions may result

in sharp oscillation-free descriptions of the interface in diffuse interface models [30].

The first instantiations of isogeometric analysis were based on Non-Uniform Rational B-Splines (NURBS), and to date, NURBS-based isogeometric analysis has achieved great success in a number of application areas including complex flow problems [5, 7] and phase-field models [30, 32]. Recently, isogeometric analysis technologies based on other classes of basis functions have been developed. Perhaps the most promising of these technologies is analysis-suitable T-splines [55]. T-splines allow local refinement as well as watertight parametrization of complex geometry in a single patch. These two characteristics make this technology an attractive candidate for capturing diffuse interfaces at realistic length scales. Another recently proposed isogeometric technology is divergence-conforming B-splines for incompressible flows [25]. It has been shown that this technology guarantees a pointwise divergence-free velocity field and enjoys a variety of conservation properties at the discrete level. We anticipate such basis functions may be utilized in compressible flow simulations as well in the hopes of attaining a well-behaved discretization in the incompressible limit, which is often the bane of compressible flow simulation technologies. In this work, we restrict ourselves to the NURBS-based isogeometric analysis approach, but we would like to point out that the new aforementioned technologies constitute promising future research directions.

1.4   Structure and content of the paper

The body of the paper begins in Section 2 where we present the strong form of the isothermal Navier-Stokes-Korteweg equations, both in dimensional and non-dimensional form, and discuss the thermodynamic properties of the van der Waals fluid model. Following, we discuss the deficiency of traditional entropy variables in the context of the van der Waals fluid model and introduce so-called functional entropy variables. In Section 3, we discuss a new fully discrete scheme for the Navier-Stokes-Korteweg problem based on functional entropy variables, and we theoretically analyze the stability and accuracy properties of our scheme. In Section 4, we perform a comprehensive numerical verification of our scheme, and in Section 5, we simulate a selection of benchmark problems. We present concluding remarks in Section 6. In Appendices A and B we summarize our methodology for constructing unconditionally stable algorithms through the use of quadrature rules. In Appendix A, we illustrate ideas with the construction of an unconditionally stable first-order scheme. In Appendix B we derive an unconditionally stable second-order scheme generalizing the mid-point rule.

2   The Isothermal Navier–Stokes–Korteweg equations

In this section, we present the isothermal Navier–Stokes–Korteweg equations and analyze the thermodynamic properties of the van der Waals fluid model. Furthermore, we generalize the notion of entropy variables to the setting of the Navier–Stokes–Korteweg equations by introducing the concept of functional entropy variables, and we present a modified strong form of the Navier–Stokes–Korteweg problem in terms of these variables.

2.1 Continuous problem in strong form

Let $\Omega \subset \mathbb{R}^d$ be an arbitrary open, connected, and bounded domain, where d is the number of spatial dimensions. The boundary of Ω is denoted as Γ and assumed to be sufficiently smooth (e.g. Lipschitz). The outward directed unit vector normal to Γ is denoted as $\mathbf{n}$. The time interval is denoted $(0, T)$, with $T > 0$. A pure material (e.g. water) is contained in Ω, and $\rho : \bar{\Omega} \times (0, T) \to (0, b)$ and $\mathbf{u} : \bar{\Omega} \times (0, T) \to \mathbb{R}^d$ denote the density and velocity fields of the material where b is the value of the maximal attainable density. The initial/boundary value problem of interest can be stated as follows: find the density ρ and velocity $\mathbf{u}$ such that

$$\frac{\partial \rho}{\partial t} + \nabla \cdot (\rho \mathbf{u}) = 0 \qquad \qquad \text{in } \Omega \times (0, T), \qquad (1)$$

$$\frac{\partial (\rho \mathbf{u})}{\partial t} + \nabla \cdot (\rho \mathbf{u} \otimes \mathbf{u} + p \mathbf{I}) - \nabla \cdot \boldsymbol{\tau} - \nabla \cdot \boldsymbol{\varsigma} = \rho \mathbf{f} \qquad \text{in } \Omega \times (0, T), \qquad (2)$$

$$\nabla \rho \cdot \mathbf{n} = 0 \qquad \qquad \text{on } \Gamma \times (0, T), \qquad (3)$$

$$\mathbf{u} = \mathbf{0} \qquad \qquad \text{on } \Gamma \times (0, T), \qquad (4)$$

$$\rho(x, 0) = \rho_0(x) \qquad \qquad \text{in } \bar{\Omega}, \qquad (5)$$

$$\mathbf{u}(x, 0) = \mathbf{u}_0(x) \qquad \qquad \text{in } \bar{\Omega}. \qquad (6)$$

Above, $\rho_0 : \bar{\Omega} \to (0, b)$ and $\mathbf{u}_0 : \bar{\Omega} \to \mathbb{R}^d$ are given functions which represent the initial density and velocity fields, $\boldsymbol{\tau}$ is the viscous stress tensor, $\boldsymbol{\varsigma}$ is the Korteweg stress tensor defined as

$$\boldsymbol{\varsigma} = \lambda \left(\rho \Delta \rho + \frac{1}{2} |\nabla \rho|^2 \right) \mathbf{I} - \lambda \nabla \rho \otimes \nabla \rho \qquad (7)$$

where λ is the capillary coefficient, $\mathbf{f}$ is the body force per unit mass, and p is the thermodynamic pressure. In this paper, we consider a Newtonian fluid, i.e., $\boldsymbol{\tau}$ takes the form

$$\boldsymbol{\tau} = \bar{\mu} \left(\nabla \mathbf{u} + \nabla^T \mathbf{u} \right) + \bar{\lambda} \nabla \cdot \mathbf{u} \mathbf{I} \qquad (8)$$

where $\bar{\mu}$ and $\bar{\lambda}$ are the first and second viscosity coefficients and $\mathbf{I}$ is the identity tensor. To derive an explicit form for the thermodynamic pressure, we have to introduce thermodynamic relations in terms of a free energy function W. In the isothermal case, W is a univariate function of ρ. Therefore, the pressure p and the chemical potential μ are defined by W and $dW/d\rho$ in the following manner.

Definition 1. *(Fundamental Thermodynamic Relations) Given the isothermal free energy function $W(\rho)$, the pressure p and chemical potential μ are defined as:*

$$p = \rho \frac{dW}{d\rho} - W, \qquad (9)$$

$$\mu = \frac{dW}{d\rho}. \qquad (10)$$

The isothermal free energy for a van der Waals fluid takes the form

$$W(\rho) = R\theta\rho \log\left(\frac{\rho}{b-\rho}\right) - a\rho^2. \tag{11}$$

where θ is the temperature, and R is the universal gas constant. From the above relations, the following explicit forms for the pressure p and chemical potential μ can be derived:

$$p = Rb\frac{\rho\theta}{b-\rho} - a\rho^2, \tag{12}$$

$$\mu = R\theta \log\left(\frac{\rho}{b-\rho}\right) + R\theta\frac{b}{b-\rho} - 2a\rho. \tag{13}$$

Equations (1)-(6) represent mass conservation, linear momentum balance, no-slip boundary condition for the velocity field, homogenous Neumann boundary condition for the density field, and initial conditions, respectively. For mathematical results regarding the existence and uniqueness of local strong solutions, see [44].

The critical temperature θ_{crit}, defined as the lowest temperature for the existence of a single phase, is given by

$$\theta_{crit} = \frac{8ab}{27R}, \tag{14}$$

and the critical density and the critical pressure pair (ρ_{crit}, p_{crit}) are defined to be the inflection point of the pressure function (12) at the critical temperature. Simple calculations show that

$$\rho_{crit} = \frac{b}{3}, \tag{15}$$

$$p_{crit} = \frac{ab^2}{27}. \tag{16}$$

Remark 1. *The values of the critical temperature, density, and pressure for typical fluids can be found from the NIST database [1]. For instance, the critical temperature, density, and pressure of water are 647.096 K, 322.0 kg/m^3, and 22.064 $\times$ 10^6 N/m^2 respectively.*

Remark 2. *In this work, we always assume that the Stokes's assumption is satisfied, i.e.,*

$$\bar{\lambda} = -\frac{2}{3}\bar{\mu}. \tag{17}$$

2.2 Dimensionless form of the isothermal Navier-Stokes-Korteweg equations

We now provide dimensionless forms of the Navier-Stokes-Korteweg equations. The fundamental idea motivating dimensional analysis is that physical laws must be independent of the units used to measure physical variables [3]. Additionally, a properly chosen reference scale can help us avoid round-off errors in numerical computations. Here we rescale the Navier-Stokes-Korteweg equations using the $MLT\Theta$ system. Let us denote the reference

7

scale of mass by M_0, length by L_0, time by T_0, and temperature by θ_0. Then we have the following non-dimensional quantities denoted with a superscript $*$:

$$x = L_0 x^*, \qquad t = T_0 t^*, \qquad \rho = \frac{M_0}{L_0^3}\rho^*, \qquad \mathbf{u} = \frac{L_0}{T_0}\mathbf{u}^*, \qquad \mathbf{f} = \frac{L_0}{T_0^2}\mathbf{f}^*,$$

$$\theta = \theta_0 \theta^*, \quad p = \frac{M_0}{L_0 T_0^2}p^*, \quad \lambda = \frac{L_0^7}{M_0 T_0^2}\lambda^*, \quad \bar{\mu} = \frac{M_0}{L_0 T_0}\bar{\mu}^* \quad \mathcal{H} = \frac{M_0}{L_0 T_0^2}\mathcal{H}^*. \tag{18}$$

where $\mathcal{H}$ represents the total energy density. Using the scaling relations (18), the dimensionless mass balance equation reads

$$\frac{M_0}{T_0 L_0^3}\left(\frac{\partial \rho^*}{\partial t^*} + \nabla^* \cdot (\rho^* \mathbf{u}^*)\right) = 0. \tag{19}$$

The momentum balance equations are rescaled as

$$\frac{M_0}{T_0^2 L_0^2}\left(\frac{\partial(\rho^* \mathbf{u}^*)}{\partial t^*} + \nabla^* \cdot (\rho^* \mathbf{u}^* \otimes \mathbf{u}^*) + \nabla^* p^* - \nabla^* \cdot \boldsymbol{\tau}^* - \nabla^* \cdot \boldsymbol{\varsigma}^* - \rho^* \mathbf{f}^*\right) = 0, \tag{20}$$

where the dimensionless viscous stress tensor and Korteweg stress tensor read

$$\boldsymbol{\tau}^* = \bar{\mu}^*\left(\nabla^* \mathbf{u}^* + \nabla^{*T}\mathbf{u} - \frac{2}{3}\nabla^* \cdot \mathbf{u}^* \mathbf{I}\right), \tag{21}$$

$$\boldsymbol{\varsigma}^* = \lambda^*\left(\rho^* \Delta^* \rho^* + \frac{1}{2}|\nabla^* \rho^*|^2\right)\mathbf{I} - \lambda^* \nabla^* \rho^* \nabla^{*T}\rho^*. \tag{22}$$

The equation of state is nondimensionalized as

$$\frac{M_0}{L_0 T_0^2}p^* = Rb\theta_0 \frac{\rho^* M_0 \theta^*}{bL_0^3 - \rho^* M_0} - a\rho^{*2}\frac{M_0^2}{L_0^6}, \tag{23}$$

and the total energy density is rescaled as

$$\mathcal{H}^* = W^*(\rho^*) + \frac{1}{2}\rho^*|\mathbf{u}^*| + \frac{1}{2}\lambda^*|\nabla^* \rho^*|^2, \tag{24}$$

where

$$W^*(\rho^*) = R\theta_0 \frac{T_0^2}{L_0^2}\theta^* \rho^* \log\left(\frac{M_0 \rho^*}{bL_0^3 - M_0 \rho^*}\right) - a\frac{M_0 T_0^2}{L_0^5}\rho^{*2}. \tag{25}$$

Notice that the dimensionless viscosity coefficient $\bar{\mu}^* = L_0 T_0 \bar{\mu}/M_0$ measures the ratio of the viscous force to the inertial force while the dimensionless capillarity coefficient $\lambda^* = M_0 T_0^2 \lambda/L_0^7$ measures the ratio of the surface tension to the inertia. Consequently, we denote these two coefficients as

$$\bar{\mu}^* = \frac{1}{\mathbb{R}\mathrm{e}}, \qquad \lambda^* = \frac{1}{\mathbb{W}\mathrm{e}} \tag{26}$$

where $\mathbb{R}\mathrm{e}$ is the Reynolds number and $\mathbb{W}\mathrm{e}$ is the Weber number [67].

8

Remark 3. *There are two other important dimensionless numbers associated with our problem. The capillarity number $\mathbb{C}a$, which measures the relative effect of the viscous force against the surface tension force, is defined to be*

$$\mathbb{C}a = \frac{\mathbb{W}e}{\mathbb{R}e}, \tag{27}$$

while the Bond number $\mathbb{B}o$, which measures the importance of the body force compared with the surface tension, is defined to be:

$$\mathbb{B}o = |\mathbf{f}^*|\mathbb{W}e. \tag{28}$$

If we choose our reference scales such that

$$\frac{M_0}{L_0^3} = b, \tag{29}$$

$$\frac{M_0}{L_0 T_0^2} = ab^2, \tag{30}$$

$$\theta_0 = \theta_{crit} = \frac{8ab}{27R}, \tag{31}$$

then the dimensionless isothermal Navier-Stokes-Korteweg equations read as follows:

$$\frac{\partial \rho^*}{\partial t^*} + \nabla^* \cdot (\rho^* \mathbf{u}^*) = 0, \tag{32}$$

$$\frac{\partial(\rho^* \mathbf{u}^*)}{\partial t^*} + \nabla^* \cdot (\rho^* \mathbf{u}^* \otimes \mathbf{u}^*) + \nabla^* p^* - \nabla^* \cdot \boldsymbol{\tau}^* - \nabla^* \cdot \boldsymbol{\varsigma}^* - \rho^* \mathbf{f}^* = 0, \tag{33}$$

where

$$p^* = \frac{8}{27} \frac{\theta^* \rho^*}{1 - \rho^*} - \rho^{*2}, \tag{34}$$

$$W^*(\rho^*) = \frac{8}{27} \theta^* \rho^* \log\left(\frac{\rho^*}{1 - \rho^*}\right) - \rho^{*2}, \tag{35}$$

$$\boldsymbol{\tau}^* = \frac{1}{\mathbb{R}e}\left(\nabla^* \mathbf{u}^* + \nabla^{*T}\mathbf{u}^* - \frac{2}{3}\nabla^* \cdot \mathbf{u}^*\boldsymbol{I}\right), \tag{36}$$

$$\boldsymbol{\varsigma}^* = \frac{1}{\mathbb{W}e}\left(\left(\rho^* \Delta^* \rho^* + \frac{1}{2}|\nabla^* \rho^*|^2\right)\mathbf{I} - \nabla^* \rho^* \nabla^{*T}\rho^*\right), \tag{37}$$

$$\mathbb{R}e = \frac{L_0 b\sqrt{ab}}{\bar{\mu}}, \tag{38}$$

$$\mathbb{W}e = \frac{aL_0^2}{\lambda}. \tag{39}$$

Likewise, the total energy is rescaled as

$$\mathcal{E}^*(\rho^*, \rho^* \mathbf{u}^*) = \int_{\Omega}\left(W^*(\rho^*) + \frac{1}{2\mathbb{W}e}|\nabla^* \rho^*|^2 + \frac{1}{2}\rho^*|\mathbf{u}^*|^2\right)d\mathbf{x}^*. \tag{40}$$

From (29) and (30), we may find that the reference time scale $T_0 = L_0/\sqrt{ab}$, which can be regarded as an inertial time scale. Among many other choices of time scales, $\sqrt{\lambda/(a^2 b)}$ is one associated with capillarity. Accordingly, we define the dimensionless time $\hat{t}$ scaled by the capillarity time scale:

$$t = T_0 t^* = \sqrt{\frac{\lambda}{a^2 b}} \hat{t}. \tag{41}$$

Then we have

$$\hat{t} = \sqrt{\frac{a^2 b}{\lambda}} T_0 t^* = L_0 \sqrt{\frac{a}{\lambda}} t^* = \mathbb{W} e^{\frac{1}{2}} t^*. \tag{42}$$

The relation (42) will be useful when we design our numerical algorithm in Section 3.3. We will henceforth use only the dimensionless form of the Navier-Stokes-Korteweg equations and, for the sake of notational simplicity, we will omit the superscript $*$ for dimensionless quantities.

2.3 Thermodynamics of the van der Waals fluid model
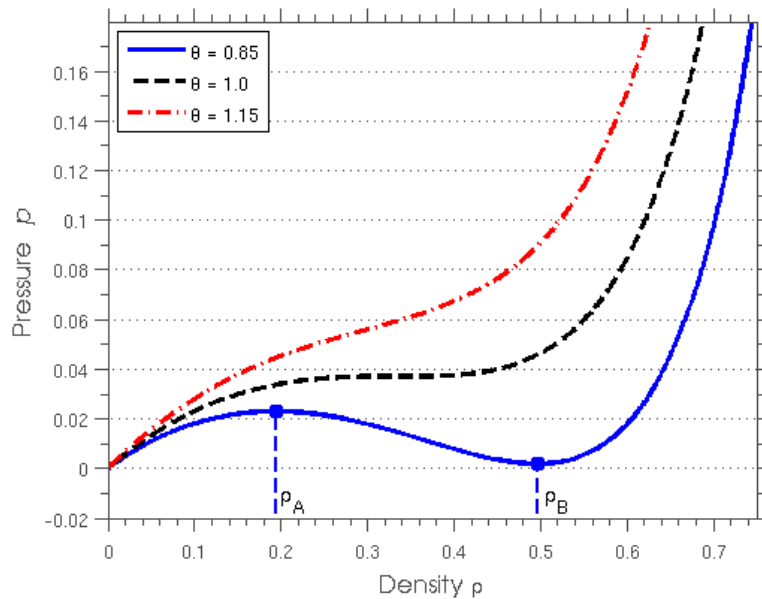
Figure 1: Pressure as a function of density at temperatures $\theta = 0.85$, 1.0, and 1.15. At $\theta = 0.85$, the elliptic region, defined as the range where the pressure function is monotonically decreasing with respect to the density field, is $(\rho_A, \rho_B) = (0.194, 0.496)$.

We now analyze in depth the thermodynamic properties of the van der Waals fluid model. In Figure 1, we have plotted the van der Waals equation of state given by (34) at three different temperatures. It is clear that the van der Waals pressure is a monotonically non-decreasing function with respect to density when $\theta \geq 1$. In this regime, the material is called

Figure 2: Comparison of van der Waals fluid model with real materials at $\theta = 0.85$. The data for water, carbon dioxide, methane, and propane are obtained from [1] and scaled to dimensionless form.
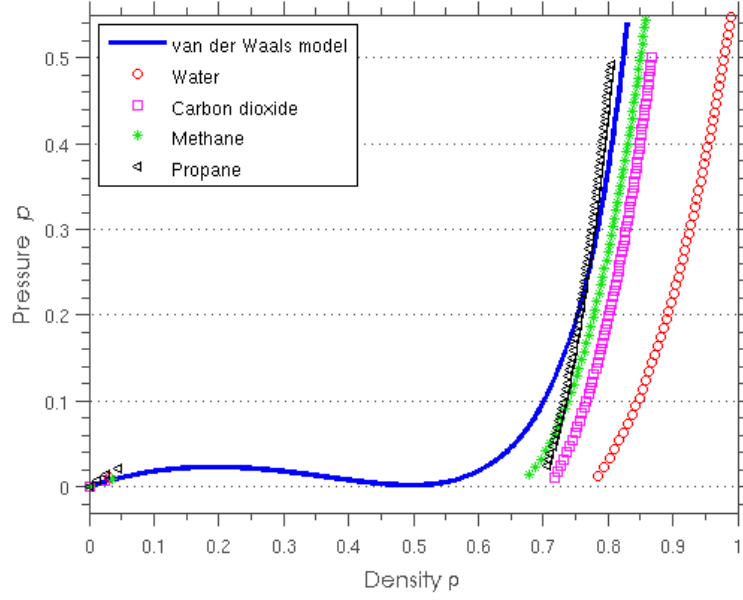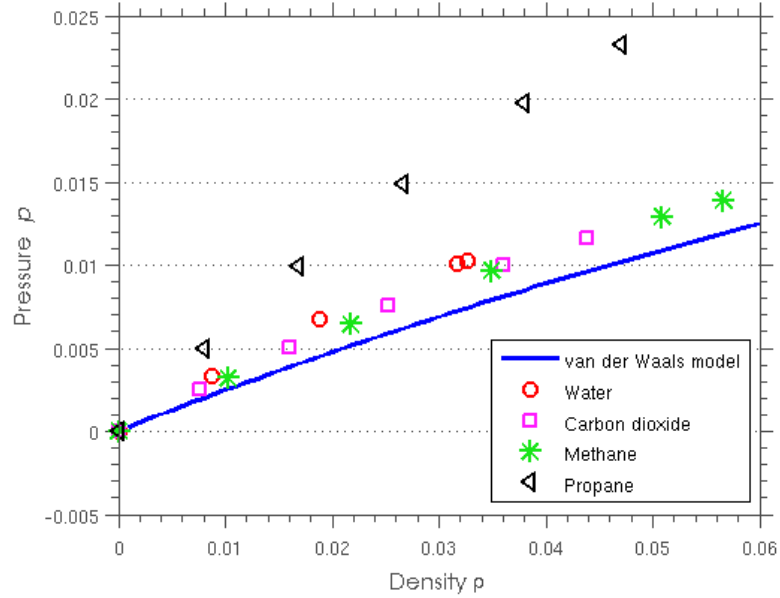

Figure 3: Detailed comparison of van der Waals fluid model with real materials at $\theta = 0.85$ in vapor phase. The data for water, carbon dioxide, methane, and propane are obtained from [1] and scaled to dimensionless form.
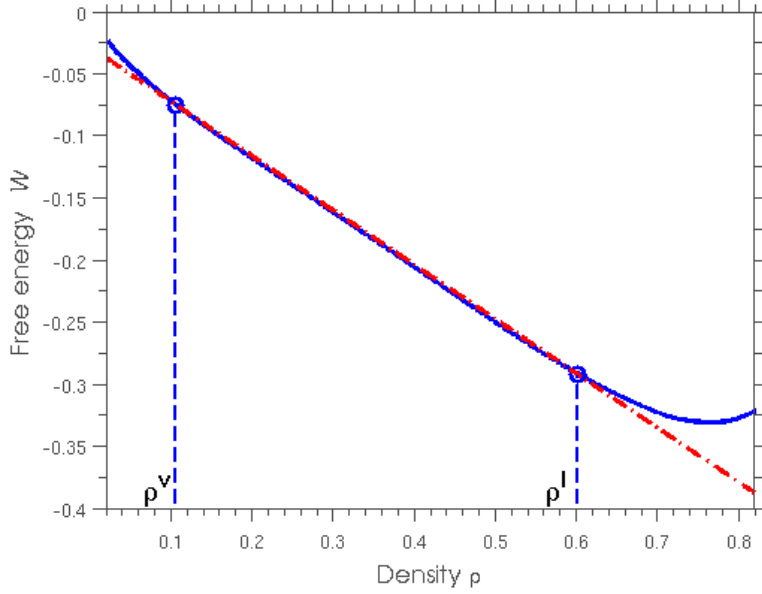
11

Figure 4: The isothermal free energy W as a function of density ρ at $\theta = 0.85$ is plotted as the blue solid line. The red dash-dotted line is the common tangent line passing through the Maxwell states $(\rho^v, W(\rho^v))$ and $(\rho^l, W(\rho^l))$, which are marked as blue circles.

a supercritical fluid as there are no distinct liquid vapor phases. When the temperature drops below the critical temperature, i.e., $\theta < 1$, the pressure function is no longer monotone, and there exists a region (ρ_A, ρ_B) where the pressure function decreases with respect to density, as is shown in the figure. In this regime, the density range $(0, \rho_A)$ corresponds to the vapor phase while the range $(\rho_B, 1)$ corresponds to the liquid phase. Mathematically, the Navier-Stokes-Korteweg system is of elliptic type in the sharp-interface limit when the density lies within the range (ρ_A, ρ_B). Moreover, the Mach number is imaginary and the system is physically unstable in this elliptic region. This is not entirely unexpected as the elliptic region corresponds to the interface between the liquid and vapor phases. The capillarity term acts to stabilize this region. To validate the van der Waals fluid model, we have downloaded the thermodynamic properties of water, carbon dioxide, methane, and propane from the NIST online database [1] and compared them with the van der Waals equation of state in dimensionless quantities. As is depicted in Figure 2 and 3, the van der Waals model gives a qualitatively accurate approximation of the various materials behavior in both liquid and vapor phases. It should be noted that the form of the equation of state is partially determined by the choice of critical point given by (15) and (16). Hence, there is still room to improve the van der Waals model for a specific material by tuning the parameters a and b using, for example, least squares. Recently, endeavors have also been made to modify the van der Walls model to get a more accurate representation of the pressure function for specific materials [57].

At a fixed temperature $\theta < 1$, the vapor phase density $\rho^v \in (0, \rho_A)$ and the liquid phase

density $\rho^l \in (\rho_B, 1)$ for a van der Waals fluid in equilibrium satisfy the following two relations:

$$p(\rho^v) = p(\rho^l), \tag{43}$$

$$\mu(\rho^v) = \mu(\rho^l). \tag{44}$$

The equilibrium densities (and their corresponding free energies) are referred to as Maxwell states. In this work, we fix $\theta = 0.85$. Solving the above two nonlinear equations at this temperature results in $\rho^v = 0.107$ and $\rho^l = 0.602$.

Remark 4. *Recalling the definitions of the pressure and the chemical potential given by* (12) *and* (13)*, we see the relations* (43) *and* (44) *imply that*

$$\frac{W(\rho^v) - W(\rho^l)}{\rho^v - \rho^l} = W'(\rho^l) = W'(\rho^v). \tag{45}$$

This means that $(\rho^v, W(\rho^v))$ *and* $(\rho^l, W(\rho^l))$ *lie on a common tangent line of* $W(\rho)$ *as is visually depicted in Figure 4.*

The following proposition gives another interesting and important observation for the free energy function W.

Proposition 1. *The free energy function* $W(\rho)$ *has positive fourth order derivative, i.e.,* $W''''(\rho) > 0$*, for* $\rho \in (0, 1)$*.*

Proof. Direct computations reveal that

$$W''''(\rho) = \frac{16\theta(6\rho^2 - 4\rho + 1)}{27\rho^3(1 - \rho)^4}. \tag{46}$$

By construction, the dimensionless temperature is always positive, i.e., $\theta > 0$. Furthermore, a direct calculation shows that the minimum of the quadratic polynomial $6\rho^2 - 4\rho + 1$ is $1/3$. Finally, due to our choice of reference scales, we know $0 < \rho < 1$. Combining all of these facts with the expression given by (46) leads to the conclusion that $W'''' > 0$. $\qquad\square$

Remark 5. *Free energy functions characterized by a positive fourth order derivative prevail in the area of phase-field modeling. This is a consequence of the fact that free energy functions arising in phase-field models have convex-concave-convex structures. We call functions with a positive fourth derivative as* **super-convex functions** *and functions with a negative fourth derivative as* **super-concave functions***.*

The following lemma provides a nonlinear stability result for smooth solutions of the isothermal Navier-Stokes-Korteweg equations. It is a global version of the Clausis-Duhem inequality in the isothermal setting.

Lemma 1. *Let* $(\rho, \rho\mathbf{u})$ *be a sufficiently smooth solution of the isothermal Navier-Stokes-Korteweg equations. Then, the total energy* $\mathcal{E}$ *satisfies the relation*

$$\frac{d}{dt}\mathcal{E}(\rho(\cdot, t), \rho\mathbf{u}(\cdot, t)) = -\int_\Omega \boldsymbol{\tau} : \nabla\mathbf{u}\,d\mathbf{x} + \int_\Omega \rho\mathbf{f}\,d\mathbf{x}, \tag{47}$$

where $\mathcal{E}$ *is defined in* (40)*.*

Proof. We multiply the continuity equation by $W'(\rho) - \frac{|\mathbf{u}|^2}{2}$ and the momentum equations by $\mathbf{u}$ and integrate them over the domain Ω:

$$\int_\Omega \left(\frac{\partial \rho}{\partial t} + \nabla \cdot (\rho \mathbf{u}) \right) \left(W'(\rho) - \frac{|\mathbf{u}|^2}{2} \right) d\mathbf{x} = 0, \tag{48}$$

$$\int_\Omega \left(\frac{\partial (\rho \mathbf{u})}{\partial t} + \nabla \cdot (\rho \mathbf{u} \otimes \mathbf{u} + p\mathbf{I}) - \nabla \cdot \boldsymbol{\tau} - \nabla \cdot \boldsymbol{\varsigma} - \rho \mathbf{f} \right) \cdot \mathbf{u} d\mathbf{x} = 0. \tag{49}$$

Summing the above two equation together and rearranging terms, it follows that

$$\int_\Omega \left(W'(\rho) \frac{\partial \rho}{\partial t} - \frac{|\mathbf{u}|^2}{2} \frac{\partial \rho}{\partial t} + \mathbf{u} \cdot \frac{\partial (\rho \mathbf{u})}{\partial t} - \nabla \cdot \boldsymbol{\varsigma} \right) d\mathbf{x}$$

$$= \int_\Omega \left(\mathbf{u} \cdot \nabla \cdot \boldsymbol{\tau} + \mathbf{u} \cdot \rho \mathbf{f} - \mathbf{u} \cdot \nabla \cdot (\rho \mathbf{u} \otimes \mathbf{u}) - \nabla p \cdot \mathbf{u} - \nabla \cdot (\rho \mathbf{u}) W'(\rho) + \nabla \cdot (\rho \mathbf{u}) \frac{|\mathbf{u}|^2}{2} \right) d\mathbf{x}. \tag{50}$$

Recalling that $\nabla \cdot \boldsymbol{\varsigma} = \rho \nabla \Delta \rho / \mathbb{W}\mathrm{e}$, we have

$$\int_\Omega \left(W'(\rho) \frac{\partial \rho}{\partial t} + \frac{|\mathbf{u}|^2}{2} \frac{\partial \rho}{\partial t} + \rho \mathbf{u} \cdot \frac{\partial \mathbf{u}}{\partial t} - \frac{1}{\mathbb{W}\mathrm{e}} \rho \mathbf{u} \cdot \nabla \Delta \rho \right) d\mathbf{x} = \int_\Omega \left(\mathbf{u} \cdot \nabla \cdot \boldsymbol{\tau} + \mathbf{u} \cdot \rho \mathbf{f} \right.$$

$$\left. - \nabla p \cdot \mathbf{u} - \rho W'(\rho) \nabla \cdot \mathbf{u} - W'(\rho) \nabla \rho \cdot \mathbf{u} + \nabla \cdot (\rho \mathbf{u}) \frac{|\mathbf{u}|^2}{2} - \mathbf{u} \cdot \nabla \cdot (\rho \mathbf{u} \otimes \mathbf{u}) \right) d\mathbf{x}. \tag{51}$$

We perform integration by parts and employ the boundary condition (4) to rewrite (51) as

$$\int_\Omega \left(\frac{d}{dt} W(\rho) + \frac{d}{dt} \left(\rho \frac{|\mathbf{u}|^2}{2} \right) + \frac{1}{\mathbb{W}\mathrm{e}} \nabla \cdot (\rho \mathbf{u}) \Delta \rho \right) d\mathbf{x}$$

$$= \int_\Omega \left(-\nabla \mathbf{u} : \boldsymbol{\tau} + \mathbf{u} \cdot \rho \mathbf{f} - \mathbf{u} \cdot \nabla \left(p + W(\rho) - \rho W'(\rho) \right) + \nabla \cdot \left(\rho |\mathbf{u}|^2 \mathbf{u} \right) \right) d\mathbf{x} \tag{52}$$

$$= \int_\Omega \left[-\nabla \mathbf{u} : \boldsymbol{\tau} + \mathbf{u} \cdot \rho \mathbf{f} - \mathbf{u} \cdot \nabla \left(p + W(\rho) - \rho W'(\rho) \right) \right] d\mathbf{x}. \tag{53}$$

Recalling $p = \rho W'(\rho) - W(\rho)$, $\nabla \cdot (\rho \mathbf{u}) = -\partial \rho / \partial t$ and making use of the boundary condition (3) yields

$$\int_\Omega \left[\frac{d}{dt} W(\rho) + \frac{d}{dt} \left(\rho \frac{|\mathbf{u}|^2}{2} \right) - \frac{1}{\mathbb{W}\mathrm{e}} \frac{\partial \rho}{\partial t} \Delta \rho \right] d\mathbf{x}$$

$$= \int_\Omega \left[\frac{d}{dt} W(\rho) + \frac{d}{dt} \left(\rho \frac{|\mathbf{u}|^2}{2} \right) + \frac{1}{\mathbb{W}\mathrm{e}} \nabla \left(\frac{\partial \rho}{\partial t} \right) \cdot \nabla \rho \right] d\mathbf{x}$$

$$= \int_\Omega \left[\frac{d}{dt} W(\rho) + \frac{d}{dt} \left(\rho \frac{|\mathbf{u}|^2}{2} \right) + \frac{d}{dt} \left(\frac{1}{2\mathbb{W}\mathrm{e}} |\nabla \rho|^2 \right) \right] d\mathbf{x}$$

$$= \int_\Omega \left(-\nabla \mathbf{u} : \boldsymbol{\tau} + \mathbf{u} \cdot \rho \mathbf{f} \right) d\mathbf{x}. \tag{54}$$

Finally, if we move the time derivative out of the integral, we obtain the desired result:

$$\frac{d}{dt} \mathcal{E}(\rho(\cdot, t), \rho(\cdot, t)) = \frac{d}{dt} \int_\Omega \left[W(\rho) + \left(\rho \frac{|\mathbf{u}|^2}{2} \right) + \left(\frac{1}{2\mathbb{W}\mathrm{e}} |\nabla \rho|^2 \right) \right] d\mathbf{x}$$

$$= \int_\Omega \left(-\nabla \mathbf{u} : \boldsymbol{\tau} + \mathbf{u} \cdot \rho \mathbf{f} \right) d\mathbf{x}. \tag{55}$$

14

□

As a direct corollary of the the above lemma, we have the following energy dissipation theorem.

Theorem 1. *Let $(\rho, \rho\mathbf{u})$ be a sufficiently smooth solution of the isothermal Navier-Stokes-Korteweg system given by (1)-(5). Assume that there is no body force (i.e., $\mathbf{f} = \mathbf{0}$) and that the Reynolds number is non-negative (i.e., $\mathbb{R}e \geq 0$). Then, we have the energy dissipation inequality:*

$$\frac{d}{dt}\mathcal{E}(\rho(\cdot, t), \rho\mathbf{u}(\cdot, t)) = -\int_\Omega \nabla\mathbf{u} : \boldsymbol{\tau} d\mathbf{x} \leq 0. \tag{56}$$

2.4   Functional entropy variables and a modified strong problem

For systems of conservation laws, stability with respect to a mathematical entropy function $\mathcal{H}$ is considered as a suitable notion for nonlinear stability and as an admissibility criterion for selecting physically relevant weak solutions. In the context of the isothermal Navier-Stokes-Korteweg equations, such a stability condition is represented by the energy dissipation relationship given by (56) where the corresponding mathematical entropy function is the sum of isothermal free energy and kinetic energy. In [34, 65], it was shown that systems of conservation laws which are endowed with a convex flux vector are symmetrizable if and only if there exists a mathematical entropy function. Given a set of conservation variables $\mathcal{U}$, the entropy variables which symmetrize the system are defined as the derivatives of the mathematical entropy function with respect to $\mathcal{U}$. In [38], the authors extended these ideas to the compressible Navier-Stokes equations. There, it was shown that the mathematical entropy must be an affine function of the physical entropy function and that semi-discrete solutions obtained from a weighted residual formulation based on entropy variables will respect the Clausius-Duhem inequality. Hence, entropy variables are a critical ingredient in the design of numerical schemes exhibiting nonlinear stability. To date, entropy-stable schemes based on entropy variables have been successfully applied to various problem classes including gas dynamics [59], the shallow water equations [13], and magnetohydrodynamics [48].

Unfortunately, for the van der Waals fluid model, the standard methodology for constructing an entropy-stable semi-discrete formulation cannot be directly applied. Notably, the entropy variables which are normally associated with the isothermal Navier-Stokes equations do not comprise a viable variable set in the context of the van der Waals model. This is a consequence of the fact that the free energy function associated with the van der Waals model is non-convex within the elliptic region, as is shown in the proof of the following proposition.

Proposition 2. *Let $\hat{\mathcal{H}} = W(\rho) + \frac{1}{2}\rho|\mathbf{u}|^2$ denote the mathematical entropy function associated with the isothermal Navier-Stokes equations. Furthermore, let $\mathcal{U} = (\rho, \rho\mathbf{u})^T$ denote the conservation variables associated with the isothermal Navier-Stokes equations. If W is given by the van der Waals model, the entropy variables $\hat{\mathcal{V}}^T = \partial\hat{\mathcal{H}}/\partial\mathcal{U}$ do not comprise a viable variable set when $\theta \leq 1$ in the sense that the mapping from $\mathcal{U}$ to $\hat{\mathcal{V}}$ is not invertible within the elliptic region.*

15

Proof. Let us consider the Hessian matrix $\dfrac{\partial \hat{\mathcal{V}}}{\partial \hat{\mathcal{U}}}$:

$$\frac{\partial \hat{\mathcal{V}}}{\partial \hat{\mathcal{U}}} = \frac{\partial^2 \hat{\mathcal{H}}}{\partial \hat{\mathcal{U}}^2} = \begin{pmatrix} W''(\rho) + \frac{|\mathbf{u}|^2}{\rho} & -\frac{u_1}{\rho} & -\frac{u_2}{\rho} & -\frac{u_3}{\rho} \\ -\frac{u_1}{\rho} & \frac{1}{\rho} & 0 & 0 \\ -\frac{u_2}{\rho} & 0 & \frac{1}{\rho} & 0 \\ -\frac{u_3}{\rho} & 0 & 0 & \frac{1}{\rho} \end{pmatrix}. \tag{57}$$

The determinant of the Hessian matrix is

$$\det\left(\frac{\partial^2 \hat{\mathcal{H}}}{\partial \hat{\mathcal{U}}^2}\right) = \frac{dp}{d\rho}\frac{1}{\rho^4}. \tag{58}$$

We know that below (at) the critical temperature there exists two (one) stationary points where $dp/d\rho = 0$. Hence, the Hessian matrix is not invertible everywhere and likewise neither is the change-of-variables mapping from $\hat{\mathcal{U}}$ to $\hat{\mathcal{V}}$. $\qquad\square$

Remark 6. *While the entropy variables $\hat{\mathcal{V}}$ do not comprise a viable variable set when $\theta \leq 1$, the Navier-Stokes-Korteweg equations can be formally symmetrized in terms of $\hat{\mathcal{V}}$, and the inner product of $\hat{\mathcal{V}}$ with the Navier-Stokes-Korteweg equations does result in the Clausius-Duhem inequality. This implies that entropy variables $\hat{\mathcal{V}}$ still can be used for the Navier-Stokes-Korteweg equations when above the critical temperature, but that is not the focus of this work.*

Remark 7. *Primitive variables (velocity and pressure) also do not comprise a viable variable set in the context of the van der Waals fluid model, because one cannot uniquely solve for the density field given the pressure field within the elliptic region.*

Proposition 2 prohibits the use of entropy variables obtained from the entropy function $\hat{\mathcal{H}}$ since the change-of-variables mapping is degenerate within the elliptic region. However, let us recall that the there exists a high-order capillarity term in the Navier-Stokes-Korteweg equations which regularizes the singularity in the elliptic region. Indeed, this term can also assist us in regularizing the entropy function $\hat{\mathcal{H}}$ in such a way that we obtain well-defined entropy variables. In this direction, let us consider the following new mathematical entropy function:

$$\mathcal{H} = \hat{\mathcal{H}} + \frac{1}{2\mathbb{W}\mathrm{e}}|\nabla\rho|^2 = W(\rho) + \frac{1}{2}\rho|\mathbf{u}|^2 + \frac{1}{2\mathbb{W}\mathrm{e}}|\nabla\rho|^2. \tag{59}$$

The mathematical entropy function given by (59) coincides with the total energy density given by (40) and is no longer just a function but rather a functional of the conservation variables $\mathcal{U}$. Therefore, to define the entropy variables associated with the new mathematical entropy function, we take the variational derivative of $\mathcal{H}$ with respect to $\mathcal{U}$ to define $\mathcal{V}$. Under appropriate boundary conditions (e.g. $\nabla\rho \cdot \mathbf{n} = 0$ on $\partial\Omega$), this yields

$$\frac{\delta \mathcal{H}}{\delta \rho} = W'(\rho) - \frac{1}{2}|\mathbf{u}|^2 - \frac{1}{\mathbb{W}\mathrm{e}}\Delta\rho, \tag{60}$$

$$\frac{\delta \mathcal{H}}{\delta(\rho\mathbf{u})} = \mathbf{u}^T. \tag{61}$$

16

Notice that the capillarity regularization term results in the Laplace operator appearing in $\delta\mathcal{H}/\delta\rho$. The presence of this Laplace operator dictates that the change-of-variables back from entropy variables to conservation variables is non-local and involves the solution operator of the Laplace problem. To avoid the difficulties associated with such an operator, we introduce $\delta\mathcal{H}/\delta\rho$ as a new unknown v to our system:

$$v = W'(\rho) - \frac{1}{\mathbb{We}}\Delta\rho - \frac{|\mathbf{u}|^2}{2}. \tag{62}$$

By rearranging terms in (62) and taking the gradient of both sides, we obtain an interesting relationship between v and the pressure and capillarity terms appearing in the momentum equations:

$$\begin{aligned}
\nabla v + \nabla\frac{|\mathbf{u}|^2}{2} &= W''(\rho)\nabla\rho - \frac{1}{\mathbb{We}}\nabla\Delta\rho \\
&= \frac{p_{,\rho}}{\rho}\nabla\rho - \frac{1}{\mathbb{We}}\nabla\Delta\rho \\
&= \frac{1}{\rho}\left(\nabla p - \nabla\cdot\boldsymbol{\varsigma}\right).
\end{aligned} \tag{63}$$

The above relationship implies that the pressure and capillarity terms in the momentum balance equations can be replaced by terms involving v as follows:

$$\nabla p - \nabla\cdot\boldsymbol{\varsigma} = \rho\nabla v + \rho\nabla\frac{|\mathbf{u}|^2}{2}. \tag{64}$$

This inspires the following modified strong form of the isothermal Navier-Stokes-Korteweg equations in terms of ρ, $\mathbf{u}$, and v:

$$\frac{\partial\rho}{\partial t} + \nabla\cdot(\rho\mathbf{u}) = 0, \tag{65}$$

$$\frac{\partial(\rho\mathbf{u})}{\partial t} + \nabla\cdot(\rho\mathbf{u}\otimes\mathbf{u}) - \nabla\cdot\boldsymbol{\tau} + \rho\nabla v + \rho\nabla\frac{|\mathbf{u}|^2}{2} = \rho\mathbf{f}, \tag{66}$$

$$v = W'(\rho) - \frac{1}{\mathbb{We}}\Delta\rho - \frac{|\mathbf{u}|^2}{2}. \tag{67}$$

Equation (67) can be understood as a new variational equation-of-state. We remark that although some terms have been rewritten, (66) still provides a momentum balance law when coupled with (67).

3 Numerical Formulation

In this section, we present a numerical scheme for the isothermal Navier-Stokes-Korteweg equations based on the modified form given by (65)-(67). First, we show that the semi-discrete scheme based on a weighted residual formulation of (65)-(67) is entropy-stable in space. Next, we apply a new time integration scheme that inherits the entropy stability property in time. Last, we discuss implementational details.

3.1 Weak form of the isothermal Navier–Stokes–Korteweg equations

We begin this section with some standard notation (see, for example, [26]). Let $L^2(\Omega)$ be the space of square integrable functions over the domain Ω. Let $(\cdot, \cdot)_\Omega$ represent the L^2 inner product over the domain Ω and $(\cdot, \cdot)_\Gamma$ represent the L^2 inner product over the boundary Γ. Let $H^1(\Omega)$ denote the space of functions in $L^2(\Omega)$ with square integrable first-order derivatives. Finally, let $L^2(0, T; X)$ denote the space which consists of all strongly measurable functions $u : [0, T] \to X$ with

$$\|u\|_{L^2(0,T;X)} := \left(\int_0^T \|u(t)\|_X^2 \right)^{1/2} < \infty. \tag{68}$$

Our numerical scheme is based on the modified strong formulation (65)-(67). Let $\mathcal{V}_1$ denote the trial solution space for ρ, and let $\mathcal{V}_2$ denote the trial solution space for u_i such that $u_i \in \mathcal{V}_2$ implies $u_i = 0$ on Γ for each $i = 1, 2, 3$. We assume that $\mathcal{V}_1$ is also used as a trial solution space for v. We further assume the test function spaces coincide with the trial solution spaces. With these assumptions, the variational formulation for the isothermal Navier-Stokes-Korteweg system given by (65)-(67) is stated as follows:

Find $\rho(t) \in L^2(0, T; \mathcal{V}_1) \cap H^1(0, T; L^2(\Omega))$, $\mathbf{u}(t) = (u_1(t), u_2(t), u_3(t))^T \in (L^2(0, T; \mathcal{V}_2))^3 \cap (H^1(0, T; L^2(\Omega)))^3$, and $v(t) \in L^2(0, T; \mathcal{V}_1)$, such that:

$$\left(q_1, \frac{\partial \rho}{\partial t} \right)_\Omega - (\nabla q_1, \rho \mathbf{u})_\Omega = 0 \qquad \forall q_1 \in \mathcal{V}_1, \tag{69}$$

$$\left(\mathbf{q}, \mathbf{u} \frac{\partial \rho}{\partial t} + \rho \frac{\partial \mathbf{u}}{\partial t} \right)_\Omega - (\nabla \mathbf{q}, \rho \mathbf{u} \otimes \mathbf{u})_\Omega + (\mathbf{q}, \rho \nabla v)_\Omega + \left(\mathbf{q}, \rho \nabla \frac{|\mathbf{u}|^2}{2} \right)_\Omega$$
$$+ (\nabla \mathbf{q}, \boldsymbol{\tau})_\Omega = (\mathbf{q}, \rho \mathbf{f})_\Omega \qquad \forall \mathbf{q} = (q_2, q_3, q_4)^T \in (\mathcal{V}_2)^3, \tag{70}$$

$$(q_5, v)_\Omega = \left(q_5, W'(\rho) - \frac{|\mathbf{u}|^2}{2} \right)_\Omega + \frac{1}{\mathbb{We}} (\nabla q_5, \nabla \rho)_\Omega \qquad \forall q_5 \in \mathcal{V}_1, \tag{71}$$

with $\rho^h(0) = \rho_0^h$ and $\mathbf{u}^h(0) = \mathbf{u}_0^h$ in Ω.

Assuming sufficiently regular $\mathcal{V}_1$ and $\mathcal{V}_2$, integrating (69)-(71) by parts yields the Euler-Lagrange form of the variational problem:

$$\left(q_1, \frac{\partial \rho}{\partial t} \right)_\Omega + (q_1, \nabla \cdot (\rho \mathbf{u}))_\Omega - (q_1, \rho \mathbf{u} \cdot \mathbf{n})_\Gamma = 0, \tag{72}$$

$$\left(\mathbf{q}, \mathbf{u} \frac{\partial \rho}{\partial t} + \rho \frac{\partial \mathbf{u}}{\partial t} \right)_\Omega + (\mathbf{q}, \nabla (\rho \mathbf{u} \otimes \mathbf{u}))_\Omega + (\mathbf{q}, \rho \nabla v)_\Omega + \left(\mathbf{q}, \rho \nabla \frac{|\mathbf{u}|^2}{2} \right)_\Omega - (\mathbf{q}, \nabla \cdot \boldsymbol{\tau})_\Omega$$
$$- (\mathbf{q}, \rho \mathbf{u} \otimes \mathbf{u} \cdot \mathbf{n})_\Gamma - (\mathbf{q}, \boldsymbol{\tau} \cdot \mathbf{n})_\Gamma - (\mathbf{q}, \rho \mathbf{f})_\Omega = 0, \tag{73}$$

$$(q_5, v)_\Omega - \left(q_5, W'(\rho) + \frac{|\mathbf{u}|^2}{2} \right)_\Omega + \frac{1}{\mathbb{We}} (q_5, \Delta \rho)_\Omega - \frac{1}{\mathbb{We}} (q_5, \nabla \rho \cdot \mathbf{n})_\Gamma = 0. \tag{74}$$

18

Equations (72)-(74) enforce weak satisfaction of the differential equations given by (65)-(67) and the boundary conditions given by (3). The following theorem reveals that solutions of the variational problem given by (69)-(71) inherit the energy stability property of the strong form of the isothermal Navier-Stokes-Korteweg equations.

Theorem 2. *Sufficiently smooth weak solutions of the variational problem given by (69)-(71) verify the nonlinear stability condition (55).*

Proof. Since ρ and v share the same trial solution and test function spaces, we can take $q_1 = v$ in (69), $q_5 = \dfrac{\partial \rho}{\partial t}$ in (71), and perform integration by parts. This results in

$$\left(v, \frac{\partial \rho}{\partial t} \right)_\Omega - (\nabla v, \rho \mathbf{u})_\Omega = 0, \tag{75}$$

$$\left(\frac{\partial \rho}{\partial t}, v \right)_\Omega = (\rho_{,t}, W'(\rho) - \frac{|\mathbf{u}|^2}{2})_\Omega - \left(\rho_{,t}, \frac{1}{\mathbb{W}\mathrm{e}} \Delta \rho \right)_\Omega. \tag{76}$$

Now we subtract the first equation above from the second:

$$\left(\frac{\partial \rho}{\partial t}, W'(\rho) - \frac{|\mathbf{u}|^2}{2} - \frac{1}{\mathbb{W}\mathrm{e}} \Delta \rho \right)_\Omega = (\nabla v, \rho \mathbf{u})_\Omega. \tag{77}$$

Noting that $\dfrac{\delta \mathcal{H}}{\delta \rho} = W'(\rho) - \dfrac{|\mathbf{u}|^2}{2} - \dfrac{1}{\mathbb{W}\mathrm{e}} \Delta \rho$, we arrive at the following relation:

$$\frac{\delta \mathcal{E}}{\delta \rho} [\frac{\partial \rho}{\partial t}] := \left(\frac{\partial \rho}{\partial t}, \frac{\delta \mathcal{H}}{\delta \rho} \right)_\Omega = (\nabla v, \rho \mathbf{u})_\Omega. \tag{78}$$

Next, we take $\mathbf{q} = \mathbf{u}$ in (70):

$$\left(\mathbf{u}, \frac{\partial (\rho \mathbf{u})}{\partial t} \right)_\Omega - (\nabla \mathbf{u}, \rho \mathbf{u} \otimes \mathbf{u})_\Omega + (\mathbf{u}, \rho \nabla v)_\Omega + \left(\mathbf{u}, \rho \nabla \frac{|\mathbf{u}|^2}{2} \right)_\Omega + (\nabla \mathbf{u}, \boldsymbol{\tau})_\Omega = (\mathbf{u}, \rho \mathbf{f})_\Omega. \tag{79}$$

Noting that $\dfrac{\delta \mathcal{H}}{\delta (\rho \mathbf{u})} = \mathbf{u}^T$, the above equation implies that

$$\frac{\delta \mathcal{E}}{\delta (\rho \mathbf{u})} [\frac{\partial (\rho \mathbf{u})}{\partial t}] := \left(\frac{\partial (\rho \mathbf{u})}{\partial t}, \frac{\delta \mathcal{H}}{\delta (\rho \mathbf{u})} \right)_\Omega$$

$$= (\nabla \mathbf{u}, \rho \mathbf{u} \otimes \mathbf{u})_\Omega - (\mathbf{u}, \rho \nabla v)_\Omega - \left(\mathbf{u}, \rho \nabla \frac{|\mathbf{u}|^2}{2} \right)_\Omega - (\nabla \mathbf{u}, \boldsymbol{\tau})_\Omega + (\mathbf{u}, \rho \mathbf{f})_\Omega \tag{80}$$

Next, we use the chain rule and equations (78) and (80) to arrive at the following expression for the time derivative of the free energy $\mathcal{E}$:

$$\frac{d\mathcal{E}}{dt} = \frac{\delta \mathcal{E}}{\delta \rho} [\frac{\partial \rho}{\partial t}] + \frac{\delta \mathcal{E}}{\delta (\rho \mathbf{u})} [\frac{\partial (\rho \mathbf{u})}{\partial t}]$$

$$= (\nabla v, \rho \mathbf{u})_\Omega + (\nabla \mathbf{u}, \rho \mathbf{u} \otimes \mathbf{u})_\Omega - (\mathbf{u}, \rho \nabla v)_\Omega - \left(\mathbf{u}, \rho \nabla \frac{|\mathbf{u}|^2}{2} \right)_\Omega - (\nabla \mathbf{u}, \boldsymbol{\tau})_\Omega + (\mathbf{u}, \rho \mathbf{f})_\Omega$$

$$= (\nabla \mathbf{u}, \rho \mathbf{u} \otimes \mathbf{u})_\Omega - \left(\mathbf{u}, \rho \nabla \frac{|\mathbf{u}|^2}{2} \right)_\Omega - (\nabla \mathbf{u}, \boldsymbol{\tau})_\Omega + (\mathbf{u}, \rho \mathbf{f})_\Omega. \tag{81}$$

19

Simple calculation shows that

$$(\nabla \mathbf{u}, \rho \mathbf{u} \otimes \mathbf{u})_\Omega - \left(\mathbf{u}, \rho \nabla \frac{|\mathbf{u}|^2}{2}\right)_\Omega = 0. \tag{82}$$

Then (81) becomes:

$$\frac{d\mathcal{E}}{dt} = -(\nabla \mathbf{u}, \boldsymbol{\tau})_\Omega + (\mathbf{u}, \rho \mathbf{f})_\Omega. \tag{83}$$

In particular, when $\mathbf{f} = \mathbf{0}$, we have the dissipation inequality:

$$\frac{d\mathcal{E}}{dt} = -(\nabla \mathbf{u}, \boldsymbol{\tau})_\Omega \leq 0. \tag{84}$$

$\square$

Remark 8. *Theorem 2 together with Proposition 2 shows that the non-convex property is regularized by the non-local differential operator. The v variable is the non-local entropy variable for density. Here we do not directly perform the change-of-variable from ρ to v; instead, we weakly define the entropy variable v in terms of ρ and $\mathbf{u}$. Indeed, by resorting to such a "weak" way of defining the entropy variable, we avoid the prohibitive computational cost associated with inverting a differential operator.*

3.2 Semi-discrete formulation

To perform spatial discretization of (69)-(71), we make use of the Galerkin method [36]. Let $\mathcal{V}_1^h \subset \mathcal{V}_1$ and $\mathcal{V}_2^h \subset \mathcal{V}_2$ be finite dimensional function spaces spanned by finite element basis functions, where h-superscript denotes a mesh parameter. We approximate (69)-(71) in space as follows:

Find $\rho^h(t) \in L^2\left(0, T; \mathcal{V}_1^h\right) \cap H^1\left(0, T; L^2(\Omega)\right)$, $\mathbf{u}(t) = (u_1(t), u_2(t), u_3(t))^T \in \left(L^2\left(0, T; \mathcal{V}_2^h\right)\right)^3 \cap \left(H^1\left(0, T; L^2(\Omega)\right)\right)^3$, and $v(t) \in L^2\left(0, T; \mathcal{V}_1^h\right)$, such that:

$$\left(q_1^h, \frac{\partial \rho^h}{\partial t}\right)_\Omega - \left(\nabla q_1^h, \rho^h \mathbf{u}^h\right)_\Omega = 0 \qquad \forall q_1^h \in \mathcal{V}_1^h, \tag{85}$$

$$\left(\mathbf{q}^h, \mathbf{u}^h \frac{\partial \rho^h}{\partial t} + \rho^h \frac{\partial \mathbf{u}^h}{\partial t}\right)_\Omega - \left(\nabla \mathbf{q}^h, \rho^h \mathbf{u}^h \otimes \mathbf{u}^h\right)_\Omega + \left(\mathbf{q}^h, \rho^h \nabla v^h\right)_\Omega + \left(\mathbf{q}^h, \rho^h \nabla \frac{|\mathbf{u}^h|^2}{2}\right)_\Omega$$
$$+ \left(\nabla \mathbf{q}^h, \boldsymbol{\tau}(\mathbf{u}^h)\right)_\Omega = \left(\mathbf{q}^h, \rho \mathbf{f}\right)_\Omega \qquad \forall \mathbf{q}^h = (q_2^h, q_3^h, q_4^h)^T \in \left(\mathcal{V}_2^h\right)^3, \tag{86}$$

$$\left(q_5^h, v^h\right)_\Omega = \left(q_5^h, W'(\rho^h) - \frac{|\mathbf{u}^h|^2}{2}\right)_\Omega + \frac{1}{\mathbb{W}\mathrm{e}}\left(\nabla q_5^h, \nabla \rho^h\right)_\Omega \qquad \forall q_5^h \in \mathcal{V}_1^h, \tag{87}$$

with $\rho^h(0) = \rho_0^h$ and $\mathbf{u}^h(0) = \mathbf{u}_0^h$ in Ω.

Above, ρ_0^h and $\mathbf{u}_0^h$ are L^2-projections of $\rho_0(x)$, $\mathbf{u}_0(x)$ onto $\mathcal{V}_1^h$ and $(\mathcal{V}_2^h)^3$ respectively. By employing the same method as was used to prove Theorem 2, we can show that the semi-discrete problem inherits the energy stability property of the strong form of the isothermal Navier-Stokes-Korteweg equations.

Theorem 3. *Solutions of the semi-discrete variational problem given by (85)-(87) verify the nonlinear stability condition (55).*

Remark 9. *To guarantee discrete mass conservation, it is sufficient to require $1 \in \mathcal{V}_1^h$.*

Remark 10. *If $\mathcal{V}_1^h$ has the property*

$$\forall \rho^h \in \mathcal{V}_1^h, \quad \nabla \rho^h \in (\mathcal{V}_1^h)^3, \tag{88}$$

we have the following relation by performing integration by parts:

$$\int_\Omega \rho^h \nabla v^h + \rho^h \nabla \frac{|\mathbf{u}^h|^2}{2} d\mathbf{x} = \int_\Gamma \rho^h \left(v^h - W'(\rho^h) + \frac{|\mathbf{u}|^2}{2} + \frac{1}{\mathbb{W}\mathrm{e}} \Delta \rho^h \right) \mathbf{n} ds$$
$$+ \int_\Omega \nabla p d\mathbf{x} - \int_\Omega \nabla \cdot \varsigma d\mathbf{x}. \tag{89}$$

If we further assume that ρ^h and v^h satisfy periodic boundary conditions, the first boundary integral becomes 0, and we have

$$\int_\Omega \rho^h \nabla v^h + \rho^h \nabla \frac{|\mathbf{u}^h|^2}{2} d\mathbf{x} = \int_\Gamma p\mathbf{n} - \varsigma \cdot \mathbf{n} ds. \tag{90}$$

The requirement (88) can be satisfied if $\mathcal{V}_1^h$ is spanned by trigonometric polynomials. Therefore, if $1 \in \mathcal{V}_2^h$, ρ and v satisfy periodic boundary conditions, and we use a spectral method based on trigonometric polynomials for $\mathcal{V}_1^h$, we can obtain discrete momentum conservation.

Remark 11. *Henceforth, we use the same discrete space (up to prescription of boundary conditions) for ρ^h, u_i^h, $i = 1, 2, 3$, and v^h, i.e. we assume that $\mathcal{V}_1^h = \mathcal{V}_2^h = \mathcal{V}^h$.*

Remark 12. *We utilize Non-Uniform Rational B-Splines (NURBS) basis functions to define the discrete spaces. Making use of NURBS basis functions and the isoparametric concept has led to the concept of Isogeometric Analysis. It has been shown that isogeometric analysis possesses several advantages over traditional finite element methods in terms of approximation accuracy [19, 24], robustness [49], and mesh generation [4, 37]. Additionally, it has been successfully applied to various fluid problems [5, 6, 25] and phase-field models [30, 32]. For a general discussion of isogeometric analysis, the reader is referred to [18].*

3.3 Energy-stable time integration scheme for Isothermal Navier–Stokes–Korteweg equations

Now that we have a provably energy-stable semi-discrete formulation, it remains to discretize in time. As was mentioned previously in Section 1.2, the weighted residual form of the symmetrized Navier-Stokes equations in terms of classical entropy variables in conjunction with a space-time formulation constitutes a fully discrete scheme which is provably unconditionally stable-in-energy [58, 59]. Unfortunately, classical entropy variables do not comprise a viable variable set in the context of a van der Waals fluid. Moreover, the stability of the space-time formulation in the context of the symmetrized Navier-Stokes equations is contingent upon

21

the fact that the Jacobian matrix describing the mapping from conservation variables to classical entropy variables is positive definite. In the context of the van der Waals fluid model, the Jacobian matrix can be singular or even negative definite within the elliptic region. This is due to the non-convexity of the classical mathematical entropy function within the elliptic region.

Perhaps the simplest second-order time-marching scheme for time-dependent systems is the mid-point rule. In fact, for some nonlinear systems such as the incompressible Navier-Stokes equations, the application of the mid-point rule to a provably energy-stable semi-discrete formulation will lead to a provably energy-stable fully discrete formulation. Unfortunately, this is not true for the isothermal Navier-Stokes-Korteweg system studied here. The primary issue in deriving a finite-difference time-discretization scheme for this system lies with approximating the chemical potential at a particular time step. A simple evaluation of the chemical potential using the mid-point rule is generally unstable. An alternative and somewhat appealing methodology is inspired by the fact that the chemical potential is precisely the derivative of the free energy function with respect to the density field. Hence, one may approximate the chemical potential at time $t_{n+1/2} = \frac{1}{2}(t_{n+1} + t_n)$ using the finite difference formula

$$\mu(t_{n+1/2}) \approx \frac{W(\rho_{n+1}^h) - W(\rho_n^h)}{\rho_{n+1}^h - \rho_n^h} \tag{91}$$

where ρ_n^h and ρ_{n+1}^h are discrete approximations of the density field at time-steps t_n and t_{n+1} respectively. Indeed, one can show that a time-marching scheme in which the above formula is used to approximate the chemical potential while all other terms are approximated using a variant of the mid-point rule is energy-stable and in fact energy-conservative in the inviscid setting. Unfortunately, the finite difference approximation given by (91) is ill-defined when $\rho_{n+1} = \rho_n$ and numerical tests have revealed it is unstable when $\rho_{n+1} \approx \rho_n$. When the free energy function is polynomial, an equivalent and numerically stable representation of (91) can be recovered using a truncated Taylor expansion of the form

$$\frac{W(\rho_{n+1}^h) - W(\rho_n^h)}{\rho_{n+1}^h - \rho_n^h} = \sum_{i=0}^{n} \frac{1}{2^{2i}(2i+1)!} \frac{d^{2i}\mu\left(\rho_{n+1/2}^h\right)}{d\rho^{2i}} [\![\rho_n^h]\!]^{2i} \tag{92}$$

where

$$[\![\rho_n^h]\!] = \rho_{n+1}^h - \rho_n^h \text{ and } \rho_{n+1/2}^h = \frac{1}{2}\left(\rho_n^h + \rho_{n+1}^h\right), \tag{93}$$

but in the non-polynomial setting, such an expansion results in fully discrete schemes which are no longer provably energy-stable. Hence, one is left with the question: how can one approximate the finite difference approximation given by (91) in such a manner that energy stability is not upset? It turns out that one can do so by employing the following specialized quadrature formulas which were introduced by Gomez and Hughes in [31] in order to develop an energy-stable fully discrete scheme for the Cahn-Hilliard equation.

Lemma 2. *(Perturbed trapezoidal rules) For a function $f \in C^3([a,b])$, there exists $\xi_1, \xi_2 \in$*

22

(a, b) *such that the following quadrature formulas hold true*

$$\int_a^b f(x)dx = \frac{b-a}{2}(f(a) + f(b)) - \frac{(b-a)^3}{12}f''(a) - \frac{(b-a)^4}{24}f'''(\xi_1), \tag{94}$$

$$\int_a^b f(x)dx = \frac{b-a}{2}(f(a) + f(b)) - \frac{(b-a)^3}{12}f''(b) + \frac{(b-a)^4}{24}f'''(\xi_2). \tag{95}$$

Proof. The original proof was given in the appendix of [31]. □

Using the above lemma, we can write

$$\frac{W(\rho_{n+1}^h) - W(\rho_n^h)}{\rho_{n+1}^h - \rho_n^h} = \frac{1}{\rho_{n+1}^h - \rho_n^h}\int_{\rho_n^h}^{\rho_{n+1}^h} W'(\rho)d\rho$$

$$= \frac{1}{\rho_{n+1}^h - \rho_n^h}\int_{\rho_n^h}^{\rho_{n+1}^h} \mu(\rho)d\rho$$

$$= \frac{1}{2}(\mu(\rho_n^h) + \mu(\rho_{n+1}^h)) - \frac{[\![\rho_n^h]\!]^2}{12}\mu''(\rho_n^h) - \frac{[\![\rho_n^h]\!]^3}{24}\mu'''(\rho_{n+\xi}^h) \tag{96}$$

for some $\xi \in (0, 1)$ where $\rho_{n+\xi}^h = (1-\xi)\rho_n^h + \xi\rho_{n+1}^h$. This inspires the following approximation of the chemical potential at time $t_{n+1/2} = \frac{1}{2}(t_{n+1} + t_n)$:

$$\mu(t_{n+1/2}) \approx \frac{1}{2}(\mu(\rho_n^h) + \mu(\rho_{n+1}^h)) - \frac{[\![\rho_n^h]\!]^2}{12}\mu''(\rho_n^h). \tag{97}$$

We see that the above approximation is a perturbation of the stable approximation given in (91) by a factor of $-\frac{[\![\rho_n^h]\!]^3}{24}\mu'''(\rho_{n+\xi}^h)$, and this in turn is a stable perturbation as the free energy function for a van der Waal's fluid is super-convex.

Remark 13. *The quadrature formulas (94) and (95) can be viewed as a perturbation of the trapezoidal rule. We note that there are other quadrature rules that can be utilized to generate nonlinear stable numerical schemes as well. Two additional quadrature rules with proofs and their application in the isothermal Navier-Stokes-Korteweg equations are given in appendix A and B.*

With the approximation given by (97), we are now ready to describe in full the proposed time integration scheme. Let us assume that the time interval is $\mathcal{I} = (0, T)$ is divided into N_{ts} subintervals $\mathcal{I}_n = (t_n, t_{n+1})$, $n = 0, \cdots, N_{ts} - 1$. We use the notation ρ_{n+1}^h, $\mathbf{u}_{n+1}^h = (u_{1,n+1}^h, u_{2,n+1}^h, u_{3,n+1}^h)^T$, and v_{n+1}^h to represent the fully discrete solutions at time level $n + 1$. In each time step, given ρ_n^h, $\mathbf{u}_n^h$ and v_n^h, we need to find ρ_{n+1}^h, $\mathbf{u}_{n+1}^h$ and v_{n+1}^h such that for all q_1^h, $q_5^h \in \mathcal{V}^h$, and $\mathbf{q}^h = (q_1^h, q_2^h, q_3^h) \in (\mathcal{V}^h)^3$,

$$\mathbf{B}^M(q_1^h; \rho_{n+1}^h, \mathbf{u}_{n+1}^h, v_{n+1}^h) := \left(q_1^h, \frac{[\![\rho_n^h]\!]}{\Delta t_n}\right)_\Omega - \left(\nabla q_1^h, \rho_{n+\frac{1}{2}}^h \mathbf{u}_{n+\frac{1}{2}}^h\right)_\Omega = 0, \tag{98}$$

$$\mathbf{B}^{\mathbf{U}}(\mathbf{q}^h; \rho_{n+1}^h, \mathbf{u}_{n+1}^h, v_{n+1}^h) := \left(\mathbf{q}^h, \mathbf{u}_{n+\frac{1}{2}}^h \frac{[\![\rho_n^h]\!]}{\Delta t_n} + \rho_{n+\frac{1}{2}}^h \frac{[\![\mathbf{u}_n^h]\!]}{\Delta t_n}\right)_\Omega - \left(\nabla \mathbf{q}^h, \rho_{n+\frac{1}{2}}^h \mathbf{u}_{n+\frac{1}{2}}^h \otimes \mathbf{u}_{n+\frac{1}{2}}^h\right)_\Omega$$
$$+ \left(\nabla \mathbf{q}^h, \boldsymbol{\tau}(\mathbf{u}_{n+\frac{1}{2}}^h)\right)_\Omega + \left(\mathbf{q}^h, \rho_{n+\frac{1}{2}}^h \nabla v_{n+1}^h + \rho_{n+\frac{1}{2}}^h \nabla(\frac{|\mathbf{u}_{n+\frac{1}{2}}^h|^2}{2})\right)_\Omega = 0, \tag{99}$$

$$\mathbf{B}^E(q_5^h; \rho_{n+1}^h, \mathbf{u}_{n+1}^h, v_{n+1}^h) := \left(q_5^h, v_{n+1}^h\right)_\Omega - \left(q_5^h, \frac{1}{2}(\mu(\rho_n^h) + \mu(\rho_{n+1}^h)) - \frac{[\![\rho_n^h]\!]^2}{12}\mu''(\rho_n^h)\right)_\Omega$$
$$+ \left(q_5^h, \frac{2|\mathbf{u}_{n+\frac{1}{2}}^h|^2 - |\mathbf{u}^h|_{n+\frac{1}{2}}^2}{2}\right)_\Omega - \left(\nabla q_5^h, \frac{1}{\mathbb{W}\mathrm{e}}\nabla \rho_{n+\alpha}^h\right)_\Omega = 0, \tag{100}$$

where

$$\Delta t_n = t_{n+1} - t_n, \tag{101}$$

$$\rho_{n+\alpha}^h = \rho_n^h + \alpha[\![\rho_n^h]\!], \tag{102}$$

$$\alpha = 1/2 + \eta, \tag{103}$$

$$\eta = \frac{1}{2}\tanh(\frac{\Delta t_n \mathbb{W}\mathrm{e}^{\frac{1}{2}}}{\mathcal{C}}). \tag{104}$$

As will become evident later, the parameter $\mathcal{C}$ appearing above is a non-dimensional constant that can be used to adjust the dissipation of our proposed time integration scheme. The quantity $\mathbb{W}\mathrm{e}^{1/2}$ in (104) will ensure that the dissipation varies according to the choices of length scale L_0. The following theorem states that our scheme is provably energy-stable, mass-conservative, and second-order accurate in time.

Theorem 4. *The fully discrete variational formulation (98)-(104) satisfies the following properties:*

(1) The scheme is mass-conservative, i.e.,

$$\int_\Omega \rho_n^h d\mathbf{x} = \int_\Omega \rho_0^h d\mathbf{x}, \qquad \forall n = 1, \cdots, N_{ts}. \tag{105}$$

(2) The scheme verifies the nonlinear stability condition

$$\mathcal{E}(\rho_n^h, \mathbf{u}_n^h) \leq \mathcal{E}(\rho_{n-1}^h, \mathbf{u}_{n-1}^h), \qquad \forall n = 1, \cdots, N_{ts}. \tag{106}$$

(3) The local truncation error in time $\tau(t)$ may be bounded by $|\tau(t_n)| \leq K\Delta t_n^2$ for all $t_n \in [0, T]$, where K is a constant independent of Δt_n.

Proof. (1) Taking $q_1^h = 1$ in equation (98), we obtain:

$$\left(1, \frac{[\![\rho_n^h]\!]}{\Delta t_n}\right)_\Omega = \frac{1}{\Delta t}\left(\int_\Omega \rho_{n+1}^h d\mathbf{x} - \int_\Omega \rho_n^h d\mathbf{x}\right)_\Omega = 0. \tag{107}$$

By induction, we have:

$$\int_\Omega \rho_n^h d\mathbf{x} = \int_\Omega \rho_0^h d\mathbf{x}. \tag{108}$$

(2) As a result of (96), we have:

$$\frac{[\![W(\rho_n^h)]\!]}{[\![\rho_n^h]\!]} + \frac{[\![\rho_n^h]\!]^3}{24}\mu'''(\rho_{n+\xi}^h) = \frac{1}{2}(\mu(\rho_n^h) + \mu(\rho_{n+1}^h)) - \frac{[\![\rho_n^h]\!]^2}{12}\mu''(\rho_n^h) \qquad \xi \in (0,1). \tag{109}$$

Now let us take $q_1^h = v_{n+1}^h$ in equation (98) and $q_5^h = [\![\rho_n^h]\!]/\Delta t_n$ in equation (100) to obtain

$$\left(v_{n+1}^h, \frac{[\![\rho_n^h]\!]}{\Delta t_n}\right)_\Omega - \left(\nabla v_{n+1}^h, \rho_{n+\frac{1}{2}}^h \mathbf{u}_{n+\frac{1}{2}}^h\right)_\Omega = 0 \tag{110}$$

and

$$\left(\frac{[\![\rho_n^h]\!]}{\Delta t_n}, v_{n+1}^h\right)_\Omega - \left(\frac{[\![\rho_n^h]\!]}{\Delta t_n}, \frac{1}{2}(\mu(\rho_n^h) + \mu(\rho_{n+1}^h)) - \frac{[\![\rho_n^h]\!]^2}{12}\mu''(\rho_n^h)\right)_\Omega$$
$$+ \left(\frac{[\![\rho_n^h]\!]}{\Delta t_n}, \frac{2|\mathbf{u}_{n+\frac{1}{2}}^h|^2 - |\mathbf{u}^h|_{n+\frac{1}{2}}^2}{2}\right)_\Omega - \left(\nabla\frac{[\![\rho_n^h]\!]}{\Delta t_n}, \frac{1}{\mathbb{We}}\nabla\rho_{n+\alpha}^h\right)_\Omega = 0. \tag{111}$$

Combining equations (110) and (111) by canceling the term $\left(v_{n+1}^h, \frac{[\![\rho_n^h]\!]}{\Delta t_n}\right)_\Omega$ yields

$$\left(\nabla v_{n+1}^h, \rho_{n+\frac{1}{2}}^h \mathbf{u}_{n+\frac{1}{2}}^h\right)_\Omega - \left(\frac{[\![\rho_n^h]\!]}{\Delta t_n}, \frac{1}{2}(\mu(\rho_n^h) + \mu(\rho_{n+1}^h)) - \frac{[\![\rho_n^h]\!]^2}{12}\mu''(\rho_n^h)\right)_\Omega$$
$$+ \left(\frac{[\![\rho_n^h]\!]}{\Delta t_n}, \frac{2|\mathbf{u}_{n+\frac{1}{2}}^h|^2 - |\mathbf{u}^h|_{n+\frac{1}{2}}^2}{2}\right)_\Omega - \left(\nabla\frac{[\![\rho_n^h]\!]}{\Delta t_n}, \frac{1}{\mathbb{We}}\nabla\rho_{n+\alpha}^h\right)_\Omega = 0. \tag{112}$$

Due to the relation given by (109), the second term in (112) can be written as

$$\left(\frac{[\![\rho_n^h]\!]}{\Delta t_n}, \frac{1}{2}(\mu(\rho_n^h) + \mu(\rho_{n+1}^h)) - \frac{[\![\rho_n^h]\!]^2}{12}\mu''(\rho_n^h)\right)_\Omega = \left(\frac{[\![\rho_n^h]\!]}{\Delta t_n}, \frac{[\![W(\rho_n^h)]\!]}{[\![\rho_n^h]\!]} + \frac{[\![\rho_n^h]\!]^3}{24}\mu'''(\rho_{n+\xi}^h)\right)_\Omega$$
$$= \int_\Omega \frac{[\![W(\rho_n^h)]\!]}{\Delta t_n}d\mathbf{x} + \left(\frac{[\![\rho_n^h]\!]}{\Delta t_n}, \frac{[\![\rho_n^h]\!]^3}{24}\mu'''(\rho_{n+\xi}^h)\right)_\Omega, \tag{113}$$

and the last term in (112) can be rewritten as

$$\left(\nabla\frac{[\![\rho_n^h]\!]}{\Delta t_n}, \frac{1}{\mathbb{We}}\nabla\rho_{n+\alpha}^h\right)_\Omega = \left(\nabla[\![\rho_n^h]\!], \frac{1}{\mathbb{We}\Delta t_n}\nabla\rho_{n+\frac{1}{2}}^h\right)_\Omega + \left(\nabla[\![\rho_n^h]\!], \frac{\eta}{\mathbb{We}\Delta t_n}\nabla[\![\rho_n^h]\!]\right)_\Omega$$
$$= \int_\Omega \frac{1}{2\mathbb{We}\Delta t_n}[\![|\nabla\rho^h|_n^2]\!]d\mathbf{x} + \left(\nabla[\![\rho_n^h]\!], \frac{\eta}{\mathbb{We}\Delta t_n}\nabla[\![\rho_n^h]\!]\right)_\Omega. \tag{114}$$

25

Therefore, equation (112) can be rewritten as

$$
(\nabla v_{n+1}^h, \rho_{n+\frac{1}{2}}^h \mathbf{u}_{n+\frac{1}{2}}^h)_\Omega - \left(\frac{[\![\rho_n^h]\!]}{\Delta t_n}, \frac{[\![\rho_n^h]\!]^3}{24} \mu'''(\rho_{n+\xi}^h) \right)_\Omega + \left(\frac{[\![\rho_n^h]\!]}{\Delta t_n}, \frac{2|\mathbf{u}_{n+\frac{1}{2}}^h|^2 - |\mathbf{u}^h|_{n+\frac{1}{2}}^2}{2} \right)_\Omega
$$

$$
- \int_\Omega \frac{[\![W(\rho_n^h)]\!]}{\Delta t_n} d\mathbf{x} - \int_\Omega \frac{1}{2\mathbb{W}e\Delta t_n} [\![|\nabla\rho^h|_n^2]\!] d\mathbf{x} - \left(\nabla[\![\rho_n^h]\!], \frac{\eta}{\mathbb{W}e\Delta t_n}\nabla[\![\rho_n^h]\!] \right)_\Omega = 0. \qquad (115)
$$

Next, let us take $\mathbf{q}^h = \mathbf{u}_{n+\frac{1}{2}}^h$ in equation (99):

$$
\left(\mathbf{u}_{n+\frac{1}{2}}^h, \mathbf{u}_{n+\frac{1}{2}}^h \frac{[\![\rho_n^h]\!]}{\Delta t_n} + \rho_{n+\frac{1}{2}} \frac{[\![\mathbf{u}_n^h]\!]}{\Delta t_n} \right)_\Omega - (\nabla \mathbf{u}_{n+\frac{1}{2}}^h, \rho_{n+\frac{1}{2}}\mathbf{u}_{n+\frac{1}{2}} \otimes \mathbf{u}_{n+\frac{1}{2}})_\Omega + (\nabla \mathbf{u}_{n+\frac{1}{2}}^h, \boldsymbol{\tau}(\mathbf{u}_{n+\frac{1}{2}}^h))_\Omega
$$

$$
+ \left(\mathbf{u}_{n+\frac{1}{2}}^h, \rho_{n+\frac{1}{2}}\nabla v_{n+1}^h + \rho_{n+\frac{1}{2}}\nabla(\frac{|\mathbf{u}_{n+\frac{1}{2}}^h|^2}{2}) \right)_\Omega = 0. \qquad (116)
$$

Subtracting (115) from (116) yields

$$
- (\nabla v_{n+1}^h, \rho_{n+\frac{1}{2}}^h \mathbf{u}_{n+\frac{1}{2}}^h)_\Omega + \left(\frac{[\![\rho_n^h]\!]}{\Delta t_n}, \frac{[\![\rho_n^h]\!]^3}{24} \mu'''(\rho_{n+\xi}^h) \right)_\Omega - \left(\frac{[\![\rho_n^h]\!]}{\Delta t_n}, \frac{2|\mathbf{u}_{n+\frac{1}{2}}^h|^2 - |\mathbf{u}^h|_{n+\frac{1}{2}}^2}{2} \right)_\Omega
$$

$$
+ \int_\Omega \frac{[\![W(\rho_n^h)]\!]}{\Delta t_n} d\mathbf{x} + \int_\Omega \frac{1}{2\mathbb{W}e\Delta t_n} [\![|\nabla\rho^h|_n^2]\!] d\mathbf{x} + \left(\nabla[\![\rho_n^h]\!], \frac{\eta}{\mathbb{W}e\Delta t_n}\nabla[\![\rho_n^h]\!] \right)_\Omega
$$

$$
+ \left(\mathbf{u}_{n+\frac{1}{2}}^h, \mathbf{u}_{n+\frac{1}{2}}^h \frac{[\![\rho_n^h]\!]}{\Delta t_n} + \rho_{n+\frac{1}{2}} \frac{[\![\mathbf{u}_n^h]\!]}{\Delta t_n} \right)_\Omega - (\nabla \mathbf{u}_{n+\frac{1}{2}}^h, \rho_{n+\frac{1}{2}}\mathbf{u}_{n+\frac{1}{2}} \otimes \mathbf{u}_{n+\frac{1}{2}})_\Omega + (\nabla \mathbf{u}_{n+\frac{1}{2}}^h, \boldsymbol{\tau}(\mathbf{u}_{n+\frac{1}{2}}^h))_\Omega
$$

$$
+ \left(\mathbf{u}_{n+\frac{1}{2}}^h, \rho_{n+\frac{1}{2}}\nabla v_{n+1}^h + \rho_{n+\frac{1}{2}}\nabla(\frac{|\mathbf{u}_{n+\frac{1}{2}}^h|^2}{2}) \right)_\Omega = 0. \qquad (117)
$$

Noticing that

$$
- \left(\frac{[\![\rho_n^h]\!]}{\Delta t_n}, \frac{2|\mathbf{u}_{n+\frac{1}{2}}^h|^2 - |\mathbf{u}^h|_{n+\frac{1}{2}}^2}{2} \right)_\Omega + \left(\mathbf{u}_{n+\frac{1}{2}}^h, \mathbf{u}_{n+\frac{1}{2}}^h \frac{[\![\rho_n^h]\!]}{\Delta t_n} + \rho_{n+\frac{1}{2}} \frac{[\![\mathbf{u}_n^h]\!]}{\Delta t_n} \right)_\Omega
$$

$$
= \int_\Omega \frac{[\![\rho_n^h]\!]|\mathbf{u}^h|_{n+\frac{1}{2}}^2}{2\Delta t_n} + \frac{\rho_{n+\frac{1}{2}}^h[\![|\mathbf{u}^h|_n^2]\!]}{2\Delta t_n} d\mathbf{x}
$$

$$
= \int_\Omega \frac{1}{\Delta t_n} [\![\rho_n^h \frac{|\mathbf{u}^h|_n^2}{2}]\!] d\mathbf{x} \qquad (118)
$$

and

$$
(\nabla \mathbf{u}_{n+\frac{1}{2}}^h, \rho_{n+\frac{1}{2}}\mathbf{u}_{n+\frac{1}{2}} \otimes \mathbf{u}_{n+\frac{1}{2}})_\Omega - \left(\mathbf{u}_{n+\frac{1}{2}}^h, \rho_{n+\frac{1}{2}}\nabla(\frac{|\mathbf{u}_{n+\frac{1}{2}}^h|^2}{2}) \right)_\Omega = 0 \qquad (119)
$$

$$
- (\nabla v_{n+1}^h, \rho_{n+\frac{1}{2}}^h \mathbf{u}_{n+\frac{1}{2}}^h)_\Omega + (\mathbf{u}_{n+\frac{1}{2}}^h, \rho_{n+\frac{1}{2}}\nabla v_{n+1}^h)_\Omega = 0, \qquad (120)
$$

26

equation (117) implies

$$\frac{[\![\mathcal{E}(\rho_n^h, \mathbf{u}_n^h)]\!]}{\Delta t_n} = \frac{1}{\Delta t_n} \int_\Omega [\![\rho_n^h \frac{|\mathbf{u}^h|_n^2}{2}]\!] + [\![W(\rho_n^h)]\!] + \frac{1}{2\mathbb{We}}[\![|\nabla \rho^h|_n^2]\!] d\mathbf{x}$$

$$= -(\nabla \mathbf{u}_{n+\frac{1}{2}}^h, \boldsymbol{\tau}(\mathbf{u}_{n+\frac{1}{2}}^h))_\Omega - \left(\frac{[\![\rho_n^h]\!]}{\Delta t_n}, \frac{[\![\rho_n^h]\!]^3}{24} \mu'''(\rho_{n+\xi}^h)\right)_\Omega - \left(\nabla[\![\rho_n^h]\!], \frac{\eta}{\mathbb{We}\Delta t_n}\nabla[\![\rho_n^h]\!]\right)_\Omega$$

$$\leq 0. \tag{121}$$

The last inequality is due to Proposition 1 and super-convexity, that is, $\mu''' = W'''' > 0$.

(3) We consider the mid-point rule applied for the semi-discrete formulation (69)-(71):

$$\left(q_1^h, \frac{[\![\rho_n^h]\!]}{\Delta t}\right)_\Omega - \left(\nabla q_1^h, \rho_{n+\frac{1}{2}}^h \mathbf{u}_{n+\frac{1}{2}}^h\right)_\Omega = 0, \tag{122}$$

$$\left(\mathbf{q}^h, \mathbf{u}_{n+\frac{1}{2}}^h \frac{[\![\rho_n^h]\!]}{\Delta t_n} + \rho_{n+\frac{1}{2}}^h \frac{[\![\mathbf{u}_n^h]\!]}{\Delta t_n}\right)_\Omega - \left(\nabla \mathbf{q}^h, \rho_{n+\frac{1}{2}}^h \mathbf{u}_{n+\frac{1}{2}} \otimes \mathbf{u}_{n+\frac{1}{2}}\right)_\Omega + \left(\nabla \mathbf{q}^h, \boldsymbol{\tau}(\mathbf{u}_{n+\frac{1}{2}}^h)\right)_\Omega$$

$$+ \left(\mathbf{q}^h, \rho_{n+\frac{1}{2}} \nabla v_{mid}^h + \rho_{n+\frac{1}{2}} \nabla(\frac{|\mathbf{u}_{n+\frac{1}{2}}^h|^2}{2})\right)_\Omega = 0, \tag{123}$$

$$\left(q_5^h, v_{mid}^h\right)_\Omega - \left(q_5^h, \mu(\rho_{n+\frac{1}{2}}^h)\right)_\Omega + \left(q_5^h, \frac{|\mathbf{u}_{n+\frac{1}{2}}^h|^2}{2}\right)_\Omega - \left(\nabla q_5^h, \frac{1}{\mathbb{We}}\nabla \rho_{n+\frac{1}{2}}^h\right)_\Omega = 0. \tag{124}$$

The local truncation error associated with the mid-point rule can be obtained by replacing the time discrete solution $\rho_n^h, \mathbf{u}_n^h$ with the corresponding exact time continuous solution $\rho^h(t_n), \mathbf{u}^h(t_n)$ in the above equations and performing Taylor expansions:

$$\left(q_1^h, \frac{[\![\rho^h(t_n)]\!]}{\Delta t}\right)_\Omega - \left(\nabla q_1^h, \rho^h(t_{n+\frac{1}{2}})\mathbf{u}^h(t_{n+\frac{1}{2}})\right)_\Omega = \left(q_1^h, \varpi_\rho^{mid}\right)_\Omega, \tag{125}$$

$$\left(\mathbf{q}^h, \mathbf{u}^h(t_{n+\frac{1}{2}})\frac{[\![\rho^h(t_n)]\!]}{\Delta t_n} + \rho^h(t_{n+\frac{1}{2}})\frac{[\![\mathbf{u}^h(t_n)]\!]}{\Delta t_n}\right)_\Omega - \left(\nabla \mathbf{q}^h, \rho^h(t_{n+\frac{1}{2}})\mathbf{u}^h(t_{n+\frac{1}{2}}) \otimes \mathbf{u}^h(t_{n+\frac{1}{2}})\right)_\Omega$$

$$+ \left(\nabla \mathbf{q}^h, \boldsymbol{\tau}(\mathbf{u}^h(t_{n+\frac{1}{2}}))\right)_\Omega + \left(\mathbf{q}^h, \rho^h(t_{n+\frac{1}{2}})\nabla \tilde{v}_{mid}^h + \rho^h(t_{n+\frac{1}{2}})\nabla(\frac{|\mathbf{u}^h(t_{n+\frac{1}{2}})|^2}{2})\right)_\Omega = \left(\mathbf{q}^h, \boldsymbol{\varpi}_\mathbf{u}^{mid}\right)_\Omega, \tag{126}$$

$$\left(q_5^h, \tilde{v}_{mid}^h\right)_\Omega - \left(q_5^h, \mu(\rho^h(t_{n+\frac{1}{2}}))\right)_\Omega + \left(q_5^h, \frac{|\mathbf{u}^h(t_{n+\frac{1}{2}})|^2}{2}\right)_\Omega - \left(\nabla q_5^h, \frac{1}{\mathbb{We}}\nabla \rho^h(t_{n+\frac{1}{2}})\right)_\Omega = 0, \tag{127}$$

where ϖ_ρ^{mid} and $\boldsymbol{\varpi}_\mathbf{u}^{mid}$ are the local truncation errors. Assuming sufficient smoothness, Taylor expansions of the time continuous solutions lead to

$$\varpi_\rho^{mid} = \mathcal{O}(\Delta t_n^2), \quad \boldsymbol{\varpi}_\mathbf{u}^{mid} = \mathcal{O}(\Delta t_n^2)\mathbf{1}. \tag{128}$$

27

This calculation verifies the second-order accuracy of the midpoint rule. Now we consider our time discrete scheme (98)-(100). Replacing the time discrete solution with the time continuous solution, we obtain the following:

$$\left(q_1^h, \frac{[\![\rho^h(t_n)]\!]}{\Delta t}\right)_\Omega - \left(\nabla q_1^h, \rho^h(t_{n+\frac{1}{2}})\mathbf{u}^h(t_{n+\frac{1}{2}})\right)_\Omega = \left(q_1^h, \varpi_\rho\right)_\Omega, \tag{129}$$

$$\left(\mathbf{q}^h, \mathbf{u}^h(t_{n+\frac{1}{2}})\frac{[\![\rho^h(t_n)]\!]}{\Delta t_n} + \rho^h(t_{n+\frac{1}{2}})\frac{[\![\mathbf{u}^h(t_n)]\!]}{\Delta t_n}\right)_\Omega$$

$$- \left(\nabla\mathbf{q}^h, \rho^h(t_{n+\frac{1}{2}})\mathbf{u}^h(t_{n+\frac{1}{2}}) \otimes \mathbf{u}^h(t_{n+\frac{1}{2}})\right)_\Omega + \left(\nabla\mathbf{q}^h, \boldsymbol{\tau}(\mathbf{u}^h(t_{n+\frac{1}{2}}))\right)_\Omega$$

$$+ \left(\mathbf{q}^h, \rho^h(t_{n+\frac{1}{2}})\nabla\tilde{v}^h + \rho^h(t_{n+\frac{1}{2}})\nabla(\frac{|\mathbf{u}^h(t_{n+\frac{1}{2}})|^2}{2})\right)_\Omega = \left(\mathbf{q}^h, \varpi_\mathbf{u}\right)_\Omega, \tag{130}$$

$$\left(q_5^h, \tilde{v}^h\right)_\Omega - \left(q_5^h, \frac{1}{2}\left(\mu(\rho^h(t_n)) + \mu(\rho^h(t_{n+1}))\right)\right)_\Omega - \left(q_5^h, \frac{[\![\rho^h(t_n)]\!]^2}{12}\mu''(\rho^h(t_n))\right)_\Omega$$

$$+ \left(q_5^h, \nabla\frac{2|\mathbf{u}^h(t_{n+\frac{1}{2}})|^2 - \frac{1}{2}(|\mathbf{u}^h(t_n)|^2 + |\mathbf{u}^h(t_{n+1})|^2)}{2}\right)_\Omega - \left(\nabla q_5^h, \frac{1}{\mathbb{We}}\nabla\rho^h(t_{n+\alpha})\right)_\Omega = 0. \tag{131}$$

Assuming sufficient smoothness in time, Taylor series can be utilized to prove

$$\frac{1}{2}\left(\mu(\rho^h(t_n)) + \mu(\rho^h(t_{n+1}))\right) = \mu(\rho^h(t_{n+\frac{1}{2}})) + \mathcal{O}(\Delta t_n^2), \tag{132}$$

$$\frac{[\![\rho^h(t_n)]\!]^2}{12}\mu''(\rho^h(t_n)) = \mathcal{O}(\Delta t_n^2), \tag{133}$$

$$2|\mathbf{u}^h(t_{n+\frac{1}{2}})|^2 - \frac{1}{2}(|\mathbf{u}^h(t_n)|^2 + |\mathbf{u}^h(t_{n+1})|^2) = |\mathbf{u}^h(t_{n+\frac{1}{2}})|^2 + \mathcal{O}(\Delta t_n^2), \tag{134}$$

$$\rho^h(t_{n+\alpha}) = \rho^h(t_{n+\frac{1}{2}}) + \mathcal{O}(\eta\Delta t). \tag{135}$$

Considering that

$$\eta = \frac{1}{2}\tanh\left(\frac{\Delta t\mathbb{We}^{\frac{1}{2}}}{\mathcal{C}}\right) \leq \frac{\Delta t\mathbb{We}^{\frac{1}{2}}}{2\mathcal{C}}, \tag{136}$$

we conclude that

$$\rho^h(t_{n+\alpha}) = \rho^h(t_{n+\frac{1}{2}}) + \mathcal{O}(\Delta t_n^2). \tag{137}$$

Combining above results, it follows that

$$\left(q_1^h, \varpi_\rho\right)_\Omega = \left(q_1^h, \varpi_\rho^{mid}\right)_\Omega + \mathcal{O}(\Delta t_n^2), \tag{138}$$

$$\left(\mathbf{q}^h, \varpi_\mathbf{u}\right)_\Omega = \left(\mathbf{q}^h, \varpi_\mathbf{u}^{mid}\right)_\Omega + \mathcal{O}(\Delta t_n^2)\mathbf{1}. \tag{139}$$

Therefore, we have

$$\left(q_1^h, \varpi_\rho\right)_\Omega = \mathcal{O}(\Delta t_n^2), \tag{140}$$

$$\left(\mathbf{q}^h, \varpi_\mathbf{u}\right)_\Omega = \mathcal{O}(\Delta t_n^2) \tag{141}$$

which completes the proof. $\qquad\square$

28

Remark 14. *According to the relations (138) and (139), we may view our scheme as a second-order perturbation of the mid-point rule which achieves nonlinear stability.*

Remark 15. *From the relation (121), we see the energy dissipation associated with the time integration scheme actually consists of two parts: physical dissipation and numerical dissipation. The numerical dissipation will vanish if the time step approaches zero. When the time step is large, the numerical dissipation terms will enhance the stability of the scheme. Such a property makes our scheme very robust.*

Remark 16. *If we temporarily denote $\widehat{\Delta t_n}$ and $\overline{\Delta t_n}$ as dimensionless time step scaled with capillarity time scale $\sqrt{\lambda/(a^2 b)}$ and dimensional time step, respectively, then the meaning of the term $\Delta t_n \mathbb{We}^{\frac{1}{2}}/\mathcal{C}$ in (104) is revealed in the following relations by recalling (42) in Section 2.2:*

$$\frac{\Delta t_n \mathbb{We}^{\frac{1}{2}}}{\mathcal{C}} = \frac{\widehat{\Delta t_n}}{\mathcal{C}} = \frac{\overline{\Delta t_n}}{\mathcal{C}\sqrt{\frac{\lambda}{a^2 b}}}. \tag{142}$$

Thus, in terms of the dimensional time step $\overline{\Delta t_n}$, we see that the dimensionless expression $\Delta t_n \mathbb{We}^{\frac{1}{2}}/\mathcal{C}$ in fact does not depend on arbitrary scaling introduced by the non-dimensionalization. This relation also indicates that the numerical dissipation introduced by the last term in (100) is actually dictated by $\widehat{\Delta t_n}$, which is analogous to the design of numerical dissipation in [31].

Remark 17. *From (136), we observe that the dimensionless parameter $\mathcal{C}$ can be used to adjust the accuracy and robustness of our method. A larger value of $\mathcal{C}$ renders a more accurate scheme, while a smaller value of $\mathcal{C}$ renders a more stable method. Unless otherwise specified, the dimensionless parameter $\mathcal{C}$ is fixed to be 100.0 in all of our numerical examples.*

Remark 18. *It may be noted that the stability proof is valid for all $\eta \geq 0$. If $\eta = 0$, the last term in (121) does not produce numerical dissipation [33]. Positive η provides controllable numerical dissipation through the value of $\mathcal{C}$ selected.*

3.4 Numerical implementation

Let $\mathbf{C}_n^\rho = \{C_{n,A}^\rho\}_{A=1}^{n_b}$, $\mathbf{C}_n^{\mathbf{u}} = \{\mathbf{C}_n^{u_i}\}_{i=1}^3$, $\mathbf{C}_n^{u_i} = \{C_{n,A}^{u_i}\}_{A=1}^{n_b}$, and $\mathbf{C}_n^v = \{C_{n,A}^v\}_{A=1}^{n_b}$ denote the vectors of control variables (discrete solution coefficients) for ρ, $\mathbf{u}$, and v at time step t_n, where A is the control variable index and n_b is the dimension of the discrete space $\mathcal{V}^h$. If $\{N_A\}_{A=1}^{n_b}$ are the basis functions that span the discrete space $\mathcal{V}^h$, we have

$$\rho_n^h = \sum_{A=1}^{n_b} C_{n,A}^\rho N_A, \tag{143}$$

$$\mathbf{u}_n^h = (u_{1,n}^h, u_{2,n}^h, u_{3,n}^h)^T, \tag{144}$$

$$u_{i,n}^h = \sum_{A=1}^{n_b} C_{n,A}^{u_i} N_A, \tag{145}$$

$$v_n^h = \sum_{A=1}^{n_b} C_{n,A}^v N_A. \tag{146}$$

With the above notation defined, our fully discrete scheme may be implemented as follows: given $\mathbf{C}_n^\rho$, $\mathbf{C}_n^\mathbf{u}$, and $\mathbf{C}_n^v$, find $\mathbf{C}_{n+1}^\rho$, $\mathbf{C}_{n+1}^\mathbf{u}$, $\mathbf{C}_{n+1}^v$, such that

$$\mathbf{Q}^M \left(\mathbf{C}_{n+1}^\rho, \mathbf{C}_{n+1}^\mathbf{u}, \mathbf{C}_{n+1}^v \right) = 0, \tag{147}$$

$$\mathbf{Q}^\mathbf{U} \left(\mathbf{C}_{n+1}^\rho, \mathbf{C}_{n+1}^\mathbf{u}, \mathbf{C}_{n+1}^v \right) = \mathbf{0}, \tag{148}$$

$$\mathbf{Q}^E \left(\mathbf{C}_{n+1}^\rho, \mathbf{C}_{n+1}^\mathbf{u}, \mathbf{C}_{n+1}^v \right) = 0. \tag{149}$$

The above residual vectors are defined in the following sense:

$$\mathbf{Q}^M \left(\mathbf{C}_{n+1}^\rho, \mathbf{C}_{n+1}^\mathbf{u}, \mathbf{C}_{n+1}^v \right) := \{ Q_A^M \left(\mathbf{C}_{n+1}^\rho, \mathbf{C}_{n+1}^\mathbf{u}, \mathbf{C}_{n+1}^v \right) \}_{A=1}^{n_b}, \tag{150}$$

$$Q_A^M \left(\mathbf{C}_{n+1}^\rho, \mathbf{C}_{n+1}^\mathbf{u}, \mathbf{C}_{n+1}^v \right) := \mathbf{B}^M (N_A; \rho_{n+1}^h, \mathbf{u}_{n+1}^h, v_{n+1}^h), \tag{151}$$

$$\mathbf{Q}^\mathbf{U} \left(\mathbf{C}_{n+1}^\rho, \mathbf{C}_{n+1}^\mathbf{u}, \mathbf{C}_{n+1}^v \right) := \{ \mathbf{Q}^{\mathbf{U}_i} \left(\mathbf{C}_{n+1}^\rho, \mathbf{C}_{n+1}^\mathbf{u}, \mathbf{C}_{n+1}^v \right) \}_{i=1}^3, \tag{152}$$

$$\mathbf{Q}^{\mathbf{U}_i} \left(\mathbf{C}_{n+1}^\rho, \mathbf{C}_{n+1}^\mathbf{u}, \mathbf{C}_{n+1}^v \right) := \{ Q_A^{\mathbf{U}_i} \left(\mathbf{C}_{n+1}^\rho, \mathbf{C}_{n+1}^\mathbf{u}, \mathbf{C}_{n+1}^v \right) \}_{A=1}^{n_b}, \tag{153}$$

$$Q_A^{\mathbf{U}_i} \left(\mathbf{C}_{n+1}^\rho, \mathbf{C}_{n+1}^\mathbf{u}, \mathbf{C}_{n+1}^v \right) := \mathbf{B}^\mathbf{U} (N_A \mathbf{e}_i; \rho_{n+1}^h, \mathbf{u}_{n+1}^h, v_{n+1}^h), \tag{154}$$

$$\mathbf{Q}^E \left(\mathbf{C}_{n+1}^\rho, \mathbf{C}_{n+1}^\mathbf{u}, \mathbf{C}_{n+1}^v \right) := \{ Q_A^E \left(\mathbf{C}_{n+1}^\rho, \mathbf{C}_{n+1}^\mathbf{u}, \mathbf{C}_{n+1}^v \right) \}_{A=1}^{n_b}, \tag{155}$$

$$Q_A^E \left(\mathbf{C}_{n+1}^\rho, \mathbf{C}_{n+1}^\mathbf{u}, \mathbf{C}_{n+1}^v \right) := \mathbf{B}^E (N_A; \rho_{n+1}^h, \mathbf{u}_{n+1}^h, v_{n+1}^h). \tag{156}$$

Equations (147)-(149) constitute a nonlinear system of algebraic equations that needs to be solved at each time step. We solve the nonlinear system of equations by using the Newton-Raphson method [51]. Specifically, the control variables $\{ \mathbf{C}_{n+1}^\rho, \mathbf{C}_{n+1}^\mathbf{u}, \mathbf{C}_{n+1}^v \}$ at each time step t_{n+1}, with $n = 0, \cdots, N_{ts} - 1$, are obtained iteratively by means of the following two-stage predictor-multicorrector algorithm.

Predictor stage: Set

$$\mathbf{C}_{n+1,(0)}^\rho = \mathbf{C}_n^\rho, \tag{157}$$

$$\mathbf{C}_{n+1,(0)}^\mathbf{u} = \mathbf{C}_n^\mathbf{u}, \tag{158}$$

$$\mathbf{C}_{n+1,(0)}^v = \mathbf{C}_n^v. \tag{159}$$

Multicorrector stage: Repeat the following steps for $j = 1, \cdots, j_{max}$:

1. Evaluate the control variables for density at the intermediate stage:

$$\mathbf{C}_{n+\alpha}^\rho = \mathbf{C}_n^\rho + \alpha \left(\mathbf{C}_{n+1,(j-1)}^\rho - \mathbf{C}_n^\rho \right) \tag{160}$$

2. Assemble the residual vector of the nonlinear system using the $j-1$ stage solution and the above intermediate stage solution:

$$\mathbf{Q}_{(j)}^M := \mathbf{Q}^M (\mathbf{C}_{n+1,(j-1)}^\rho, \mathbf{C}_{n+1,(j-1)}^\mathbf{u}, \mathbf{C}_{n+1,(j-1)}^v), \tag{161}$$

$$\mathbf{Q}_{(j)}^\mathbf{U} := \mathbf{Q}^\mathbf{U} (\mathbf{C}_{n+1,(j-1)}^\rho, \mathbf{C}_{n+1,(j-1)}^\mathbf{u}, \mathbf{C}_{n+1,(j-1)}^v), \tag{162}$$

$$\mathbf{Q}_{(j)}^E := \mathbf{Q}^E (\mathbf{C}_{n+1,(j-1)}^\rho, \mathbf{C}_{n+1,(j-1)}^\mathbf{u}, \mathbf{C}_{n+1,(j-1)}^v). \tag{163}$$

3. Let $\| \left(\mathbf{Q}_{(j)}^M; \mathbf{Q}_{(j)}^{\mathbf{U}}; \mathbf{Q}_{(j)}^E \right) \|_{l^2}$ denote the l^2 norm of the $5n_b \times 1$ vector $\left(\mathbf{Q}_{(j)}^M; \mathbf{Q}_{(j)}^{\mathbf{U}}; \mathbf{Q}_{(j)}^E \right)$. If either one of the following criteria

$$\frac{\| \left(\mathbf{Q}_{(j)}^M; \mathbf{Q}_{(j)}^{\mathbf{U}}; \mathbf{Q}_{(j)}^E \right) \|_{l^2}}{\| \left(\mathbf{Q}_{(0)}^M; Q_{(0)}^{\mathbf{U}}; Q_{(0)}^E \right) \|_{l^2}} \le tol_R, \tag{164}$$

$$\| \left(\mathbf{Q}_{(j)}^M; \mathbf{Q}_{(j)}^{\mathbf{U}}; \mathbf{Q}_{(j)}^E \right) \|_{l^2} \le tol_A \tag{165}$$

is satisfied for a prescribed tolerance tol_R, tol_A, set the control variables at time t_{n+1} as $\mathbf{C}_{n+1}^\rho = \mathbf{C}_{n+1,(j-1)}^\rho$, $\mathbf{C}_{n+1}^{\mathbf{u}} = \mathbf{C}_{n+1,(j-1)}^{\mathbf{u}}$, $\mathbf{C}_{n+1}^v = \mathbf{C}_{n+1,(j-1)}^v$, and exit the multicorrector stage; otherwise, continue to step 4. We remind the reader that the notations (164) and (165) are non-dimensional.

4. Assemble the tangent matrix of the nonlinear system and solve the linear system of equations:

$$K_{11,(j)} = \frac{\partial \mathbf{Q}^M(\mathbf{C}_{n+1,(j-1)}^\rho, \mathbf{C}_{n+1,(j-1)}^{\mathbf{u}}, \mathbf{C}_{n+1,(j-1)}^v)}{\partial \mathbf{C}_{n+1,(j-1)}^\rho}, \tag{166}$$

$$K_{12,(j)} = \frac{\partial \mathbf{Q}^M(\mathbf{C}_{n+1,(j-1)}^\rho, \mathbf{C}_{n+1,(j-1)}^{\mathbf{u}}, \mathbf{C}_{n+1,(j-1)}^v)}{\partial \mathbf{C}_{n+1,(j-1)}^{\mathbf{u}}}, \tag{167}$$

$$K_{13,(j)} = \frac{\partial \mathbf{Q}^M(\mathbf{C}_{n+1,(j-1)}^\rho, \mathbf{C}_{n+1,(j-1)}^{\mathbf{u}}, \mathbf{C}_{n+1,(j-1)}^v)}{\partial \mathbf{C}_{n+1,(j-1)}^v}, \tag{168}$$

$$K_{21,(j)} = \frac{\partial \mathbf{Q}^{\mathbf{U}}(\mathbf{C}_{n+1,(j-1)}^\rho, \mathbf{C}_{n+1,(j-1)}^{\mathbf{u}}, \mathbf{C}_{n+1,(j-1)}^v)}{\partial \mathbf{C}_{n+1,(j-1)}^\rho}, \tag{169}$$

$$K_{22,(j)} = \frac{\partial \mathbf{Q}^{\mathbf{U}}(\mathbf{C}_{n+1,(j-1)}^\rho, \mathbf{C}_{n+1,(j-1)}^{\mathbf{u}}, \mathbf{C}_{n+1,(j-1)}^v)}{\partial \mathbf{C}_{n+1,(j-1)}^{\mathbf{u}}}, \tag{170}$$

$$K_{23,(j)} = \frac{\partial \mathbf{Q}^{\mathbf{U}}(\mathbf{C}_{n+1,(j-1)}^\rho, \mathbf{C}_{n+1,(j-1)}^{\mathbf{u}}, \mathbf{C}_{n+1,(j-1)}^v)}{\partial \mathbf{C}_{n+1,(j-1)}^v}, \tag{171}$$

$$K_{31,(j)} = \frac{\partial \mathbf{Q}^E(\mathbf{C}_{n+1,(j-1)}^\rho, \mathbf{C}_{n+1,(j-1)}^{\mathbf{u}}, \mathbf{C}_{n+1,(j-1)}^v)}{\partial \mathbf{C}_{n+1,(j-1)}^\rho}, \tag{172}$$

$$K_{32,(j)} = \frac{\partial \mathbf{Q}^E(\mathbf{C}_{n+1,(j-1)}^\rho, \mathbf{C}_{n+1,(j-1)}^{\mathbf{u}}, \mathbf{C}_{n+1,(j-1)}^v)}{\partial \mathbf{C}_{n+1,(j-1)}^{\mathbf{u}}}, \tag{173}$$

$$K_{33,(j)} = \frac{\partial \mathbf{Q}^E(\mathbf{C}_{n+1,(j-1)}^\rho, \mathbf{C}_{n+1,(j-1)}^{\mathbf{u}}, \mathbf{C}_{n+1,(j-1)}^v)}{\partial \mathbf{C}_{n+1,(j-1)}^v}, \tag{174}$$

$$\begin{pmatrix} K_{11,(j)} & K_{12,(j)} & K_{13,(j)} \\ K_{21,(j)} & K_{22,(j)} & K_{23,(j)} \\ K_{31,(j)} & K_{32,(j)} & K_{33,(j)} \end{pmatrix} \begin{pmatrix} \Delta C_{n+1,(j)}^\rho \\ \Delta C_{n+1,(j)}^{\mathbf{u}} \\ \Delta C_{n+1,(j)}^v \end{pmatrix} = - \begin{pmatrix} \mathbf{Q}_{(j)}^M \\ \mathbf{Q}_{(j)}^{\mathbf{U}} \\ \mathbf{Q}_{(j)}^E \end{pmatrix}. \tag{175}$$

5. Use the solutions to update the iterates as:

$$\mathbf{C}_{n+1,(j)}^{\rho} = \mathbf{C}_{n+1,(j-1)}^{\rho} + \Delta C_{n+1,(j)}^{\rho}, \tag{176}$$

$$\mathbf{C}_{n+1,(j)}^{\mathbf{u}} = \mathbf{C}_{n+1,(j-1)}^{\mathbf{u}} + \Delta C_{n+1,(j)}^{\mathbf{u}}, \tag{177}$$

$$\mathbf{C}_{n+1,(j)}^{v} = \mathbf{C}_{n+1,(j-1)}^{v} + \Delta C_{n+1,(j)}^{v} \tag{178}$$

and return to step 1.

Remark 19. *The control variables $\mathbf{C}_0^{\rho}$ and $\mathbf{C}_0^{\mathbf{u}}$ are straightforwardly obtained from the initial condition. We obtain the control variables $\mathbf{C}_0^v$ by solving*

$$\left(q_5^h, v_0^h\right)_{\Omega} = \left(q_5^h, \mu\left(\rho_0^h\right) - \frac{1}{2}|\mathbf{u}_0^h|^2\right)_{\Omega} + \left(\nabla q_5^h, \frac{1}{\mathbb{We}}\nabla \rho_0^h\right)_{\Omega} \tag{179}$$

This is a simple calculation because (179) *is linear in v_0^h and the coefficient matrix is the Gram matrix determined by the basis functions. The solution at step $n = 0$ does not depend on C_0^v, however its value is necessary to initiate the predictor-corrector algorithm given by* (157)-(178).

Remark 20. *We adopt the preconditioned GMRES algorithm [53] from PETSc [2] to solve the linear system given by* (175). *In our experience, the additive Schwarz method performs better than incomplete-LU factorization as a parallel preconditioner.*

Remark 21. *We use the consistent tangent matrix in all of our computations. For the verification problems in Section 4, we set $tol_R = 10^{-9}$ and $tol_A = 10^{-11}$. For the application simulations in Section 5, we set $tol_R = 10^{-3}$ and $tol_A = 10^{-6}$.*

3.5   Interface width and refinement methodology

In a numerical simulation of a phase-field problem, it is required that the computational mesh be sufficiently fine in order to resolve the diffuse interface. Otherwise, unphysical oscillations may appear and pollute the numerical solution. In [22], it was shown that, at a fixed temperature, the diffuse interface length scale for the isothermal Navier-Stokes-Korteweg system is proportional to $L_0 \mathbb{We}^{-\frac{1}{2}}$. Based on this scaling argument, we propose a criterion for choosing a proper simulation mesh size h. Assuming σ is a non-dimensional positive constant and h is the non-dimensional characteristic length scale of the spatial mesh, we require that h satisfy the following inequality:

$$h \leq \frac{\sigma}{\sqrt{\mathbb{We}}}. \tag{180}$$

For a given Weber number, this inequality indicates an upper bound for the size of a computational mesh. For realistic problems where the interface width is often on the order of a few nanometers, this inequality provides an estimate for local mesh sizes in the context of adaptive refinement [54, 56]. In Section 5.1.1, we demonstrate through numerical experimentation the importance of satisfying the mesh size criterion (180). In all other numerical experiments in Section 4 and 5, we only employ computational meshes which satisfy (180).

Finally, before proceeding, in order to obtain physically correct solutions in the vanishing viscosity and capillarity limit, the following relationship

$$\mathbb{R}\mathrm{e} = \beta \mathbb{W}\mathrm{e}^{\frac{1}{2}}, \tag{181}$$

where β is a non-dimensional constant, must be satisfied [61, 47]. With the aim of capturing the correct sharp interface limit solution, we will adopt such a relation in all of our later numerical simulations.

Remark 22. *Similar scaling arguments to those discussed above have been successfully applied to the numerical studies of phase-field models in [30, 31, 32]. Following the parameter choices made in [32], we take $\sigma = 1.0$ and $\beta = 2.0$ in all of our simulations. All of the meshes used in our calculations give rise to a characteristic spatial mesh length-scale defined as*

$$h = \frac{1}{2} \max_i V_i^{\frac{1}{d}}, \tag{182}$$

where d is the number of spatial dimensions and V_i is the volume/area of the i-th element such that (180) is satisfied, except for the example in Section 5.1.1 where we explore the consequences of violating (180). In the context of NURBS-based isogeometric analysis, an element is defined as a Bézier element [11], that is the volume/area between knots.

4   Numerical Examples

In this section, we present a selection of numerical examples to test the stability, accuracy, and mass conservation properties of our numerical formulation.

4.1   Manufactured solution for code verification

For our first numerical example, we construct a one dimensional manufactured solution to verify our code as well as the time accuracy of the time integration scheme given by (98)-(100). In particular, we consider the manufactured solution

$$\rho = 0.6 + 0.1 \sin(5\pi t) \cos(3\pi x), \tag{183}$$
$$\mathbf{u} = \sin(3\pi t) \sin(2\pi x). \tag{184}$$

Restricting our computations to the domain $\Omega = (0, 1)$, we observe that the manufactured solution satisfies the boundary conditions given by (4) and (3). The force vector $\mathbf{f}$ is obtained by substituting the above manufactured solution into equations (32)-(33). The dimensionless parameters are fixed to be $\mathbb{R}\mathrm{e} = 2.0 \times 10^1$ and $\mathbb{W}\mathrm{e} = 1.0 \times 10^2$. First, we compute the problem with mesh size $\Delta x = 1/16, 1/32, 1/64, 1/128$ and $1/256$ for a fixed time step size of $\Delta t = 1.0 \times 10^{-5}$ for polynomial degrees $k' = 1, 2$, and 3. The L^2-errors of ρ and $\mathbf{u}$, together with the corresponding convergence rates of the errors at $t = 0.1$, are listed in Tables 1-3. Notice that the L^2-norm of the density and velocity errors optimally converges like $\mathcal{O}(\Delta x^{(k'+1)})$. These are optimal convergence rates in L^2. We want to mention that the deteriorated convergence

rates for $k' = 3$ at $\Delta x = 1/256$ are expected since the numerical errors are driven close to machine precision at these spatial resolutions. Next, to analyze the behavior of the temporal discretization, we fix the spatial mesh to consist of 10^4 linear, quadratic, and cubic elements and calculate the discrete solution up to $t = 1.0$ with $20, 100, 200, 1000$, and 2000 time steps. The solution errors at $t = 1.0$ versus the number of time steps are listed in Tables 4-6. We see that the numerical scheme exhibits second-order accuracy in time for all three polynomial degrees.

Table 1: Spatial convergence rate at $t = 0.1$ with polynomial degree $k' = 1$.

Δx	1/16	1/32	1/64	1/128	1/256
$\|\rho - \rho^h\|_{L^2(\Omega)}$	9.94×10^{-4}	2.41×10^{-4}	5.97×10^{-5}	1.49×10^{-5}	3.72×10^{-6}
order	-	2.04	2.01	2.00	2.00
$\|\mathbf{u} - \mathbf{u}^h\|_{L^2(\Omega)}$	3.74×10^{-3}	9.26×10^{-4}	2.31×10^{-4}	5.77×10^{-5}	1.44×10^{-5}
order	-	2.01	2.00	2.00	2.00

Table 2: Spatial convergence rate at $t = 0.1$ with polynomial degree $k' = 2$.

Δx	1/16	1/32	1/64	1/128	1/256
$\|\rho - \rho^h\|_{L^2(\Omega)}$	1.00×10^{-4}	1.19×10^{-5}	1.46×10^{-6}	1.82×10^{-7}	2.28×10^{-8}
order	-	3.07	3.03	3.00	3.00
$\|\mathbf{u} - \mathbf{u}^h\|_{L^2(\Omega)}$	2.36×10^{-4}	2.82×10^{-5}	3.47×10^{-6}	4.31×10^{-7}	5.37×10^{-8}
order	-	3.07	3.02	3.01	3.00

Table 3: Spatial convergence rate at $t = 0.1$ with polynomial degree $k' = 3$.

Δx	1/16	1/32	1/64	1/128	1/256
$\|\rho - \rho^h\|_{L^2(\Omega)}$	8.75×10^{-6}	4.94×10^{-7}	3.02×10^{-8}	1.92×10^{-9}	3.94×10^{-10}
order	-	4.15	4.03	3.98	2.28
$\|\mathbf{u} - \mathbf{u}^h\|_{L^2(\Omega)}$	1.38×10^{-5}	7.94×10^{-7}	4.87×10^{-8}	3.31×10^{-9}	1.35×10^{-9}
order	-	4.12	4.03	3.88	1.29

4.2 Coalescence of two bubbles in the absence of gravity

In this example, we consider a problem with zero body force (i.e., $\mathbf{f} = \mathbf{0}$) for the purpose of examining the mass conservation and energy dissipation properties of our scheme. Specifically, we consider a vapor bubble dynamics problem that was originally studied in [32, 41]. In this example, two vapor bubbles of different radii are originally placed close to each other.

Table 4: Temporal convergence rate at $t = 1.0$ with $\Delta x = 1.0 \times 10^{-4}$, polynomial degree k' = 1.

Δt	5.0×10^{-2}	1.0×10^{-2}	5.0×10^{-3}	1.0×10^{-3}	5.0×10^{-4}
$\|\rho - \rho^h\|_{L^2(\Omega)}$	7.35×10^{-3}	2.77×10^{-4}	6.90×10^{-5}	2.76×10^{-6}	6.93×10^{-7}
order	-	2.04	2.00	2.00	1.99
$\|\mathbf{u} - \mathbf{u}^h\|_{L^2(\Omega)}$	1.74×10^{-2}	6.75×10^{-4}	1.68×10^{-4}	6.72×10^{-6}	1.67×10^{-6}
order	-	2.02	2.01	2.00	2.01

Table 5: Temporal convergence rate at $t = 1.0$ with $\Delta x = 1.0 \times 10^{-4}$, polynomial degree k' = 2.

Δt	5.0×10^{-2}	1.0×10^{-2}	5.0×10^{-3}	1.0×10^{-3}	5.0×10^{-4}
$\|\rho - \rho^h\|_{L^2(\Omega)}$	7.35×10^{-3}	2.77×10^{-4}	6.90×10^{-5}	2.76×10^{-6}	6.90×10^{-7}
order	-	2.04	2.00	2.00	2.00
$\|\mathbf{u} - \mathbf{u}^h\|_{L^2(\Omega)}$	1.74×10^{-2}	6.75×10^{-4}	1.68×10^{-4}	6.73×10^{-6}	1.68×10^{-6}
order	-	2.02	2.00	2.00	2.00

Table 6: Temporal convergence rate at $t = 1.0$ with $\Delta x = 1.0 \times 10^{-4}$, polynomial degree k' = 3.

Δt	5.0×10^{-2}	1.0×10^{-2}	5.0×10^{-3}	1.0×10^{-3}	5.0×10^{-4}
$\|\rho - \rho^h\|_{L^2(\Omega)}$	7.35×10^{-3}	2.77×10^{-4}	6.90×10^{-5}	2.76×10^{-6}	6.90×10^{-7}
order	-	2.04	2.00	2.00	2.00
$\|\mathbf{u} - \mathbf{u}^h\|_{L^2(\Omega)}$	1.74×10^{-2}	6.75×10^{-4}	1.68×10^{-4}	6.73×10^{-6}	1.68×10^{-6}
order	-	2.02	2.00	2.00	2.00

Capillarity and pressure forces then drive the two bubbles to merge together and form a single vapor bubble in equilibrium.

For this example, the computational domain is set to be $\Omega = (0,1)^2$. We use 256^2 quadratic NURBS functions to discretize in space. The centers of the bubbles are originally located at points $C_1 = (0.40, 0.50)$ and $C_2 = (0.78, 0.50)$. The radii of the bubbles are set to be $R_1 = 0.25$ and $R_2 = 0.10$. We specify the diffuse interface between the vapor and liquid phases via a hyperbolic tangent regularization [32]:

$$\rho_0(\mathbf{x}) = 0.10 + 0.25 \left[\tanh\left(\frac{d_1(\mathbf{x}) - R_1}{2}\sqrt{\mathbb{We}} \right) + \tanh\left(\frac{d_2(\mathbf{x}) - R_2}{2}\sqrt{\mathbb{We}} \right) \right], \qquad (185)$$

where $d_i(\mathbf{x})$ is the Euclidean distance between $\mathbf{x}$ and C_i, $i = 1, 2$. The initial velocities are set to be zero, i.e. $\mathbf{u} = \mathbf{0}$, and we simulate the coalescence process up to a final time of $t = 5.0$. In our simulation, the dimensionless parameters are fixed to be $\mathbb{Re} = 5.12 \times 10^2$ and $\mathbb{We} = 6.55 \times 10^4$, which satisfy (180) and (181). To verify the time accuracy of our scheme, we have employed an overkill solution with which to compare our numerical solution.

4.2.1 Mass conservation

Let us denote the discrete mass at the final time step $t_n = 5.0$ as

$$m_n = \int_\Omega \rho_n^h d\mathbf{x}, \qquad (186)$$

and the initial mass as

$$m_0 = \int_\Omega \rho_0^h d\mathbf{x} = \int_\Omega \rho_0(\mathbf{x}) d\mathbf{x}. \qquad (187)$$

We have computed the coalescence problem with time step sizes of $\Delta t = 2.50 \times 10^{-2}, 1.25 \times 10^{-2}, 6.25 \times 10^{-3}, 5.0 \times 10^{-3}, 2.5 \times 10^{-3}$, and 1.25×10^{-3} and listed the corresponding maximum norms of relative mass error in Table 7. Note that the maximum mass errors are on the order of 10^{-12} which may be attributed to quadrature errors, the nonlinear solver tolerance and round-off errors. This corroborates the mass conservation of the numerical scheme (98)-(100).

Table 7: Mass error of the two-bubble coalescence problem.

Δt	2.50×10^{-2}	1.25×10^{-2}	6.25×10^{-3}	5.00×10^{-3}	2.50×10^{-3}	1.25×10^{-3}
$\left\|\frac{m_n - m_0}{m_0}\right\|_{l_\infty}$	1.95×10^{-12}	1.97×10^{-12}	1.89×10^{-12}	1.96×10^{-12}	2.02×10^{-12}	2.06×10^{-12}

4.2.2 Energy dissipation

To verify the energy dissipation property of our scheme, we have calculated the discrete energy associated with the numerical solution corresponding to time step sizes of $\Delta t =$

$2.50 \times 10^{-2}, 1.25 \times 10^{-2}, 6.25 \times 10^{-3}$, and 2.50×10^{-3}. We have also computed the discrete energy associated with an overkill solution corresponding to a time step size of $\Delta t = 2.5 \times 10^{-5}$. These discrete energies $\mathcal{E}(\rho_n^h, \mathbf{u}_n^h)$ are plotted against time in Figure 5. From the figure, we observe that the energy monotonically decreases with time for each time step size. Additionally, there is no visual difference between the different discrete energies. In Figure 6, we have plotted a detailed view of the discrete energy histories near $t = 0.1$. From this figure, we can see that the difference between the numerical solution and the overkill solution decreases with a reduction of time step size.
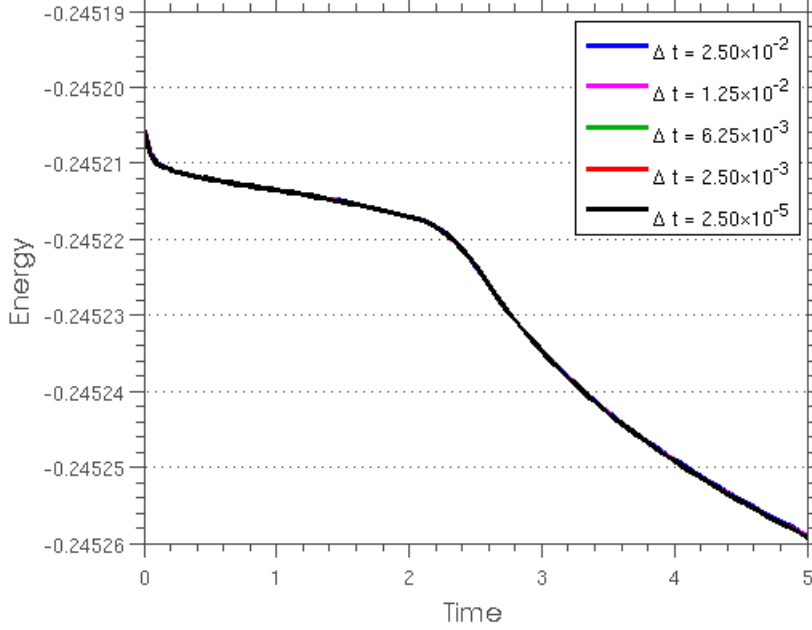
Figure 5: Coalescence of two bubbles: Evolution of the free energy calculated using provably stable algorithm with different time steps.

4.2.3 Time accuracy

We calculate overkill solutions with $\Delta t = 2.50 \times 10^{-5}$. Then we repeat the computation with larger time steps $\Delta t = 2.50 \times 10^{-2}, 1.25 \times 10^{-2}, 6.25 \times 10^{-3}, 2.50 \times 10^{-3}$, and 1.25×10^{-3}. The errors at $t = 1.0, 2.0, 3.0, 4.0$ and 5.0 are listed in Tables 8 - 12. In these five tables, we may observe that the time accuracy for both density and velocity are second-order, which confirms the theoretical estimate we gave previously. In figures 7-11, we depict the density profile and the velocity field at time $t = 1.0, 2.0, 3.0, 4.0$ and 5.0.

5 Applications

In this section, we simulate three different benchmark problems to investigate the effectiveness of our method as well as the validity of the Navier-Stokes-Korteweg model.
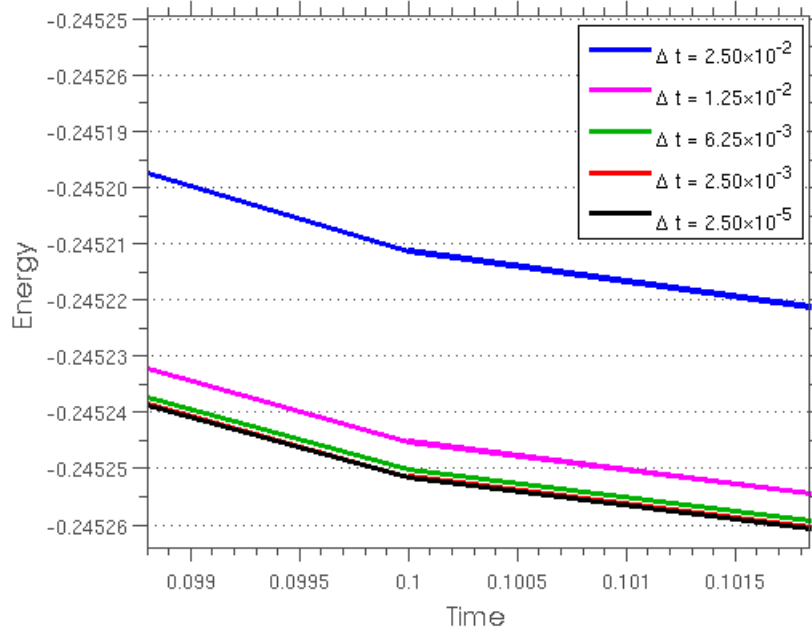
Figure 6: Coalescence of two bubbles: Evolution of the free energy calculated using provably stable algorithm with different time steps. Detailed view in the vicinity of $t = 0.1$.

Table 8: Convergence rate at $t = 1.0$.

Δt	2.50×10^{-2}	1.25×10^{-2}	6.25×10^{-3}	5.00×10^{-3}	2.50×10^{-3}	1.25×10^{-3}
$\|\rho - \rho^h\|_{L^2(\Omega)}$	1.81×10^{-4}	4.57×10^{-5}	1.14×10^{-5}	7.32×10^{-6}	1.83×10^{-6}	4.57×10^{-7}
order	-	1.99	2.00	1.99	2.00	2.00
$\|\mathbf{u} - \mathbf{u}^h\|_{L^2(\Omega)}$	3.56×10^{-5}	8.81×10^{-6}	2.20×10^{-6}	1.41×10^{-6}	3.52×10^{-7}	8.79×10^{-8}
order	-	2.02	2.00	2.00	2.00	2.00

Table 9: Convergence rate at $t = 2.0$.

Δt	2.50×10^{-2}	1.25×10^{-2}	6.25×10^{-3}	5.00×10^{-3}	2.50×10^{-3}	1.25×10^{-3}
$\|\rho - \rho^h\|_{L^2(\Omega)}$	5.75×10^{-4}	1.45×10^{-4}	3.65×10^{-5}	2.33×10^{-5}	5.83×10^{-6}	1.46×10^{-6}
order	-	1.99	1.99	2.01	2.00	2.00
$\|\mathbf{u} - \mathbf{u}^h\|_{L^2(\Omega)}$	4.79×10^{-5}	1.21×10^{-5}	3.04×10^{-6}	1.94×10^{-6}	4.86×10^{-7}	1.21×10^{-7}
order	-	1.98	2.00	2.00	2.00	2.00

Table 10: Convergence rate at $t = 3.0$.

Δt	2.50×10^{-2}	1.25×10^{-2}	6.25×10^{-3}	5.00×10^{-3}	2.50×10^{-3}	1.25×10^{-3}
$\|\rho - \rho^h\|_{L^2(\Omega)}$	8.21×10^{-4}	2.08×10^{-4}	5.21×10^{-5}	3.34×10^{-5}	8.34×10^{-6}	2.09×10^{-6}
order	-	1.98	2.00	1.99	2.00	2.00
$\|\mathbf{u} - \mathbf{u}^h\|_{L^2(\Omega)}$	5.20×10^{-5}	1.33×10^{-5}	3.33×10^{-6}	2.13×10^{-6}	5.33×10^{-7}	1.33×10^{-7}
order	-	1.97	1.99	2.00	2.00	2.00

Table 11: Convergence rate at $t = 4.0$.

Δt	2.50×10^{-2}	1.25×10^{-2}	6.25×10^{-3}	5.00×10^{-3}	2.50×10^{-3}	1.25×10^{-3}
$\|\rho - \rho^h\|_{L^2(\Omega)}$	9.00×10^{-4}	2.28×10^{-4}	5.70×10^{-5}	3.65×10^{-5}	9.12×10^{-6}	2.28×10^{-6}
order	-	1.98	2.00	2.00	2.00	2.00
$\|\mathbf{u} - \mathbf{u}^h\|_{L^2(\Omega)}$	3.54×10^{-5}	8.49×10^{-6}	2.24×10^{-6}	1.43×10^{-6}	3.58×10^{-7}	8.95×10^{-8}
order	-	2.06	1.92	2.00	2.00	2.00

Table 12: Convergence rate at $t = 5.0$.

Δt	2.50×10^{-2}	1.25×10^{-2}	6.25×10^{-3}	5.00×10^{-3}	2.50×10^{-3}	1.25×10^{-3}
$\|\rho - \rho^h\|_{L^2(\Omega)}$	1.10×10^{-3}	2.77×10^{-4}	6.92×10^{-5}	4.43×10^{-5}	1.11×10^{-5}	2.76×10^{-6}
order	-	1.99	2.00	2.00	2.00	2.00
$\|\mathbf{u} - \mathbf{u}^h\|_{L^2(\Omega)}$	3.56×10^{-5}	8.98×10^{-6}	2.25×10^{-6}	1.44×10^{-6}	3.59×10^{-7}	8.96×10^{-8}
order	-	1.99	2.00	2.00	2.00	2.00
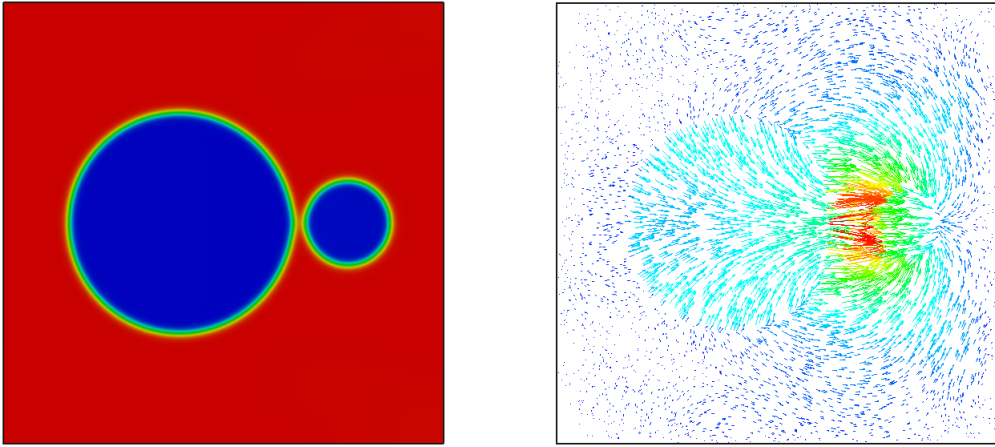
Figure 7: Solution at $t = 1.0$: (left) density distribution, (right) velocity field.
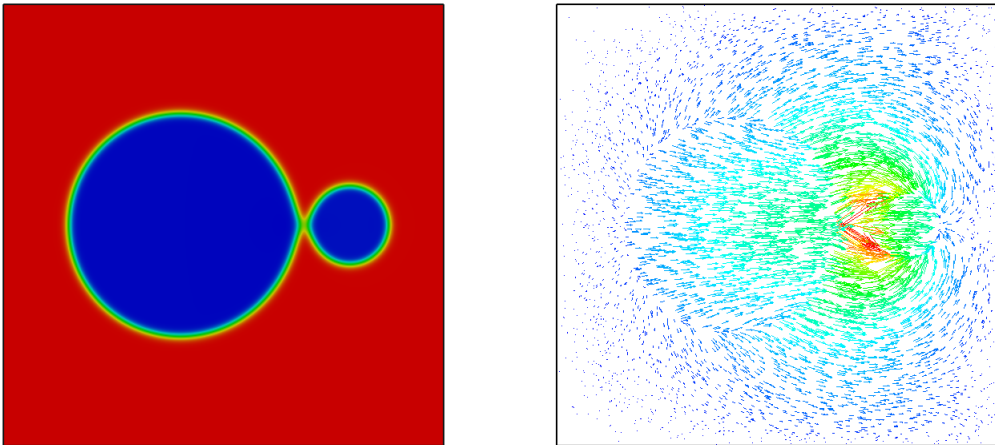
Figure 8: Solution at $t = 2.0$: (left) density distribution, (right) velocity field.
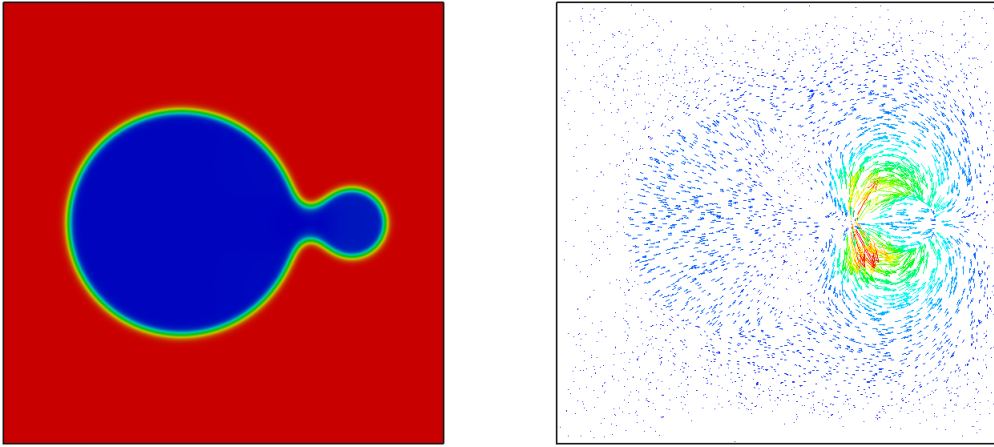
Figure 9: Solution at $t = 3.0$: (left) density distribution, (right) velocity field.
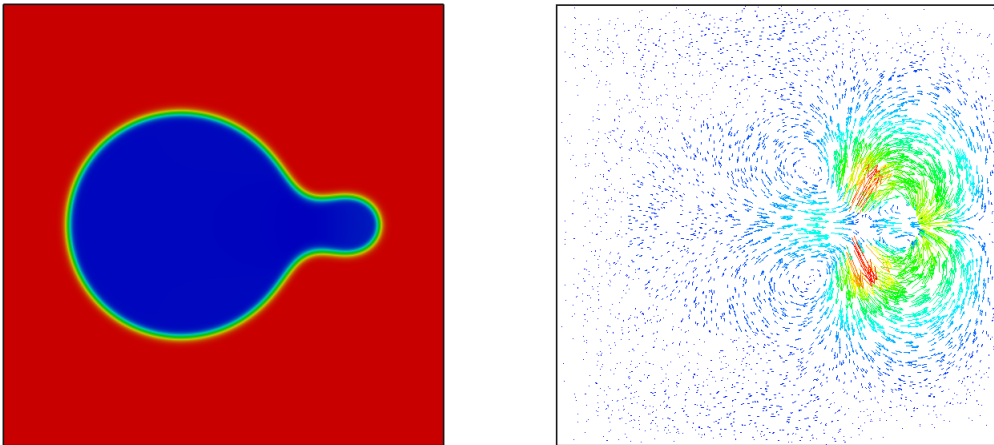
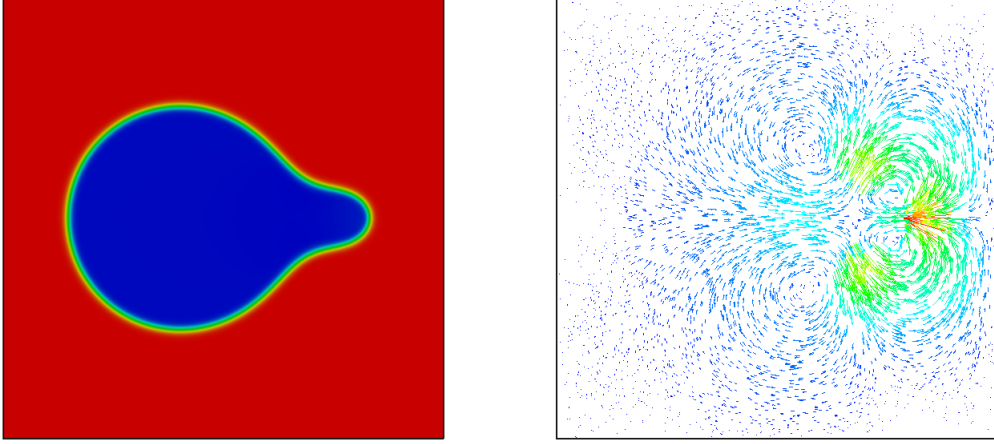Figure 10: Solution at $t = 4.0$: (left) density distribution, (right) velocity field.

Figure 11: Solution at $t = 5.0$: (left) density distribution, (right) velocity field.

5.1 Traveling wave problem

The traveling wave problem is one of the few benchmark problems that possesses a firm mathematical foundation [8]. It is frequently used to assess the accuracy and robustness of numerical schemes for conservation laws. As is well-known, poorly-designed numerical schemes will result in approximate solutions characterized by overshoots, undershoots, and incorrect propagation speeds of waves in the presence of sharp layers or discontinuities. Here, we consider traveling wave solutions to the one-dimensional Navier-Stokes-Korteweg equations. We restrict ourselves to the domain $(0, 1)$ and set the initial conditions as

$$\rho_0(x) = \frac{\rho^{right} + \rho^{left}}{2} + \frac{\rho^{right} - \rho^{left}}{2} \tanh\left(\frac{x - 0.5}{2}\sqrt{\mathbb{W}\text{e}}\right), \tag{188}$$

$$u_0(x) = \frac{u^{right} + u^{left}}{2} + \frac{u^{right} - u^{left}}{2} \tanh\left(\frac{x - 0.5}{2}\sqrt{\mathbb{W}\text{e}}\right). \tag{189}$$

Periodic boundary conditions are imposed on an extended region $(-1, 1)$.

5.1.1 Stationary wave problem

We begin by considering a stationary wave problem. By applying the initial conditions

$$(\rho^{right}, u^{right}) = (0.602, 0.0), \qquad (\rho^{left}, u^{left}) = (0.107, 0.0), \tag{190}$$

we obtain a stationary wave centered at $x = 0.5$ which sharpens as time evolves. This is due to the fact that the initial velocity field is zero and the initial density profile satisfies the Maxwell states (43)-(44) as well as the Rankine-Hugoniot conditions [26]. We choose the Reynolds number to be 2.0×10^2 and the Weber number to be 1.0×10^4. The problem is simulated using linear, quadratic, and cubic NURBS for $\Delta x = 1.0 \times 10^{-2}$ up to a final

42
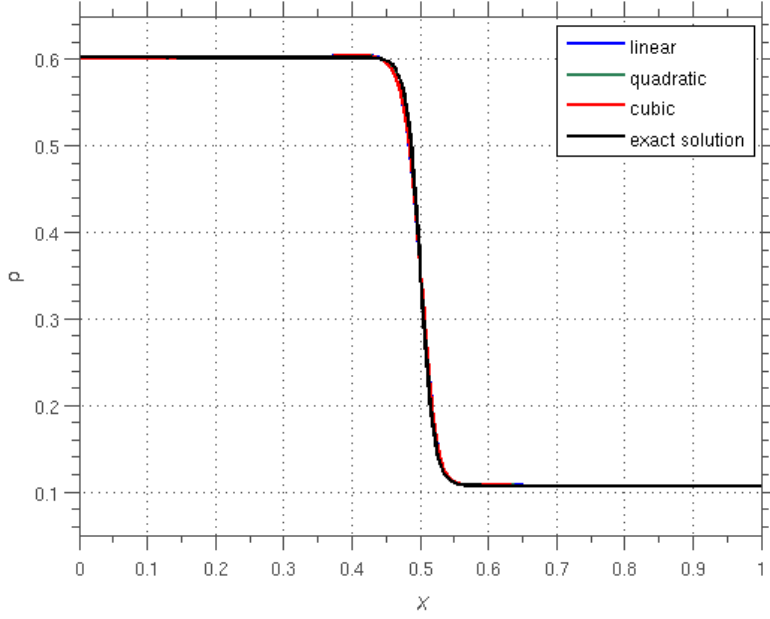
Figure 12: Solution of the stationary wave problem at $t = 0.1$ using linear, quadratic, and cubic NURBS for $\Delta x = 1.0 \times 10^{-2}$, $\Delta t = 1.0 \times 10^{-6}$, $\mathbb{Re} = 2.0 \times 10^2$, and $\mathbb{We} = 1.0 \times 10^4$.
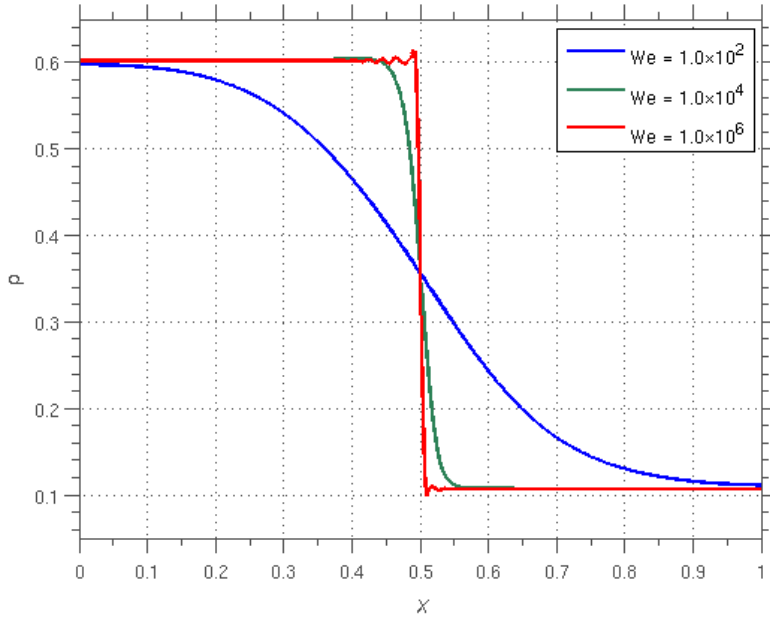
Figure 13: Solution of the stationary wave problem at $t = 0.1$ for Weber numbers 1.0×10^2, 1.0×10^4, and 1.0×10^6 when $\Delta x = 1.0 \times 10^{-2}$, $\Delta t = 1.0 \times 10^{-6}$, and $\mathbb{Re} = 2.0 \times 10^2$.
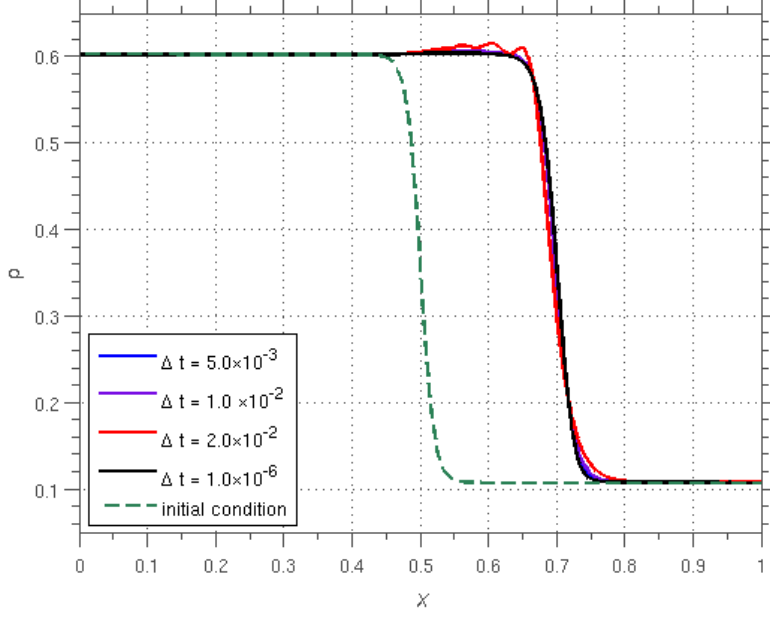
Figure 14: Solution of the propagating wave problem at $t = 0.2$ for time step sizes of $\Delta t = 5.0 \times 10^{-3}$, $\Delta t = 1.0 \times 10^{-2}$, $\Delta t = 2.0 \times 10^{-2}$, and $\Delta t = 1.0 \times 10^{-6}$ (reference solution) when $\Delta x = 1.0 \times 10^{-2}$, $\mathbb{R}e = 2.0 \times 10^2$, and $\mathbb{W}e = 1.0 \times 10^4$.

time of $t = 0.1$ using a time step size of $\Delta t = 1.0 \times 10^{-6}$. The resulting density profiles are illustrated in Figure 12. We can see from the figure that the differences between the numerical solutions and the exact solution are indistinguishable for all three polynomial degrees. Another important feature is that all three numerical solutions are smooth without oscillations.

We next compare the effect of capillarity on our approximation of the stationary wave problem. We use this example to illustrate the importance of the mesh choice criterion (180). We discretize in space using a quadratic NURBS basis and fix the spatial mesh size to be $\Delta x = 1.0 \times 10^{-2}$. The temporal integration is performed up to $t = 0.1$ with a step size of $\Delta t = 1.0 \times 10^{-6}$. The Reynolds number is fixed to be 2.0×10^2. In Figure 13, we have plotted the numerical solution for Weber numbers 1.0×10^2, 1.0×10^4, and 1.0×10^6 respectively. For $\mathbb{W}e = 1.0 \times 10^2$ and 1.0×10^4, the criterion given by (180) is satisfied and the obtained numerical solutions are smooth and without oscillations. We may also observe that the interface width for $\mathbb{W}e = 1.0 \times 10^2$ is of the order $\mathcal{O}(1)$, while that for $\mathbb{W}e = 1.0 \times 10^4$ is of the order $\mathcal{O}(0.1)$. These observations match well with the interface width estimate made in [22]. For $\mathbb{W}e = 1.0 \times 10^6$, the mesh size criterion (180) is upset. Spikes and oscillations are observed near a very sharp phase boundary, which is harmful for long time simulations. Indeed, this example indicates that the satisfaction of criterion (180) is necessary for providing non-oscillatory results.

5.1.2 Propagating wave problem

We next consider a propagating wave problem. To do so, we set the initial conditions to be

$$(\rho^{right}, u^{right}) = (0.602, 1.0), \qquad (\rho^{left}, u^{left}) = (0.107, 1.0). \tag{191}$$

In this setting, a propating traveling solution will form, moving in the positive x direction at speed 1.0. We fix the spatial discretization to consist of quadratic NURBS basis functions and we fix the spatial mesh size to be $\Delta x = 1.0 \times 10^{-2}$, and the dimensionless quantities are taken as $\mathbb{Re} = 2.0 \times 10^2$ and $\mathbb{We} = 1.0 \times 10^4$. We perform temporal integration up to $t = 0.2$ with time step sizes of $\Delta t = 5.0 \times 10^{-3}$, $\Delta t = 1.0 \times 10^{-2}$, and $\Delta t = 2.0 \times 10^{-2}$. Notice that the characteristic speeds of this problem are $u \pm \sqrt{dp/d\rho}$. The CFL number $\mathbb{C}$ is defined as

$$\mathbb{C} = \max_{\rho \in [0.602, 0.107]} \left\{ u \pm \sqrt{\frac{dp}{d\rho}} \right\} \frac{\Delta t}{\Delta x} = 162.1 \Delta t. \tag{192}$$

Thus, the corresponding CFL numbers are 0.81, 1.62, and 3.24. We observe that correct traveling waves are captured at all three CFL numbers. Oscillations are seen for $\mathbb{C} \geq 1$. For even larger time steps, there is the counterbalancing effect of even more numerical dissipation being introduced and the computed solution becomes more diffusive, as can be seen in Figure 14.

5.2 Bubble dynamics on an annular surface

As a second benchmark problem, we solve the Navier-Stokes-Korteweg equations on an annular surface to study vapor bubble dynamics on a curved geometry. There are several objectives of this study. First of all, we want to research the effects of the capillarity and the pressure force on bubble dynamics. According to thermodynamic considerations [29], inward-pointing pressure gradients exist at the surface of smaller bubbles due to capillarity effects. These pressure gradients cause smaller bubbles to disappear in favor of larger ones. Therefore, small bubbles are considered thermodynamically unstable. A closely related phenomenon is known as Ostwald's ripening [50]. Using the van der Waals model, we endeavor to obtain insight on such an important thermodynamic phenomenon. Our second objective is to show the geometrical and topological flexibility of isogeometric analysis. The annular surface is a common engineering geometry, yet it is hard to represent exactly within traditional numerical frameworks such as finite differences or finite elements. Specifically finite difference or finite element methods usually approximate annular geometries using polyhedral grids or elements, inevitably introducing approximation errors due to geometry. This geometric approximation error may introduce erroneous numerical mass sources, which in turn may deteriorate the conservation properties of a given numerical scheme. By employing NURBS-based isogeometric analysis, we are able to exactly represent the geometry of the annular surface. Such an exact representation will play a critical role in retaining the nonlinear stability and mass conservation properties of our fully discrete scheme.
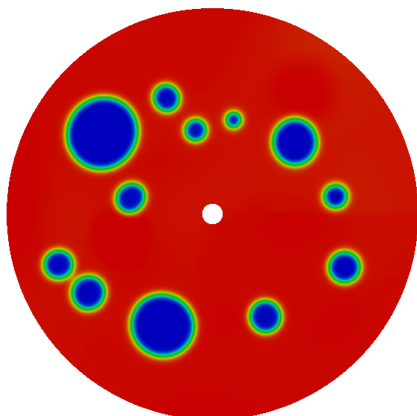
The interior radius of the annular surface is taken to be $r_{in} = 0.1$, while the exterior radius is taken as $r_{ex} = 2.0$. To parametrize the annular surface using NURBS, we employ the square-based NURBS construction of degree two outlined in [10, 18]. In the circumferential
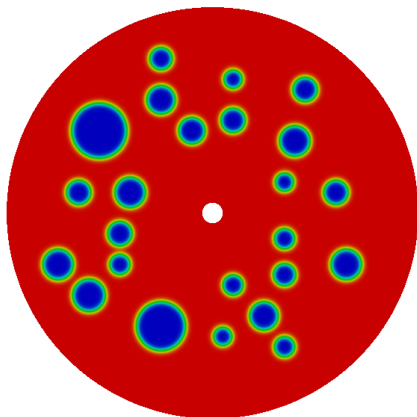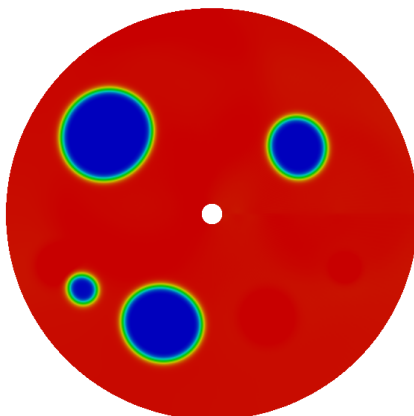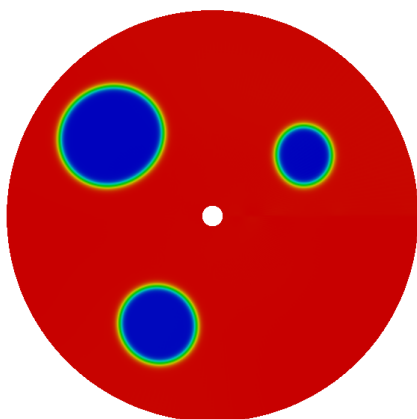
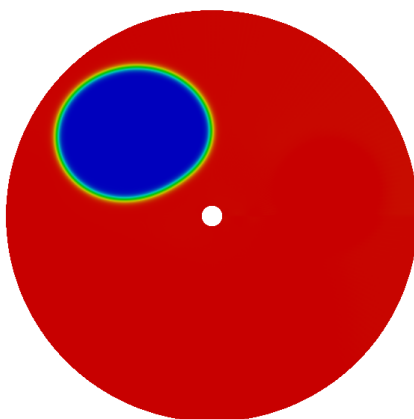(a) Initial condition
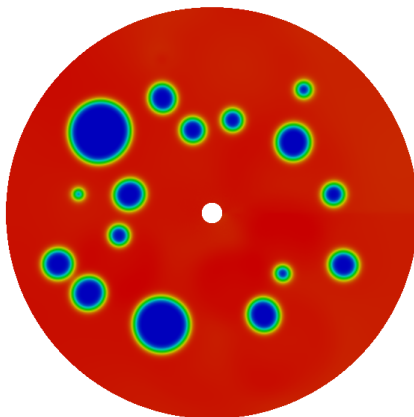
(b) $t = 3.0$

(c) $t = 5.0$

(d) $t = 10.0$

(e) $t = 20.0$

(f) $t = 55.0$

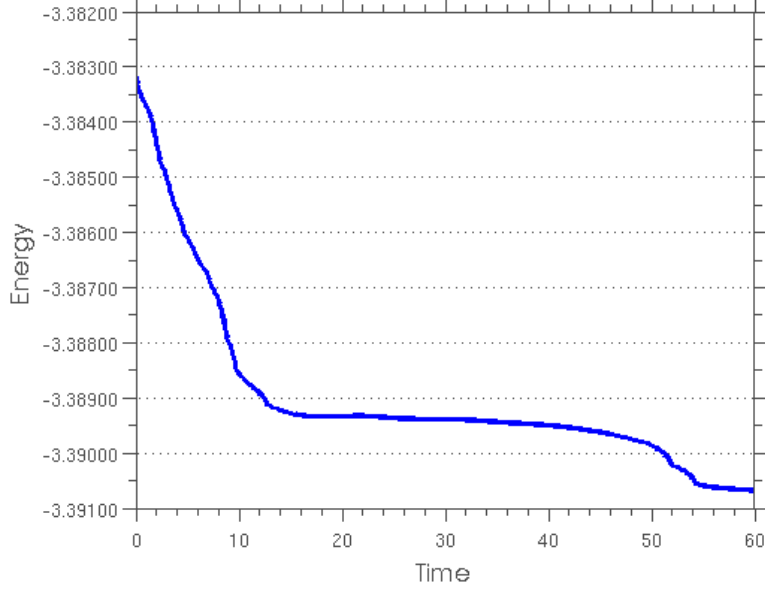Figure 15: Vapor bubble dynamics on an annular surface.

Figure 16: The evolution of total energy for vapor bubble dynamics on an annular surface. The total energy is monotonically decreasing in time.

direction, 513 uniform quadratic NURBS are used for spatial discretization, and in the radial direction, 120 uniform quadratic NURBS are used. In the circumferential direction, periodic boundary conditions are imposed for all variables. On the interior and exterior circular boundaries, the boundary condition (3) is imposed weakly as a natural boundary condition while the no-slip boundary condition (4) is imposed strongly on the velocity field. The initial bubble distribution is chosen randomly. That is, for n_{bub} bubbles at the initial stage, the bubble centers C_i, $i = 1, \cdots, n_{bub}$ are generated randomly within the annular surface. The bubble radii R_i, $i = 1, \cdots, n_{bub}$ are also generated randomly in such a manner that each bubble does not overlap with any other bubble nor cross the annular boundary. We take $n_{bub} = 24$ in our case. If we define $d_j(\mathbf{x})$ as the Euclidean distance between $\mathbf{x}$ and C_j, the initial density profile reads

$$\rho_0(\mathbf{x}) = \sum_{j=1}^{n} \tanh\left(\frac{d_j(\mathbf{x}) - R_j}{2}\sqrt{\mathbb{We}}\right) - 0.25 n_{bub} + 0.6. \tag{193}$$

The initial velocity field is set to be zero. The dimensionless parameters are fixed as $\mathbb{Re} = 1.372 \times 10^2$ and $\mathbb{We} = 4.705 \times 10^3$. A fixed time step size of $\Delta t = 1.0 \times 10^{-4}$ is used for time integration. In Figure 15, we provide snapshots of the density profile at different times. The physical process simulated here is similar to the two-bubble dynamics problem we studied in Section 4.2. Small bubbles merge into large bubbles. After enough time has passed, all 24 bubbles will have merged together and formed one large vapor bubble. In Figure 16 we plot the evolution of total energy over time. This figure shows the total energy is monotonically decreasing with respect to time, again verifying the stability of our algorithm. We have also computed the mass error. Following the notation defined in (186) and (187), we have

47

$\left\| \frac{m_n - m_0}{m_0} \right\|_{l_\infty} = 7.707 \times 10^{-9}.$

5.3   Liquid droplet on a solid substrate

As a final benchmark problem, we study the wetting phenomenon. The wetting phenomenon, which describes the shape of a liquid droplet on a solid substrate, is a challenging problem in fluid mechanics. This problem involves the interaction between three interfaces: the liquid-vapor interface, the liquid-solid interface, and the vapor-solid interface. The shape of the liquid droplet is primarily determined by two factors: (1) the contact angle of the droplet with the solid substrate and (2) the Bond number $\mathbb{B}$o. The size of the contact angle varies depending on whether the surface is hydrophilic or hydrophobic to the fluid. In our model, this contact angle is enforced as a wall boundary condition

$$-\frac{\nabla \rho}{\|\nabla \rho\|} \cdot \mathbf{n} = \cos \varphi, \tag{194}$$

at the wetted surface, where φ is the contact angle. On the other hand, the Bond number assesses the relative importance of the gravity force against the surface tension. If the Bond number is small, the surface tension dominates and the droplet will contract like a sphere. If the Bond number is larger, the gravity force, being the dominant effecting force, will flatten the droplet like a pancake. The wetting phenomenon for two immiscible fluids, e.g. water and air, has been studied in depth both theoretically [29] and numerically [39, 68]. However, the wetting phenomenon of a single material in liquid-vapor phase on a solid substrate has not been the focus of as much study. In [22], the author considered the effects of different contact angle boundary conditions on the shape of the droplet. In our work, we will focus on the effect of the Bond number by fixing the contact angle to be $\pi/2$.

For our simulations, we restrict the computational domain to be the unit square $\Omega = (0, 1)^2$. Our spatial discretizations are comprised of 300^2 quadratic NURBS basis functions. The dimensionless quantities are fixed to be $\mathbb{R}$e $= 848.53$ and $\mathbb{W}$e $= 1.80 \times 10^5$ with criteria (180) and (181) satisfied. The initial density profile is set as

$$\rho_0(\mathbf{x}) = 0.35 - 0.25 \tanh\left(\frac{d(\mathbf{x}) - 0.2}{2}\sqrt{\mathbb{W}\text{e}}\right), \tag{195}$$

$$d(\mathbf{x}) = \sqrt{(x_1 - 0.5)^2 + x_2^2}. \tag{196}$$

We set the volumetric force $\mathbf{f}$ to point in the negative y direction with magnitude $|\mathbf{f}| = 1.0 \times 10^{-3}$, 1.0×10^{-2}, 2.0×10^{-2}, and 5.0×10^{-2}. Recalling the relation (28), this means the corresponding Bond numbers $\mathbb{B}$o are 1.8×10^2, 1.8×10^3, 3.6×10^3, and 9.0×10^3 respectively. We simulate the wetting phenomenon up to a final time of $t = 20.0$ with a fixed time step size of $\Delta t = 4.0 \times 10^{-5}$. The corresponding density profiles at $t = 20.0$ are plotted in Figure 17-20.

We can observe from the four figures that the magnitude of Bond number has a significant impact on the shape of the droplet. In Figure 17, the Bond number is relatively small and hence capillarity dominates. The strong surface tension tries to maintain curvature and makes the droplet almost a spherical cap. In contrast, in Figure 20, the Bond number is

50 times larger, and the gravitational force has a significant impact on the droplet. Consequently, the droplet is flattened as we expected. Intermediate shapes are obtained for $\mathbb{B}o = 1.8 \times 10^3$ and 3.6×10^3.
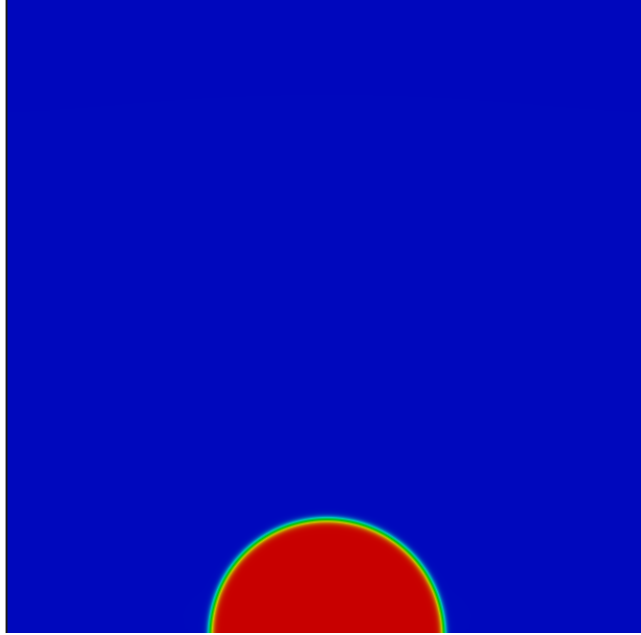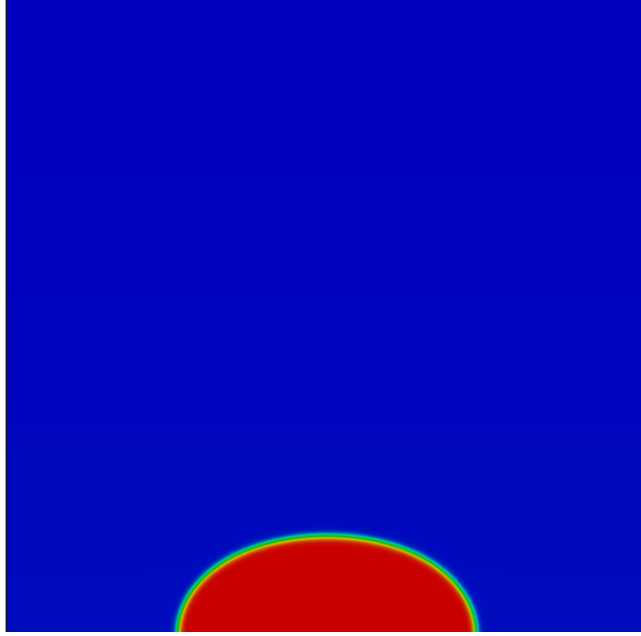

Figure 17: Solution of liquid droplet on solid surface at $t = 20.0$ with $|\mathbf{f}| = \mathbb{B}o/\mathbb{W}e = 1.0 \times 10^{-3}$.

6 Conclusions

In this paper, we introduced a new energy-stable and second-order time-accurate scheme for the Navier-Stokes-Korteweg equations. The spatial discretization of this new scheme is based on a new functional definition of entropy variables. The temporal discretization is based on a recently introduced second-order time integration method which has its roots in numerical quadrature. We provided proofs of nonlinear stability, time accuracy, and mass conservation, and we numerically verified these properties using the method of manufactured solutions as well as comparing our numerical solutions with overkill solutions. We also simulated a variety of benchmark problems to investigate the effectiveness of our method. In particular, we successfully simulated vapor bubble dynamics on an annular surface with the aid of isogeometric analysis, and we investigated the effect of Bond number on the shape of a liquid droplet on a solid substrate.

Acknowledgements

Figure 18: Solution of liquid droplet on solid surface at $t = 20.0$ with $|\mathbf{f}| = \mathbb{B}\text{o}/\mathbb{W}\text{e} = 1.0 \times 10^{-2}$.
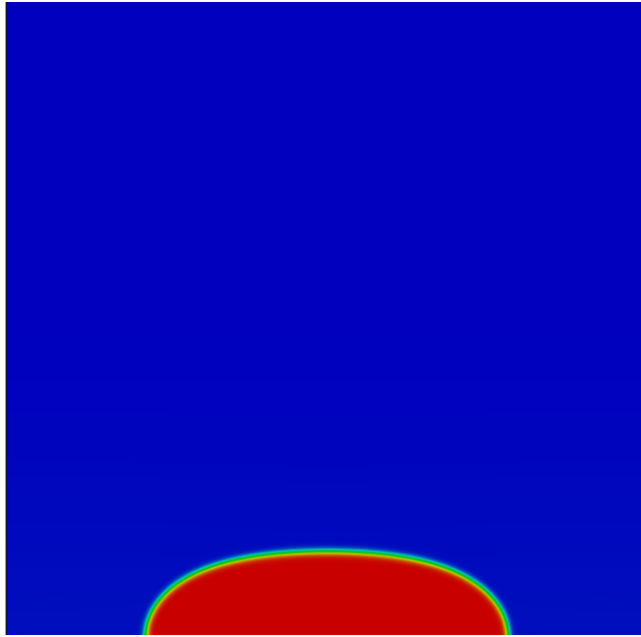

Figure 19: Solution of liquid droplet on solid surface at $t = 20.0$ with $|\mathbf{f}| = \mathbb{B}\text{o}/\mathbb{W}\text{e} = 2.0 \times 10^{-2}$.

Figure 20: Solution of liquid droplet on solid surface at $t = 20.0$ with $|\mathbf{f}| = \mathbb{Bo}/\mathbb{We} = 5.0 \times 10^{-2}$.

A   Rectangular quadrature rules and a first-order nonlinear stable scheme

In this section, we review the well-known rectangular quadrature formulas, and show how they may be applied to generate a nonlinear stable first-order scheme, which has a close link to Eyre's method [27]. We first state the quadrature formulas in the following lemma.

Lemma 3. *(Rectangular quadrature rules) For a function $f \in C^1([a,b])$, there exists $\xi_1, \xi_2 \in (a,b)$ such that the following quadrature rules hold true*

$$\int_a^b f(x)dx = (b-a)f(a) + \frac{(b-a)^2}{2}f'(\xi_1), \tag{197}$$

$$\int_a^b f(x)dx = (b-a)f(b) - \frac{(b-a)^2}{2}f'(\xi_2). \tag{198}$$

Proof. We consider functions $F(x)$ and $G(x)$ defined as follows:

$$F(x) = \int_a^x f(s)ds, \tag{199}$$

$$G(x) = \int_b^x f(s)ds. \tag{200}$$

Taylor expansion of $F(x)$ at a and $G(x)$ at b leads to

$$F(x) = F(a) + (x-a)f(a) + \frac{(x-a)^2}{2}f'(\hat{\xi}_1)$$

$$= (x-a)f(a) + \frac{(x-a)^2}{2}f'(\hat{\xi}_1), \qquad \hat{\xi}_1 \in (a,b); \tag{201}$$

$$G(x) = G(b) + (x-b)f(b) + \frac{(x-b)^2}{2}f'(\hat{\xi}_2)$$

$$= (x-b)f(b) + \frac{(x-b)^2}{2}f'(\hat{\xi}_2), \qquad \hat{\xi}_2 \in (a,b), \tag{202}$$

where $\hat{\xi}_1$ and $\hat{\xi}_2$ depend on x. Specifically, if we take $x=b$ for $F(x)$, and $x=a$ for $G(x)$, we have

$$\int_a^b f(x)dx = F(b) = (b-a)f(a) + \frac{(b-a)^2}{2}f'(\xi_1), \qquad \xi_1 \in (a,b); \tag{203}$$

$$\int_a^b f(x)dx = -G(a) = (b-a)f(b) - \frac{(b-a)^2}{2}f'(\xi_2), \qquad \xi_2 \in (a,b). \tag{204}$$

$\square$

Despite the low-order accuracy of the rectangular quadrature rules, they are useful for constructing a nonlinear stable time integration scheme, as will be shown here. We first split the free energy $W(\rho)$ into a convex part and a concave part, i.e.,

$$W(\rho) = W_1(\rho) + W_2(\rho), \tag{205}$$

where $W_1''(\rho) \geq 0$ and $W_2''(\rho) \leq 0$. The corresponding chemical potentials are denoted as $\mu_1(\rho) = W_1'(\rho)$ and $\mu_2(\rho) = W_2'(\rho)$. Then we have the following identity:

$$\frac{W(\rho_{n+1}^h) - W(\rho_n^h)}{\rho_{n+1}^h - \rho_n^h} = \frac{1}{\rho_{n+1}^h - \rho_n^h} \int_{\rho_n^h}^{\rho_{n+1}^h} \left(W_1'(\rho) + W_2'(\rho) \right) d\rho$$

$$= \frac{1}{\rho_{n+1}^h - \rho_n^h} \int_{\rho_n^h}^{\rho_{n+1}^h} \left(\mu_1(\rho) + \mu_2(\rho) \right) d\rho$$

$$= \mu_1(\rho_{n+1}^h) + \mu_2(\rho_n^h) - \frac{[\![\rho_n^h]\!]}{2} \left(\mu_1'(\rho_{n+\xi_1}^h) - \mu_2'(\rho_{n+\xi_2}^h) \right), \tag{206}$$

where $\xi_1, \xi_2 \in (0,1)$. Note, $\mu_1'(\rho_{n+\xi_1}) - \mu_2'(\rho_{n+\xi_2})$ is always positive due to the splitting. Adopting the same notation as is used in Section 3.3, we state the fully discrete scheme as

follows. In each time step, given ρ_n^h, $\mathbf{u}_n^h$ and v_n^h, we need to find ρ_{n+1}^h, $\mathbf{u}_{n+1}^h$ and v_{n+1}^h such that for all q_1^h, $q_5^h \in \mathcal{V}^h$, and $\mathbf{q}^h = (q_1^h, q_2^h, q_3^h) \in (\mathcal{V}^h)^3$,

$$\mathbf{B}^M(q_1^h; \rho_{n+1}^h, \mathbf{u}_{n+1}^h, v_{n+1}^h) := \left(q_1^h, \frac{[\![\rho_n^h]\!]}{\Delta t_n} \right)_\Omega - \left(\nabla q_1^h, \rho_{n+\frac{1}{2}}^h \mathbf{u}_{n+\frac{1}{2}}^h \right)_\Omega = 0, \tag{207}$$

$$\mathbf{B}^{\mathbf{U}}(\mathbf{q}^h; \rho_{n+1}^h, \mathbf{u}_{n+1}^h, v_{n+1}^h) := \left(\mathbf{q}^h, \mathbf{u}_{n+\frac{1}{2}}^h \frac{[\![\rho_n^h]\!]}{\Delta t_n} + \rho_{n+\frac{1}{2}}^h \frac{[\![\mathbf{u}_n^h]\!]}{\Delta t_n} \right)_\Omega - \left(\nabla \mathbf{q}^h, \rho_{n+\frac{1}{2}}^h \mathbf{u}_{n+\frac{1}{2}}^h \otimes \mathbf{u}_{n+\frac{1}{2}}^h \right)_\Omega$$

$$+ \left(\nabla \mathbf{q}^h, \boldsymbol{\tau}(\mathbf{u}_{n+\frac{1}{2}}^h) \right)_\Omega + \left(\mathbf{q}^h, \rho_{n+\frac{1}{2}}^h \nabla v_{n+1}^h + \rho_{n+\frac{1}{2}}^h \nabla(\frac{|\mathbf{u}_{n+\frac{1}{2}}^h|^2}{2}) \right)_\Omega = 0, \tag{208}$$

$$\mathbf{B}^E(q_5^h; \rho_{n+1}^h, \mathbf{u}_{n+1}^h, v_{n+1}^h) := \left(q_5^h, v_{n+1}^h \right)_\Omega - \left(q_5^h, \mu_1(\rho_{n+1}^h) + \mu_2(\rho_n^h) \right)_\Omega$$

$$+ \left(q_5^h, \frac{2|\mathbf{u}_{n+\frac{1}{2}}^h|^2 - |\mathbf{u}^h|_{n+\frac{1}{2}}^2}{2} \right)_\Omega - \left(\nabla q_5^h, \frac{1}{\mathbb{We}} \nabla \rho_{n+\alpha}^h \right)_\Omega = 0. \tag{209}$$

Following the same manner as in the proof of Theorem 4, we may obtain a dissipation relation for this scheme:

$$\frac{[\![\mathcal{E}(\rho_n^h, \mathbf{u}_n^h)]\!]}{\Delta t_n} = \frac{1}{\Delta t_n} \int_\Omega [\![\rho_n^h \frac{|\mathbf{u}^h|_n^2}{2}]\!] + [\![W(\rho_n^h)]\!] + \frac{1}{2\mathbb{We}} [\![|\nabla \rho^h|_n^2]\!] d\mathbf{x}$$

$$= - (\nabla \mathbf{u}_{n+\frac{1}{2}}^h, \boldsymbol{\tau}(\mathbf{u}_{n+\frac{1}{2}}^h))_\Omega - \left(\frac{[\![\rho_n^h]\!]^2}{2\Delta t_n}, \left(\mu_1'(\rho_{n+\xi_1}) - \mu_2'(\rho_{n+\xi_2}) \right) \right)_\Omega$$

$$- \left(\nabla [\![\rho_n^h]\!], \frac{\eta}{\mathbb{We}\Delta t_n} \nabla [\![\rho_n^h]\!] \right)_\Omega \leq 0. \tag{210}$$

The term $\left(q_5^h, \mu_1(\rho_{n+1}^h) + \mu_2(\rho_n^h) \right)_\Omega$ is only a first-order approximation of $\left(q_5^h, W'(\rho^h) \right)$. Therefore, (207)-(209) leads to a first-order, nonlinear stable scheme for the isothermal Navier-Stokes-Korteweg equations.

Remark 23. *If we apply the rectangular quadrature rules for the Cahn-Hilliard equation within the framework of [31], the resulting first-order nonlinear stable scheme is actually the Eyre's scheme [27], which has enjoyed significant popularity in the phase-field community. However, we note that Eyre's method is restricted to gradient flow problems. Using the rectangular quadrature formulas enables us to extend Eyre's method to more general settings, such as the Navier-Stokes-Korteweg equations.*

Remark 24. *A convex-concave splitting of the free energy function W of the van der Waals fluid is:*

$$W_1 = \frac{8}{27} \theta \rho \log \left(\frac{\rho}{1 - \rho} \right), \tag{211}$$

$$W_2 = - \rho^2. \tag{212}$$

This can be used in (205) as a basis for the first-order stable scheme.

B A pair of perturbed mid-point quadrature rules and a second-order nonlinear stable scheme

Lemma 4. *(Perturbed mid-point rules) For a function $f \in C^3([a,b])$, there exists $\xi_1, \xi_2 \in (a,b)$ such that the following quadrature rules hold true*

$$\int_a^b f(x)dx = (b-a)f(\frac{a+b}{2}) + \frac{(b-a)^3}{24}f''(a) + \frac{(b-a)^4}{48}f'''(\xi_1), \tag{213}$$

$$\int_a^b f(x)dx = (b-a)f(\frac{a+b}{2}) + \frac{(b-a)^3}{24}f''(b) - \frac{(b-a)^4}{48}f'''(\xi_2). \tag{214}$$

Proof. Let $P(x)$ be a quadratic polynomial satisfying

$$P(\frac{a+b}{2}) = f(\frac{a+b}{2}), \qquad P'(\frac{a+b}{2}) = f'(\frac{a+b}{2}), \qquad P'' = f''(a). \tag{215}$$

Let us denote $R(x)$ as $R(x) = f(x) - P(x)$, and we may rewrite $R(x)$ as

$$R(x) = w(x)S(x), \tag{216}$$

$$w(x) = (x - \frac{a+b}{2})^2(x - 2a + b). \tag{217}$$

According to l'Hôspital's rule,

$$\lim_{x \to \frac{a+b}{2}} S(x) = \frac{R''(\frac{a+b}{2})}{3(b-a)} = \frac{f''(\frac{a+b}{2}) - P''}{3(b-a)} = \frac{f''(\frac{a+b}{2}) - f''(a)}{3(b-a)} = \frac{f'''(a+\zeta)}{6}, \tag{218}$$

for $\zeta \in (0, (b-a)/2)$. Therefore, $S(x)$ is well-defined in (a,b). Consider a function $F(z) = f(z) - P(z) - w(z)S(x)$, with $x \in (a,b), x \neq \frac{a+b}{2}$ fixed. Apparently, $F(z)$ satisfies

$$F(\frac{a+b}{2}) = F'(\frac{a+b}{2}) = F''(a) = F(x) = 0. \tag{219}$$

Applying Rolle's rule three times, we may find that there exists $\theta \in (a,b)$ such that $F'''(\theta) = 0$. Therefore,

$$f'''(\theta) - P'''(\theta) - w'''(\theta)S(x) = 0 \tag{220}$$

$$\Rightarrow S(x) = \frac{f'''(\theta)}{w'''(\theta)} = \frac{f'''(\theta)}{6}. \tag{221}$$

Relations (218) and (221) imply that there exist $\theta \in (a,b)$ such that $S(x) = f'''(\theta)/6$ for $\forall x \in (a,b)$. Considering the integration of $f(x)$ over (a,b), we have

$$\int_a^b f(x)dx = \int_a^b P(x)dx + \int_a^b w(x)S(x)dx. \tag{222}$$

It is easy to verify that $w(x)$ does not change its sign in (a, b), therefore, the mean value theorem implies

$$\int_a^b w(x)S(x)dx = \int_a^b w(x)\frac{f'''(\theta)}{6}dx = \frac{f'''(\xi_1)}{6}\int_a^b w(x)dx = \frac{f'''(\xi_1)}{48}(b-a)^4. \tag{223}$$

Also, we may obtain an explicit form of $P(x)$ by solving the equations (215), and we have

$$\int_a^b P(x)dx = (b-a)f(\frac{a+b}{2}) + \frac{(b-a)^3}{24}f''(a). \tag{224}$$

Combing the results (223) and (224), we have

$$\int_a^b f(x)dx = (b-a)f(\frac{a+b}{2}) + \frac{(b-a)^3}{24}f''(a) + \frac{(b-a)^4}{48}f'''(\xi_1), \tag{225}$$

which proved the first quadrature formula (213). The proof for the second formula (214) follows the same manner by choosing $P(x)$ satisfying

$$P(\frac{a+b}{2}) = f(\frac{a+b}{2}), \qquad P'(\frac{a+b}{2}) = f'(\frac{a+b}{2}), \qquad P'' = f''(b), \tag{226}$$

and

$$w(x) = (x - \frac{a+b}{2})^2(x - 2b + a). \tag{227}$$

$\square$

Since the free energy function is super-convex for the van der Waals fluid, we only need (214) to approximate $W'(\rho^h)$,

$$\begin{aligned}
\frac{W(\rho_{n+1}^h) - W(\rho_n^h)}{\rho_{n+1}^h - \rho_n^h} &= \frac{1}{\rho_{n+1}^h - \rho_n^h}\int_{\rho_{n+1}^h}^{\rho_n^h} W'(\rho)d\rho \\
&= \frac{1}{\rho_{n+1}^h - \rho_n^h}\int_{\rho_{n+1}^h}^{\rho_n^h} \mu(\rho)d\rho \\
&= \mu(\rho_{n+\frac{1}{2}}^h) + \frac{[\![\rho_n^h]\!]^2}{24}\mu''(\rho_{n+1}^h) - \frac{[\![\rho_n^h]\!]^3}{48}\mu'''(\rho_{n+\xi}^h),
\end{aligned} \tag{228}$$

where $\xi \in (0, 1)$. Adopting the notations in Section 3.3, we state a fully discrete scheme based on the perturbed mid-point rule. In each time step, given ρ_n^h, $\mathbf{u}_n^h$ and v_n^h, we need to

55

find ρ_{n+1}^h, $\mathbf{u}_{n+1}^h$ and v_{n+1}^h such that for all q_1^h, $q_5^h \in \mathcal{V}^h$, and $\mathbf{q}^h = (q_1^h, q_2^h, q_3^h) \in (\mathcal{V}^h)^3$,

$$\mathbf{B}^M(q_1^h; \rho_{n+1}^h, \mathbf{u}_{n+1}^h, v_{n+1}^h) := \left(q_1^h, \frac{[\![\rho_n^h]\!]}{\Delta t_n}\right)_\Omega - \left(\nabla q_1^h, \rho_{n+\frac{1}{2}}^h \mathbf{u}_{n+\frac{1}{2}}^h\right)_\Omega = 0, \tag{229}$$

$$\mathbf{B}^{\mathbf{U}}(\mathbf{q}^h; \rho_{n+1}^h, \mathbf{u}_{n+1}^h, v_{n+1}^h) := \left(\mathbf{q}^h, \mathbf{u}_{n+\frac{1}{2}}^h \frac{[\![\rho_n^h]\!]}{\Delta t_n} + \rho_{n+\frac{1}{2}}^h \frac{[\![\mathbf{u}_n^h]\!]}{\Delta t_n}\right)_\Omega - \left(\nabla \mathbf{q}^h, \rho_{n+\frac{1}{2}}^h \mathbf{u}_{n+\frac{1}{2}}^h \otimes \mathbf{u}_{n+\frac{1}{2}}^h\right)_\Omega$$

$$+ \left(\nabla \mathbf{q}^h, \boldsymbol{\tau}(\mathbf{u}_{n+\frac{1}{2}}^h)\right)_\Omega + \left(\mathbf{q}^h, \rho_{n+\frac{1}{2}}^h \nabla v_{n+1}^h + \rho_{n+\frac{1}{2}}^h \nabla(\frac{|\mathbf{u}_{n+\frac{1}{2}}^h|^2}{2})\right)_\Omega = 0, \tag{230}$$

$$\mathbf{B}^E(q_5^h; \rho_{n+1}^h, \mathbf{u}_{n+1}^h, v_{n+1}^h) := \left(q_5^h, v_{n+1}^h\right)_\Omega - \left(q_5^h, \mu(\rho_{n+\frac{1}{2}}^h) + \frac{[\![\rho_n^h]\!]^2}{24}\mu''(\rho_{n+1}^h)\right)_\Omega$$

$$+ \left(q_5^h, \frac{2|\mathbf{u}_{n+\frac{1}{2}}^h|^2 - |\mathbf{u}^h|_{n+\frac{1}{2}}^2}{2}\right)_\Omega - \left(\nabla q_5^h, \frac{1}{\mathbb{W}e}\nabla \rho_{n+\alpha}^h\right)_\Omega = 0. \tag{231}$$

Following the same procedure as of the proof of Theorem 4, we may derive a discrete dissipation estimate for the scheme (229)-(231):

$$\frac{[\![\mathcal{E}(\rho_n^h, \mathbf{u}_n^h)]\!]}{\Delta t_n} = \frac{1}{\Delta t_n}\int_\Omega [\![\rho_n^h \frac{|\mathbf{u}^h|_n^2}{2}]\!] + [\![W(\rho_n^h)]\!] + \frac{1}{2\mathbb{W}e}[\![|\nabla \rho^h|_n^2]\!]d\mathbf{x}$$

$$= -(\nabla \mathbf{u}_{n+\frac{1}{2}}^h, \boldsymbol{\tau}(\mathbf{u}_{n+\frac{1}{2}}^h))_\Omega - \left(\frac{[\![\rho_n^h]\!]^4}{\Delta t_n}, \frac{1}{48}\mu'''(\rho_{n+\xi}^h)\right)_\Omega$$

$$- \left(\nabla[\![\rho_n^h]\!], \frac{\eta}{\mathbb{W}e\Delta t_n}\nabla[\![\rho_n^h]\!]\right)_\Omega \leq 0. \tag{232}$$

Taylor's expansion may show that the fully discrete scheme (229)-(231) is second-order accurate in time.

Remark 25. *Comparing the discrete dissipation relations (121) and (232), we notice that when $\eta = 0$, the numerical dissipation introduced by the scheme (98)-(100) is*

$$\int_\Omega \frac{[\![\rho_n^h]\!]^4}{24\Delta t_n}\mu'''(\rho_{n+\hat{\xi}}^h)d\mathbf{x}, \tag{233}$$

while the numerical dissipation introduced by the scheme (229)-(231) is

$$\int_\Omega \frac{[\![\rho_n^h]\!]^4}{48\Delta t_n}\mu'''(\rho_{n+\tilde{\xi}}^h)d\mathbf{x}. \tag{234}$$

Since it is hard to compare the value of $\mu'''(\rho_{n+\hat{\xi}}^h)$ and $\mu'''(\rho_{n+\tilde{\xi}}^h)$, we can only conclude that the fully discrete scheme (229)-(231) is less dissipative than the numerical scheme (98)-(100).

References

[1] Thermophysical Properties of Fluid Systems. http://webbook.nist.gov/chemistry/fluid/. [Online; accessed 15-July-2012].

[2] S. Balay, W. Gropp, L.C. McInnes, and B. Smith. PETSc 2.0 users manual. Mathematics and Computer Science Division, Argonne National Laboratory http://www.mcs.anl.gov/petsc, 2000.

[3] G. I. Barenblatt. *Similarity, self-similarity, and intermediate assymptotics.* Plenum Press, New York and London, 1979.

[4] Y. Bazilevs, V.M. Calo, J.A. Cottrell, J.A. Evans, T.J.R. Hughes, S. Lipton, M.A. Scott, and T.W. Sederberg. Isogeometric analysis using T-splines. *Computer Methods in Applied Mechanics and Engineering*, 199(5-8):229–263, 2010.

[5] Y. Bazilevs, V.M. Calo, J.A. Cottrell, T.J.R. Hughes, A. Reali, and G. Scovazzi. Variational multiscale residual-based turbulence modeling for large eddy simulation of incompressible flows. *Computer Methods in Applied Mechanics and Engineering*, 197:173–201, 2007.

[6] Y. Bazilevs, V.M. Calo, T.J.R. Hughes, and Y. Zhang. Isogeometric fluid-structure interaction: Theory, algorithms, and computations. *Computational Mechanics*, 43:3–37, 2008.

[7] Y. Bazilevs, V.M. Calo, Y. Zhang, and T.J.R. Hughes. Isogeometric fluid-structure interaction analysis with applications to arterial blood flow. *Computational Mechanics*, 38:310–322, 2006.

[8] S. Benzoni-Gavage. Stability of subsonic planar phase boundaries in a van der Waals fluid. *Archive for Rational Mechanics and Analysis*, 150:23–55, 1999.

[9] S. Benzoni-Gavage, R. Danchin, S. Descombes, and D. Jamet. *Control Methods in PDE-Dynamical Systems*, volume 426 of *Contemporary Mathematics*, chapter Stability issues in the Euler-Korteweg model, pages 103–127. American Mathematical Society, Providence, RI, 2007.

[10] C. Blanc and C. Schlick. Accurate Parametrization of Conic by NURBS. *Computer Graphics and Applications*, 16:64–71, 1996.

[11] M.J. Borden, M.A. Scott, J.A. Evans, and T.J.R. Hughes. Isogeometric finite element data structures based on Bézier extraction of NURBS. *International Journal for Numerical Methods in Engineering*, 87:15–47, 2011.

[12] M.J. Borden, M.A. Scott, C.V. Verhoosel, C.M. Landis, and T.J.R. Hughes. Phase-field modeling of dynamic fracture using isogeometric analysis. *Computer Methods in Applied Mechanics and Engineering*, 217-220:77–95, 2011.

[13] S.W. Bova and G.F. Carey. An entropy variable formulation and applications for the two-dimensional shallow water equations. *International Journal of Numerical Methods in Fluids*, 23:29–46, 1996.

[14] D. Bresch, B. Desjardins, and C.K. Lin. On some compressible fluid models: Korteweg, lubrication, and shallow water systems. *Communications in Partial Differential Equations*, 28:843–868, 2003.

[15] C. Chalons and P.G. LeFloch. High-Order Entropy-Conservative Schemes and Kinetic Relations for van der Waals Fluids. *Journal of Computational Physics*, 168(1):184 – 206, 2001.

[16] L.Q. Chen. Phase-field models for microstructural evolution. *Annual Review of Materials Research*, 32:113–140, 2002.

[17] B. Cockburn and H. Gau. A Model Numerical Scheme for the Propagation of phase Transitions in Solids. *SIAM Journal on Scientific Computin*, 17:1092–1121, 1996.

[18] J.A. Cottrell, T.J.R. Hughes, and Y. Bazilevs. *Isogeometric analysis: Toward Integration of CAD and FEA*. Wiley, Chichester, 2009.

[19] J.A. Cottrell, T.J.R. Hughes, and A. Reali. Studies of refinement and continuity in isogeometric analysis. *Computer Methods in Applied Mechanics and Engineering*, 196:4160–4183, 2007.

[20] W. Danchin and B. Desjardins. Existence of solutions for compressible fluid models of Korteweg type. *Annales de l'Institut Henri Poincaré (C) Analyse Non Linéaire*, 18:97–133, 2001.

[21] L. Dede, M.J. Borden, and T.J.R. Hughes. Isogeometric Analysis for Topology Optimization with a Phase Field Model. *Archives of Computational Methods in Engineering*, 19:427–465, 2012.

[22] D. Diehl. *High Order Schemes for Simulation of Compressible Liquid-Vapor Flows with Phase Change*. PhD thesis, Albert-Ludwigs-Universitat Freiburg, 2007.

[23] J.E. Dunn and J. Serrin. On the thermomechanics of interstitial working. *Archive for Rational Mechanics and Analysis*, 88:95–133, 1985.

[24] J.A. Evans, Y. Bazilevs, I. Babuška, and T.J.R. Hughes. *n*-widths, sup-infs, and optimality ratios for the *k*-version of the isogeometric finite element method. *Computer Methods in Applied Mechanics and Engineering*, 198(21-26):1726–1741, 2009.

[25] J.A. Evans and T.J.R. Hughes. Isogeometric divergence-conforming B-splines for the Darcy-Stokes-Brinkman equations. *Mathematical Models and Methods in Applied Sciences*, 2012. DOI: 10.1142/S0218202512500583.

[26] L.C. Evans. *Partial Differential Equations (Graduate Studies in Mathematics, Vol. 19)*. American Mathematical Society, Providence, RI, 2002.

[27] D.J. Eyre. An unconditionally stable one-step scheme for gradient systems. www.math.utah.edu/eyre/research/methods/stable.ps.

[28] E. Feireisl. Compressible Navier-Stokes equations with a non-monotone pressure law. *Journal of Differential Equations*, 184:97–108, 2002.

[29] P. Gennes, F. Brochard-Wyart, and D. Quere. *Capillarity and Wetting Phenomena: Drops, Bubbles, Pearls, Waves.* Springer, 2003.

[30] H. Gomez, V.M. Calo, Y. Bazilevs, and T.J.R. Hughes. Isogeometric analysis of the Cahn-Hilliard phase-field model. *Computer Methods in Applied Mechanics and Engineering*, 197:4333–4352, 2008.

[31] H. Gomez and T.J.R. Hughes. Provably unconditionally stable, second-order time-accurate, mixed variational methods for phase-field models. *Journal of Computational Physics*, 230(13):5310 – 5327, 2011.

[32] H. Gomez, T.J.R. Hughes, X. Nogueira, and V.M. Calo. Isogeometric analysis of the isothermal Navier-Stokes-Korteweg equations. *Computer Methods in Applied Mechanics and Engineering*, 199(25-28):1828–1840, 2010.

[33] H. Gomez and X. Nogueira. An unconditionally energy-stable method for the phase eld crystal equation. *Computer Methods in Applied Mechanics and Engineering*, 249-252:52–61, 2012.

[34] A. Harten. On the symmetric form of systems of conservation laws with entropy. *Journal of Computational Physics*, 49:151–164, 1983.

[35] H. Hattori and D. Li. The existence of global solutions to a fluid dynamic model for materials for korteweg type. *Journal of Partial Differential Equations*, 9:323–342, 1996.

[36] T.J.R. Hughes. *The Finite Element Method: Linear Static and Dynamic Finite Element Analysis.* Dover Publications, Mineola, NY, 2000.

[37] T.J.R. Hughes, J.A. Cottrell, and Y. Bazilevs. Isogeometric analysis: CAD, finite elements, NURBS, exact geometry, and mesh refinement. *Computer Methods in Applied Mechanics and Engineering*, 194:4135–4195, 2005.

[38] T.J.R. Hughes, L.P. Franca, and M. Mallet. A new finite element formulation for computational fluid dynamics: I. Symmetric forms of the compressible Euler and Navier-stokes equations and the second law of thermodynamics. *Computer Methods in Applied Mechanics and Engineering*, 54:223–234, 1986.

[39] D. Jacqmin. Contact-line dynamics of a diffuse fluid interface. *Journal of Fluid Mechanics*, 402:57–88, 2000.

[40] R.D. James. The propagation of phase boundaries in elastic bars. *Archive for Rational Mechanics and Analysis*, 73:125–158, 1980.

[41] D. Jamet, O. Lebaigue, N. Coutris, and J.M. Delhaye. The second gradient method for the direct numerical simulation of liquid-vapor flows with phase change. *Journal of Computational Physics*, 169:624–651, 2001.

[42] S. Jin. Numerical integrations of systems of conservation laws of mixed type. *SIAM Journal on Applied Mathematics*, 55:1536–1551, 1995.

[43] J. Kiendl, K.-U. Bletzinger, J. Linhard, and R. Wüchner. Isogeometric shell analysis with Kirchhoff-Love elements. *Computer Methods in Applied Mechanics and Engineering*, 198(49-52):3902–3914, 2009.

[44] M. Kotschote. Strong solutions for a compressible fluid model of Korteweg type. *Annales de l'Institut Henri Poincaré (C) Analyse Non Linéaire*, 25(4):679 – 696, 2008.

[45] G. Kuiper. *Cavitation inception on ship propeller models.* PhD thesis, Delft University of Technology, 1981.

[46] P.G. LeFloch. *Hyperbolic Systems of Conservation Laws: The Theory of Classical and Nonclassical Shock Waves.* Lectures in Mathematics, ETH Zurich, 2002.

[47] P.G. LeFloch. Kinetic relations for undercompressive shock waves. physical, mathematical, and numerical issues. In H. Holden and K. Karlsen, editors, *Contemporary Mathematics*, volume 526. American Mathematical Society, 2010.

[48] P.G. LeFloch and S. Mishra. Kinetic functions in magnetohydrodynamics with resistivity and hall effect. *Acta Mathematica Scientia*, 29:1684–1702, 2009.

[49] S. Lipton, J.A. Evans, Y. Bazilevs, T. Elguedj, and T.J.R. Hughes. Robustness of isogeometric structural discretizations under severe mesh distortion. *Computer Methods in Applied Mechanics and Engineering*, 199(5-8):357–373, 2010.

[50] L.Ratke and P. W. Voorhees. *Growth and Coarsening: Ostwald Ripening in Material Processing (Engineering Materials).* Springer, 1 edition, 2002.

[51] H. Matthies and G. Strang. The solution of nonlinear finite element equations. *International Journal for Numerical Methods in Engineering*, 14:1613–1626, 1979.

[52] J.T. Oden, A. Hawkins, and S. Prudhomme. General diffuse-interface theories and an approach to predictive tumor growth modeling. *Mathematical Models and Methods in Applied Sciences*, 20:477–517, 2010.

[53] Y. Saad and M.H. Schultz. GMRES: A generalized minimal residual algorithm for solving nonsymmetric linear systems. *SIAM Journal of Scientific and Statistical Computing*, 7:856–869, 1986.

[54] D. Schillinger, L. Dedé, M.A. Scott, J.A. Evans, M.J. Borden, E. Rank, and T.J.R. Hughes. An isogeometric design-through-analysis methodology based on adaptive hierarchical refinement of NURBS, immersed boundary methods, and T-spline CAD surfaces. *Computer Methods in Applied Mechanics and Engineering*, 2012. In press.

[55] M.A. Scott. *T-splines as a Design-Through-Analysis Technology.* PhD thesis, The University of Texas at Austin, 2011.

[56] M.A. Scott, X. Li, T.W. Sederberg, and T.J.R. Hughes. Local refinement of analysis-suitable T-splines. *Computer Methods in Applied Mechanics and Engineering*, 213:206–222, 2012.

[57] J. Serrin. The area rule for simple fluid phase transition. *Journal of Elasticity*, 90:129–159, 2008.

[58] F. Shakib. *Finite element analysis of the compressible Euler and Navier-Stokes equations*. PhD thesis, Stanford University, 1989.

[59] F. Shakib, T.J.R. Hughes, and Z. Johan. A new finite element formulation for computational fluid dynamics: X. The compressible Euler and Navier-Stokes equations. *Computer Methods in Applied Mechanics and Engineering*, 89:141–219, 1991.

[60] C.W. Shu. A numerical method for systems of conservation laws of mixed type admitting hyperbolic flux splitting. *Journal of Computational Physics*, 100:424–429, 1992.

[61] M. Slemrod. Admissibility criteria for propagating phase boundaries in a van der Waals fluid. *Archive for Rational Mechanics and Analysis*, 81(4):301–315, 1983.

[62] M. Slemrod and J.E. Flaherty. Numerical integration of a Riemann problem for a van der Waals fluid. In E.C. Aifantis and J. Gittus, editors, *Phase Transformations*, pages 203–212. Elsevier, 1986.

[63] Y. Su and C.M. Landis. Continuum Thermodynamics of Ferroelectric Domain Evolution: Theory, Finite Element Implementation, and Application to Domain Wall Pinning. *Journal of the Mechanics and Physics of Solids*, 55:280–305, 2007.

[64] M.L. Szulczewski, C.W. MacMinn, H.J. Herzog, and R. Juanes. Lifetime of carbon capture and storage as a climate-change mitigation technology. *Proceedings of the National Academy of Sciences of the United States of America*, 109(14):5185–5189, 2012.

[65] E. Tadmor. Skew selfadjoint form for systems of conservation laws. *Journal of Mathematical Analysis and Applications*, 103:428–442, 1984.

[66] M. Versluis, B. Schmitz, A. von der Heydt, and D. Lohse. How snapping shrimp snap: Through cavitating bubbles. *Science*, 289(5487):2114–2117, 2000.

[67] P. Yue, J.J. Feng, C. Liu, and J. Shen. A diffuse-interface method for simulating two-phase flows of complex fluids. *Journal of Fluid Mechanics*, 515:293–317, 2004.

[68] P. Yue, C. Zhou, and J.J. Feng. Sharp-interface limit of the Cahn-Hilliard model for moving contact lines. *Journal of Fluid Mechanics*, 645:279–294, 2010.